ACHIEVEING HIGH EFFICIENCY THERMOELECTRIC HEATING AND COOLING WITH METAL FOAM HEAT EXCHANGERS

by

Gavin Clark

A Thesis Submitted in Partial Fulfillment
of the Requirements for the Degree of

Master of Applied Science in Automotive Engineering

The Faculty of Engineering and Applied Science Program
University of Ontario Institute of Technology
April 2014

ACKNOWLEDGMENT

This thesis would not have been possible without the guidance and support of my supervisor, Dr. Greg Rohrauer. His passion and knowledge in the automotive field led to my pursuit of a master's degree in automotive engineering. He has taught me practical life skills and greatly expanded my knowledge of the automotive field. It was a privilege to have him as a supervisor during my tenure at UOIT.

I am also grateful for the support of Eric Hagverdian who spent countless hours building, testing and supporting my research. His machining expertise helped discover key issues and the completion of this thesis would not have been possible without him.

To all my friends how have supported me: Hugo Provencher for the many hours proofreading my papers, Joseph Brennan, Lesley McLelland and the remainder of the EcoCar team for the many enjoyable trips and long nights at the shop where my true passion for EV's began.

To my parents and family who have supported me through this journey both financially and spiritually.

The Automotive Partnership Canada and EcoCar: The NeXt Challenge for their financial support.

ABSTRACT

This thesis examines the development of a high efficiency heat pump system using thermoelectric (TE) and reticulated metal foam (RMF) technologies to power a vehicle`s battery thermal management system. The focus is split into two areas: first a review of TE's sourcing or removing heat, second an examination of compact heat exchanger (HX) design. Five TE suppliers were investigated to understand the performance and limitations of their TE modules. Testing showed the Kyrotherm product to be superior so it was used as a design basis. RMF's are known to be an effective means to improve the performance of compact heat exchangers, thus HX's were evaluated with RMF foams compressed to varying densities in order to understand their potential in conjunction with thermoelectric devices. Experimental results showed performance was limited due to adequate bonding, yet still on par with the highest efficiency technologies currently on the market.

Keywords: thermoelectrics, compact heat exchanger, reticulated metal foam, battery thermal management.

TABLE OF CONTENTS

LIST OF FIGURES

LIST OF TABLES

NOMENCLATURE

A_{con}	contact area (m^2)
a	width of flow passage (m)
b	height of flow passage (m)
A_{cs}	cross-sectional area (m^2)
B_i	Bias
COP	Coefficient of Performance
C_p	specific heat (J/kg·K)
D_{hyd}	hydraulic diameter (m)
E	thermoemf (V)
E_{max}	maximum thermoemf (V)
g	TE arm packing density
h	heat transfer coefficient (W/m^2)
I	current (A)
I_{max}	maximum current (A)
i	non-dimensional current (-)
j	Colburn factor (-)
k	thermal conductivity of thermoelement materials (W/mK)
k_c	thermal contact conductivity (W/m^2K)
K	thermal conductance of a TE couple (W/K)
K_c	thermal contact conductance (W/K)
K_{eqv}	equivalent thermal conductance (W/K)
K_p	permeability factor (m^2)
L_{ref}	reference length (mm)
l	non-dimensional thermoelement length (-)
L	thermoelement length (mm)
L_f	flow length (m)
Nu	Nusselt number (-)
P	power (W)

Q	volumetric flow rate (m^3/s)
Q_c	cooling power at cold side (W)
Q_h	heat power at hot side (W)
Re	Reynolds number (-)
Re_k	Reynolds number for permeability (-)
R_{th}	thermal resistance(K/W)
S_i	Precision
Q	volumetric flow rate (m^3/s)
Q_c	cooling power at cold side (W)
Q_h	heat power at hot side (W)
T_c	cold side temperature (°C)
$T_{c,inlet}$	cold side inlet temperature (°C)
$T_{c,outlet}$	cold side outlet temperature (°C)
$T_{c,max}$	cold side maximum temperature (°C)
T_{LTMD}	fluid log mean temperature difference (°C)
T_h	hot side temperature (°C)
T_{pl}	plate temperature (°C)
U_i	Uncertainty
v_d	Darcian velocity (m/s)
V	voltage (V)
V_m	flow velocity (m/s)
V_{max}	maximum voltage (V)
W	pumping power (W)
Z	figure of merit (1/K)
Z_{eqv}	equivalent figure of merit (1/K)
σ	standard deviation (-)
α	Seebeck coefficient of a TE couple (V/K)
α_f	fluid thermal diffusivity (m^2/s)
ρ	density (kg/m^3)
ρ_r	electrical resistivity of thermoelement materials (Ωm)

ρ_f	foam density (kg/m^3)
ρ_s	solid density (kg/m^3)
π_{AB}	differential Peltier Effect
θ	non-dimensional (-)
ΔP	pressure differential (Pa)
ΔT	temperature difference (K)
ΔT_{max}	maximum temperature difference (K)
μ	dynamic viscosity (kg/m·s)
υ	kinematic viscosity (m^2/s)
ε	porosity (-)

Abbreviations

A/C	Air conditioning
CCS	Climate controlled seat
CPU	Computer processing unit
DAQ	Data acquisition system
ESS	Energy storage system
EV	Electric vehicle
FRP	Fiberglass reinforced plastic
HEV	Hybrid electric vehicle
HVAC	Heating ventilation and air conditioning
HX	Heat exchanger
IGBT	Insulated gate bipolar transistor
Li-Ion	Lithium ion
MTBF	Mean time between failures
OEM	Original equipment manufacturer
PID	Proportional integral derivative
PPI	Pores per inch
PTC	Positive thermal coefficient
RMF	Reticulated metal foam
TE	Thermoelectric

TEC	Thermoelectric cooling
TEG	Thermoelectric generator
TPM	Thermosyphon porous medium

CHAPTER 1 – BACKGROUND

1.1. OVERVIEW

This thesis investigates two unique technologies, thermoelectrics (TE) and reticulated metal foams (RMF), in an attempt to develop a compact high efficiency heat pump system for use within a vehicle's battery thermal management system. The TE device acts as a source to provide or remove heat based on the demand. Secondly a compact heat exchanger (HX) was designed and tested; the RMF is placed inside the cavity to improve overall thermal performance. The goal of combining these two technologies is creating a heat pump system that has a heat transfer coefficient of 30,000 W/m^2K.

The first chapter reviews the background of these technologies and the industries they are found within. Chapter 2 provides a more in-depth look at the theory, operation and performance of each technology. Chapter 3 outlines the experiments used to evaluate the TE modules under working conditions. The results indicate which TE module performs superior in a real world testing environment. HX design, experimentation and results are presented in Chapter 4 along with a detailed post mortem analysis outlining the issues stemming from a lack of bonding. The final chapter draws conclusions and includes recommendations for future research.

1.2. THERMOELECTRICS

The use of thermoelectric (TE) devices is not new; Seebeck and Peltier devices were developed in the 1800s but did not see application in industry until the late 1950s. Initially the materials used were very inefficient and required substantial amounts of power to perform their tasks. In the 1950s, the development of semiconductors led to practical TE devices, which consumed less power and had superior performance. Presently, devices are

being used in military, aerospace, scientific, medical, electronics and most recently, in automotive applications. Through varying configurations a TE device is able to provide: heating, cooling and electricity. Throughout the first 40 years of commercial introduction, few improvements were made to TE devices. Recent advancements in materials, manufacturing and heat transfer effectiveness introduce new opportunities for TE devices.

As with most innovative ideas, thermoelectrics began with application in the military and aerospace industries. These industries took advantage of TEs as generators and cooling devices. Most space missions by NASA incorporated thermoelectric generators to provide electric power to their rockets or satellites. The longest running is still in use today after 35 years of service. The military has also employed TE devices as generators due to their ability to provide power silently in stealth operations.

The electronics and automotive industries will be analyzed in this review; both offer new opportunities for TE devices. The electronics industry is now applying TE modules as active cooling devices for computer CPUs and other heat generating devices such as laser diodes and infrared cameras. TE devices are also being introduced into mass market consumer products, such as small refrigerators and freezers. The automotive industry began using TE devices in temperature regulating seats during the late 1990s. These have since seen substantial growth, and are currently being installed in over 1,000,000 cars annually. Research continues to be conducted to determine the technological viability of TEs to perform as the vehicle's heating, ventilation and air conditioning (HVAC) system. There is a big effort underway to use the devices for generating electricity through

extraction of waste heat from the exhaust. Such systems are being developed to improve fuel economy while reducing vehicle emissions.

1.2.1. HISTORY OF THERMOELECTRIC DEVICES

Thermoelectric effects were first discovered by Thomas Johann Seebeck in 1821 [**1**]. Seebeck found that a circuit made from two dissimilar metals at different temperatures would deflect a compass magnet. Initially he believed this was due to magnetism relative to earth's magnetic field. After continued experimentation he found that the temperature difference in fact produced a voltage. His first experiment is depicted in Figure 1, where n and o are dissimilar metals and the flame is being applied from a candle.

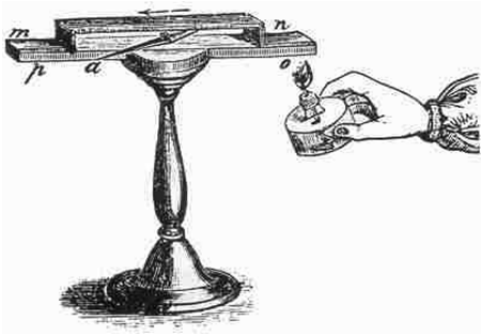

Figure 1: Seebeck's first thermoelectric instrument [**2**]

With continued experimentation Seebeck determined that the voltage produced was proportional to the temperature difference. The proportional constant α is known as the Seebeck coefficient and is used in thermoelectric processes to define the power. Thermocouples are devices that use the Seebeck effect to measure the temperature difference between given points. This is accomplished as shown in Figure 2 where each junction is at a different temperature when introduced to a heat source. This temperature differential will produce a voltage that can be measured. Thermocouples are the most well-known and widely used type of thermoelectric device on the market today.

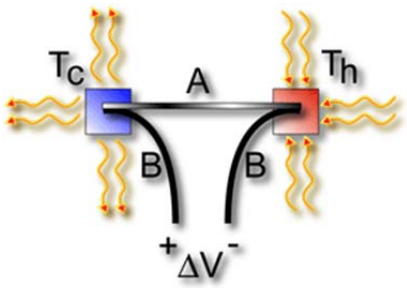

Figure 2: Seebeck effect [**2**]

The second discovery in thermoelectrics was made by Jean Charles Athanase Peltier in 1834. Peltier discovered that inducing an electric current through a thermocouple would produce either heating or cooling. Four years later Emil Lenz set up an experiment to show that this concept could melt ice and freeze water on the same surface by switching the direction of current flow. From Lenz's observations it was found that the heat absorbed or created was proportional to the electric current applied. This is now referred to as the differential Peltier coefficient, π_{AB}, but is rarely used for calculations due to its complexity [**1**].

When Peltier discovered that he could produce or absorb heat with electricity, he was not aware it was dependent on the Seebeck phenomena. This was first understood by W. Thomson (later Lord Kelvin) in 1855 [**1**]. He established a relationship between the Peltier and Seebeck coefficients by applying the laws of thermodynamics. He found that the Peltier coefficient was the Seebeck coefficient times the absolute temperature. This relationship indicates that heat is produced or absorbed when current flows through a material with a temperature gradient, also known as the Thomson effect.

$$\pi_{AB} = \alpha_{AB} T \tag{1}$$

The introduction of semiconductors as thermoelectric materials in the 1950's allowed the practical application of Peltier devices. Figure 3 shows a modern Peltier thermoelectric module, this consists of p-type and n-type semiconductors that are wired in series with copper conductors. This system is then connected with a ceramic substrate plate on the top and bottom allowing it to be connected electrically in series and thermally in parallel.

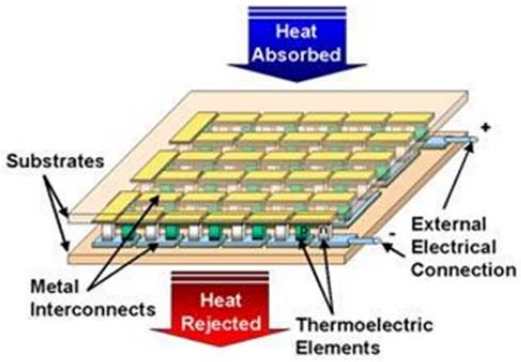

Figure 3: Peltier effect thermoelectric device [2]

When current is supplied to the module, electrons will flow from the p- or n- type semiconductors into the copper conductor. P-type semiconductors are doped with atoms that have fewer electrons than required to complete the atomic bonds in the crystal lattice, where n-type semiconductors are doped with atoms that have more electrons than required. Figure 4 illustrates how the thermoelectric process works. When a voltage is applied, the p-type semiconductor will conduct electrons in an attempt to complete its atomic bond. This process creates holes as the electron flow from the p-type into the copper on the cold side which is at a higher energy level. The energy required to create these holes comes from absorbing heat. Electrons then travel from the hot side copper conductor into the p-type semiconductor, following the path of least resistance. As the electrons move into the holes created on the cold side the heat is rejected.

Meanwhile the n-type semiconductor has more electrons then necessary, when a voltage is applied these electrons move freely into the conductor. The conductor has a higher energy level, from the p-type semiconductor, that the n-type must match. This energy originates from absorbing heat on the cold side. Electrons then move to the hot side of the semiconductor which is at a lower energy level. To match this energy level, the n-type material now releases its absorbed heat and electrons move back to the cold side. There is a complex relationship between the element geometry, number of couples and material properties that define the heat pumping capacity of the module.

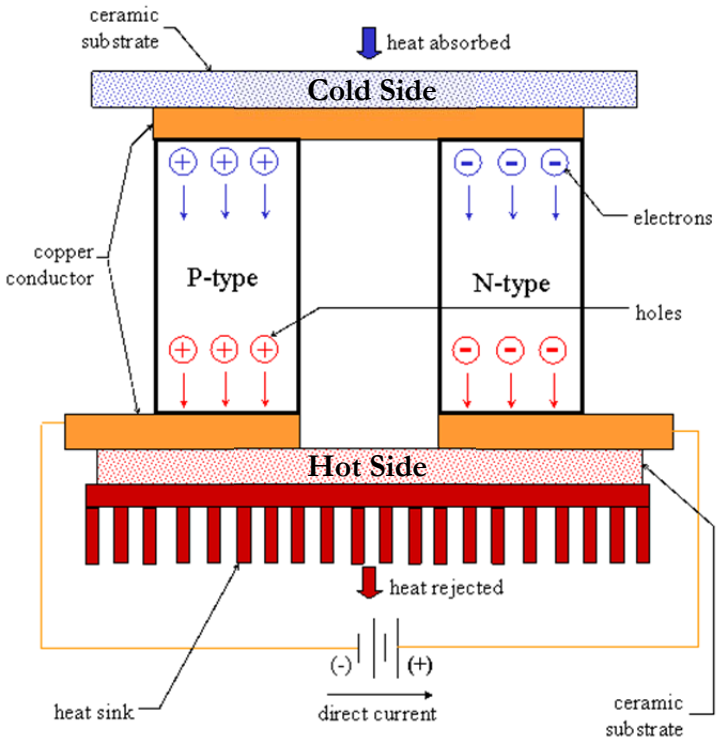

Figure 4: Schematic of thermoelectric cooler [**3**]

The Seebeck effect utilizes the same principles as outlined above with the exception that electricity is extracted rather than applied. When a temperature difference is applied across the p- and n- semiconductors it promotes the flow of electrons as described above. This flow of electrons (current) causes a voltage differential, thus electric power;

$$P = V \cdot I \tag{2}$$

1.2.2. INDUSTRIES AND APPLICATIONS

In the 1960's TE devices were predominately used within the military and aerospace industries. As the technology spread devices began to be introduced into the medical and electronics industries. One of the most recent market penetration areas is within the automotive industry.

1.2.2.1. Military

Modern thermoelectric devices were first used within the military establishments. This industry saw potential in the technology as it has a simple design, lacks moving parts, is quiet and could handle abuse. TE devices began in service as generators since they were able to produce energy silently, an important trait during covert operations. Military vehicles also house electronic equipment that can overheat due to lack of space for cooling equipment. The small size of thermoelectric modules allowed them to fit in the tight confines. Presently, the use of thermoelectrics is found throughout the military ranging among: cooling systems, refrigerators, fans, generators, missile power systems, and avionics equipment [**4**].

1.2.2.2. Aerospace

The aerospace industry helped to develop the initial thermoelectric devices into the present systems. Thermoelectrics have been used by NASA on the Apollo, Pioneer, Viking, Voyager, Galileo and Cassini missions [**2**]. A TE generator used in such missions can be seen in Figure 5. It utilizes heat from a Pu238 radioactive source with thermoelectrics generating electricity for the craft. Such a power source is still operational

in the Voyager after 35 years. Generators are also used on various satellites, space probes and spacecraft to ensure power is always available.

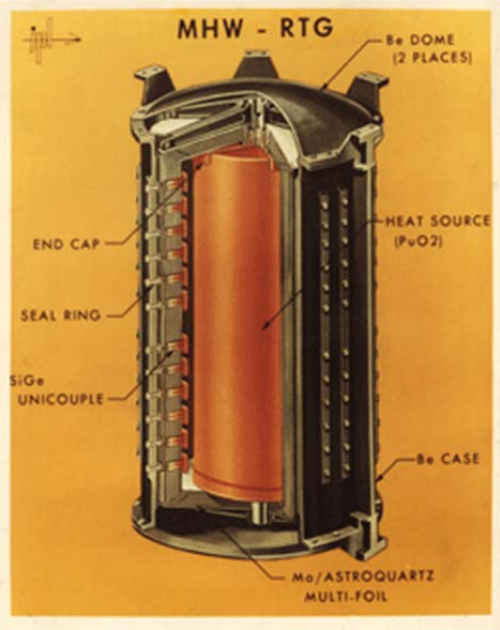

Figure 5: Radioisotope thermoelectric generator

Other uses in aerospace applications encompass cooling of avionics equipment. In the 1960s this was found to be superior to air cooling as it allowed direct cooling to remote locations, eliminated moisture issues, worked while stationary, provided easy maintenance, and was redundant in case of module failure [**5**]. Thermoelectrics are still present in avionics cooling and are now incorporated into other areas of aircraft design including temperature controlled suits for pilots.

1.2.2.3. Medical

Thermoelectrics have seen many uses in various types of laboratory and hospital equipment. For instance Laird Technologies uses thermoelectrics to cool their medical laser applications and indicates "the solid-state assemblies have higher reliability with

fewer moving parts and require less maintenance" [**6**]. TE units are also used in: emergency disaster equipment, survival gear, portable lab and shipping refrigerators, medical coolers and auxiliary power units. The medical industry requires high fidelity temperature control that is achievable with either simple thermoelectric units or highly complex mechanical heating and cooling systems [**6**]. Thermoelectrics have also seen use as heating /cooling blankets when a patient has hypothermia to help raise their core temperature [**7**]. These same blankets can be used to lower a patient's temperature, for instance if they have heat stroke. Having the option to heat and cool with one device saves space and reduces complexity which can be critical in remote locations and for high precision instruments.

1.2.2.4. Electronics

The electronics industry has grown exponentially over the past few decades. With this accelerated pace of innovation come challenges. One of the challenges is to effectively cool the microprocessors installed in tight spaces. Electronic devices can be cooled with heat sinks utilizing the ambient air temperature and convection thermodynamic principles. An increase in cooling demand has made this system inadequate for high power applications, and thus heat pipes and liquid cooling were introduced to augment heat transfer. Thermoelectric technology is an alternative presently being researched to provide enhanced cooling to modern CPU's.

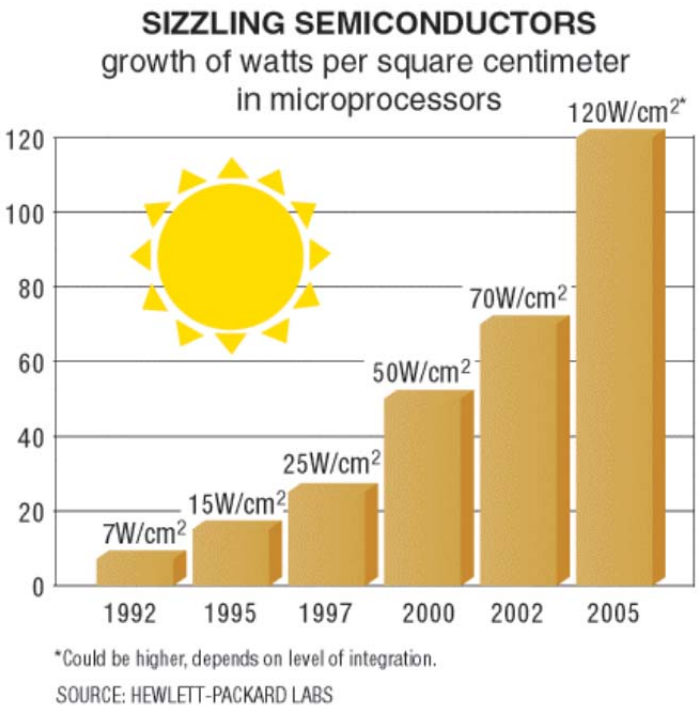

Figure 6: Growth of CPU power density [**8**]

Air-cooling systems unable to maintain cooling demands can be improved by using heat pipes or by switching to a liquid cooling medium. Systems with a liquid cooling medium have heat transfer coefficients between 500-1,000 W/mK compared to 50-100 W/mK for an air-cooled system [**8**]. While this is a benefit such systems require more space and have many components, increasing the cost. Heat pipes are more compact and are currently used in laptops to move the heat from tight locations to ones with more surface area such as the keyboard [**9**]. They can be used in situations where liquid cooling is not feasible due to space restrictions.

Electronic temperature control can be separated into active or passive systems. The systems mentioned above are all passive ones. Thermoelectric based systems offer an active solution that alters the amount of cooling based on overall requirements. This offers better temperature control over passive systems resulting in superior operating

conditions which can prolong the electronics life span. The TE assisted thermal management of computer electronics offers a solution to handle higher heat loads, while capitalizing on heat pipes and liquid cooling systems currently in use by the industry.

1.2.2.4.i Liquid CPU Cooling

TE powered liquid cooling system can either be mounted directly on the CPU, as shown in Figure 7, or through a waterblock, as shown in Figure 8. Typically, the CPU is smaller than the TE module as seen in Figure 7. To overcome this issue, a copper spreader plate is used to disperse heat. This allows the full surface area of the TE module to be utilized improving heat removal capabilities. Hydrocool [**8**] experimented with such a design using one Kryotherm Drift 0_8 TE module running at 24 V. It was possible to maintain a CPU at 25°C while extracting 93 W of heat, while the TE device was consuming 245 W [**8**]. This result gave the system a COP of 0.379. The low COP exemplifies how direct cooling through a TE device is an inefficient means to provide cooling. Although the copper spreader plate has a high thermal conductivity, ~400 W/mK [**10**], it is not as effective as a direct contact liquid heat exchanger, which can have a heat transfer coefficient exceeding 1000 W/m^2K.

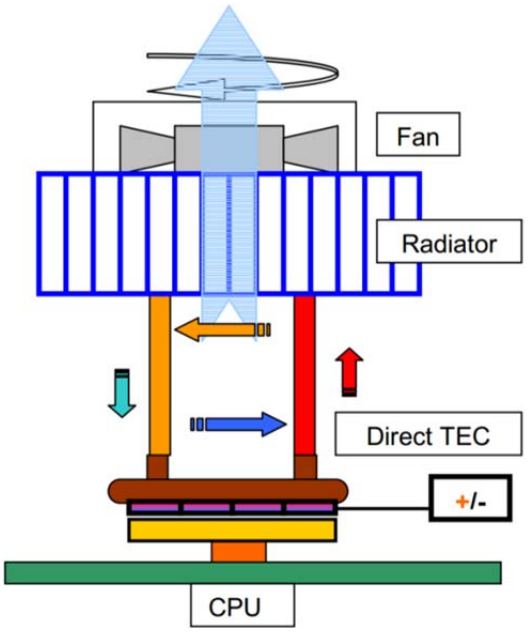

Figure 7: Direct mount liquid cooling system [**8**]

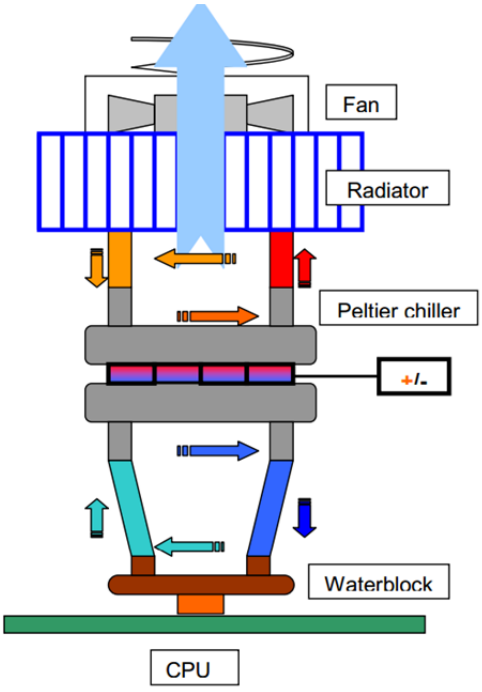

Figure 8: CPU chiller schematic [**8**]

To improve thermal conductivity, a TE based cooling system can use the CPU water block found in typical liquid cooling applications. Heat is transferred from the CPU into the water block directly and the heat is removed from the fluid through an external radiator. To effectively utilize TE's, the fluid will flow from the water block into a TE cooler. The TE cooler will then release the heat through an external radiator as depicted in Figure 8.

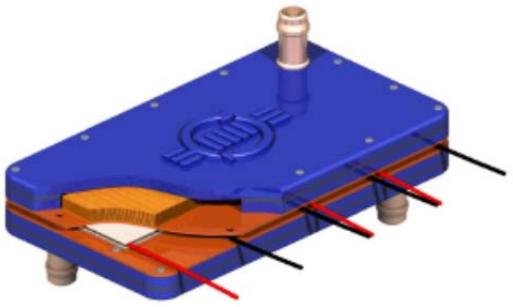

Figure 9: Hydrocool TE cooler [**8**]

The TE cooler developed by Hydrocool, shown in Figure 9, has multiple TE modules which run near their optimal COP. This is an improvement to the previous design which has one TE module that must run at a higher power level to provide sufficient cooling. Hydrocool experimented with this later system by using 4 Kyrotherm Drift 0_8 TE modules each running at 12 V. Experiments showed that the system could maintain a CPU at 25°C by extracting 180 W of heat with a power consumption of 220 W [**8**]. This corresponds to a COP of 0.818 or an increase of 115.8% from the previous design. By improving the heat exchanger design and running the TE modules near their optimal COP, an increase of performance can be realized. In this case, a CPU generating twice as much heat could be installed by the manufacturer.

1.2.2.4.ii Heat pipes

Heat pipes offer a variation to the liquid cooling scheme previously analyzed. Heat pipes are considered an improvement in certain applications due to their compact size, simple design and lack of moving parts. Heat pipes are vacuum sealed components utilizing a fluid that changes state [**9**]. Heat is absorbed through the evaporator causing the liquid to evaporate. The vapour, having a high temperature and pressure, travels to a lower pressure region along a pressure gradient. When it reaches the colder low pressure area the vapour condenses to liquid and travels back to the evaporator through a wick, repeating the cycle. This cycle is depicted in Figure 10. It has been found that heat pipes have a thermal conductivity up to 70x that of copper [**9**], and thus are very effective in CPU applications.

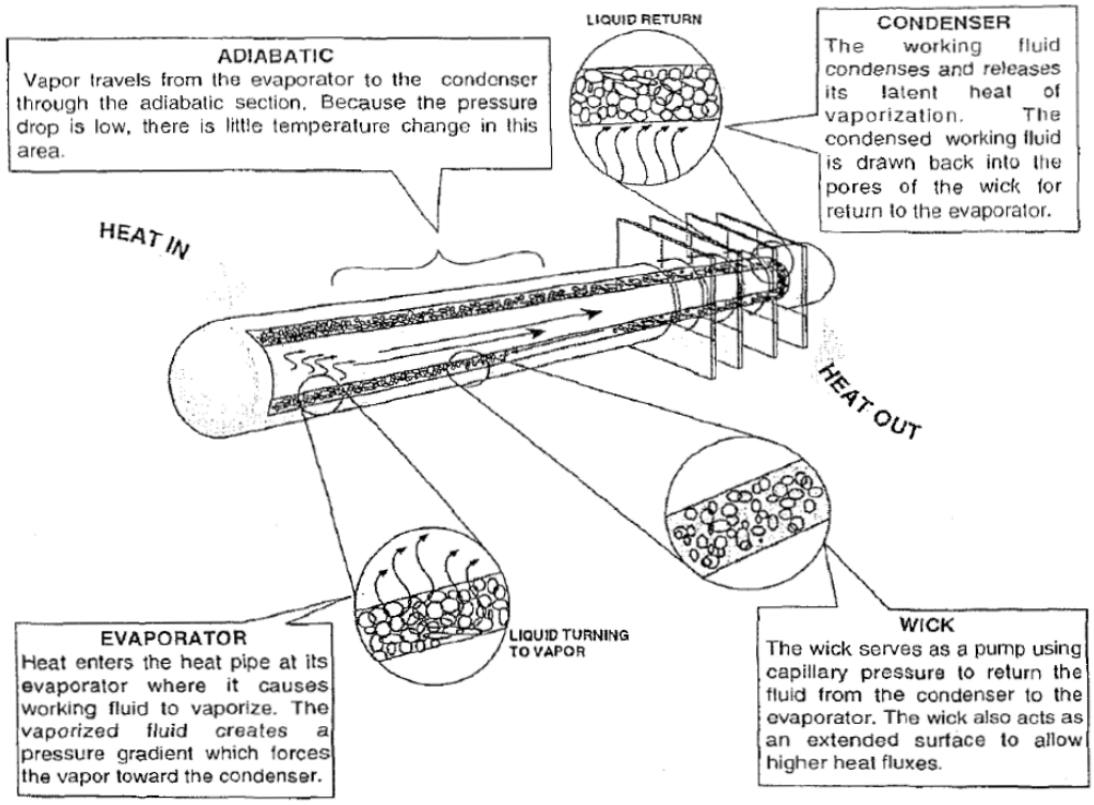

Figure 10: Heat pipe operation [**11**]

The major limitation in most CPU applications is the lack of space. Heat pipes are currently used in many notebook computers as they can transfer heat from the CPU to another location with more space. They are also able to provide high amounts of cooling for systems with multiple CPU's.

A TE system utilizing heat pipes can have a few different configurations. Figure 11 shows an experiment Ikeda et al. [**12**] performed where the heat pipe is between the CPU and TE module. The spreader plate was used to provide an effective surface to transfer the heat from the CPU to the TE module. A finned heat sink is used to dissipate the heat from the TE module using forced convection.

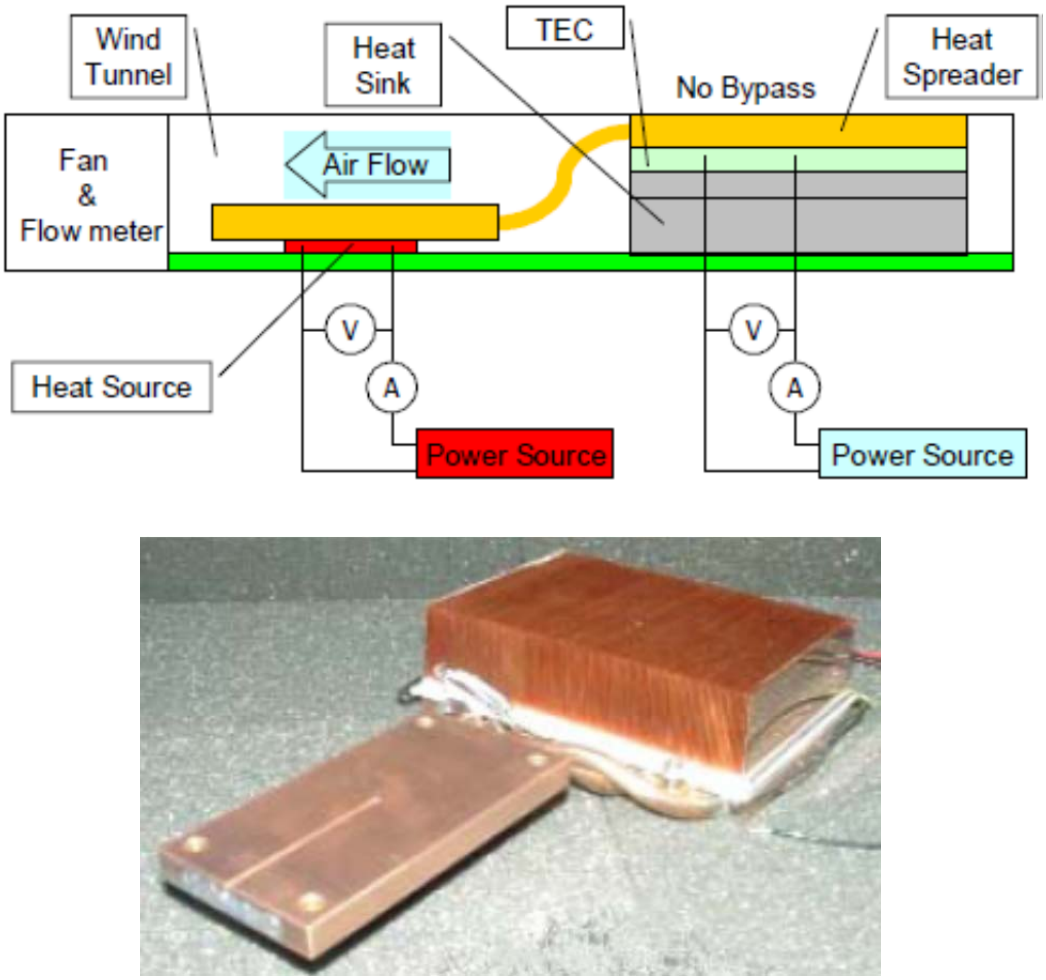

Figure 11: Heat pipe with TEC [**12**]

Some practical experimentation found that the performance of the TE module would decrease as cooling requirements increased [**12**]. The experiment shown in Figure 11 has a COP of 5 with a heat load of 88W and a COP of 2.0 with a CPU heat load of 150W. From this, it can be seen that as the heat loads increase the system efficiency decreases for a given module size. To perform at high CPU heat loads TE modules with larger capacities are required. Due to variance in test conditions, this experiment cannot be taken in direct comparison to previous liquid cooling results.

A second configuration for the TE module and heat pipes is a parallel configuration, as shown in Figure 12. The fluid within the heat pipe system can follow two different paths. The first path holds two 40 x 40 mm TEC modules using cooling fins to dissipate heat. The second path is along four heat pipes where the heat is dissipated by a second set of cooling fins. Both sets of cooling fins use an 80 x 80 mm fan providing forced convection cooling [**12**].

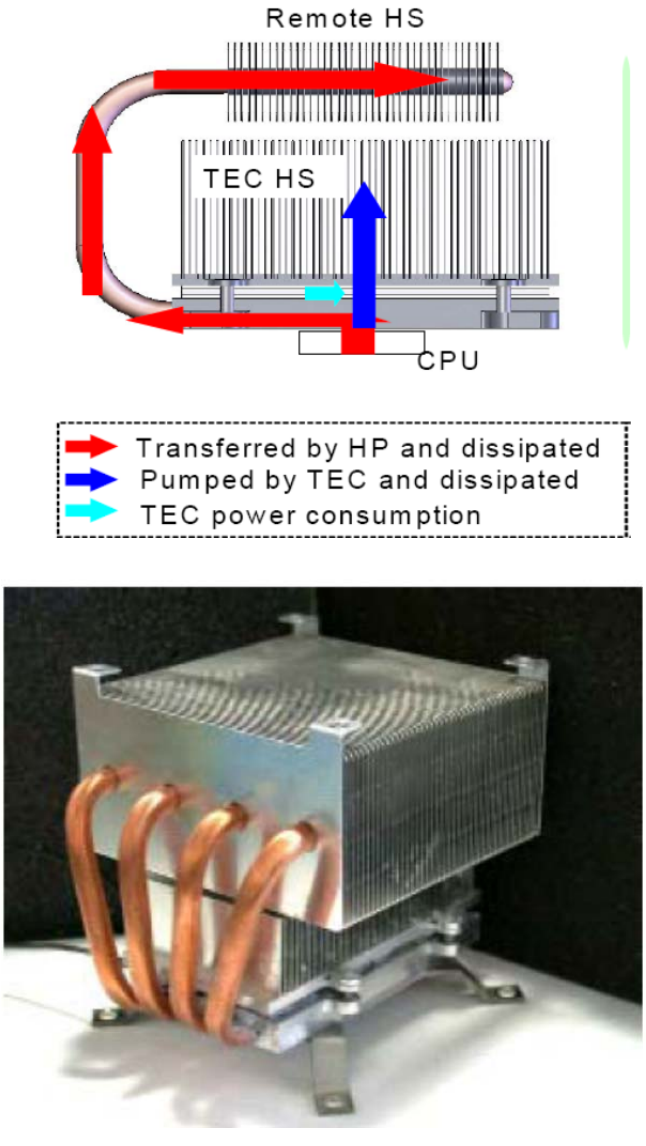

Figure 12: Parallel TEC & heat pipe cooler [**12**]

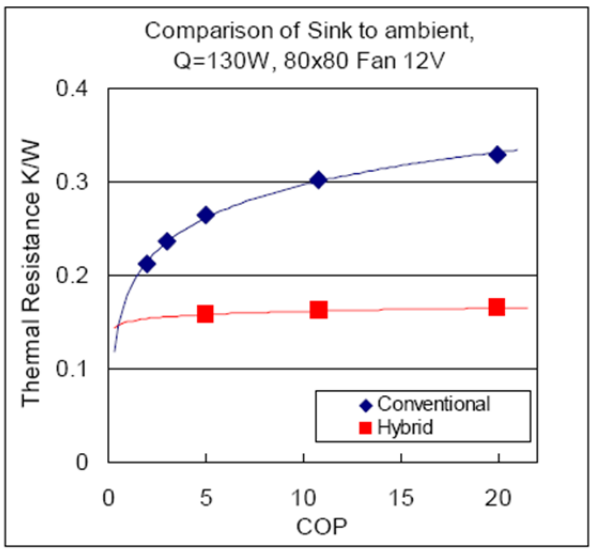

Figure 13: Comparison of thermal resistance at 130W [**12**]

This design maximizes the COP of the TEC by reducing the heat input. The experimental results show that the parallel design produced a COP of 10.8 at a heat load of 130 W [**12**]. Due to lower thermal resistances this parallel design was able to handle higher heat loads than the first design. The graph in Figure 13 shows the hybrid design is able to maintain a stable thermal resistance, while the conventional design requires higher input power to maintain cooling capacity. The improvement in system COP can be accomplished in a variety of ways; a parallel design is just one of them. The designers could have used multiple TE modules as done by Hydrocool or utilized superior heat exchangers. This illustrates how different cooling configurations can achieve the same goal.

1.2.2.4.iii TE Market Barriers

The applications examined above both employ TE modules for cooling CPU's and other electronic devices. TE's offer an alternative thermal management solution to liquid, air and heat pipe cooled systems on the market today. One barrier to their use is the size

of the components as TE devices are generally still much larger than the CPU's they are cooling. The above solutions employed micro channel heat exchangers to improve heat transfer but continued innovation in this field is required. By introducing additional components to the system, complexity and costs increase, these factors must be considered when implementing a TE powered cooling system. Ikeda et al [**12**] performed reliability and thermal shock tests on TE modules, in all cases less than 1% deviation of electrical resistance was found throughout the test cycles. They concluded that the TE modules are able to meet reliability and stress requirements for their case. While TE's offer improvements in certain areas, more development is required before the technology gains full industry acceptance.

1.2.2.5. Consumer Products

Thermoelectrics have only seen minor success in the consumer product sector. In other industries TE's have been successful as a means of refrigeration. This began in the military and aerospace industries where the benefits outweighed the high initial costs of development. Presently TE powered refrigerators can be found in mini-bars, automotive cup coolers, wine coolers and other small appliances that do not require freezing [**13**]. Two companies are researching ways to apply TE modules to the common household refrigerator/freezer. Hydrocool Pty Ltd [**13**] has designed a household size 126L fridge with 36L freezer operated solely through TE modules. Vian and Astrain [**14**] incorporated a thermosyphon into a TE refrigerator in an attempt to improve the overall COP. Both companies are conducting research to determine if TE powered devices can be made comparable in performance and cost to vapour compressor systems. As government regulations on refrigerants become tighter, companies are looking for environmental solutions to common problems. TE devices provide an environmentally friendly

alternative to current vapour-compressor systems. The major limitation to the application of TE modules is their inefficiency and relative low power capabilities compared to present cooling/heating processes.

1.2.2.5.i Liquid cooled TE Fridge

The liquid cooled fridge uses a TE system similar to the one described in the section 1.3.4.1. The system consists of liquid heat exchangers on both sides of the TE module, and fin/tube heat exchangers with fans in the liquid to air locations. All the heat exchangers were developed by Hydrocool Pty Ltd to have low thermal resistances for the low flow rates typically found in refrigerators [**13**]. The project was partnered with Matsushita Refrigeration Company to develop a commercially viable TE powered refrigerator and freezer [**13**]. The target performance requested by the manufacturer is outlined in Table 1 and the experimental unit is shown in Figure 14.

Table 1: Performance criteria [**13**]

Item	**Condition**	**Target Performance**	**Hydrocool Performance**
Cooling Power	30°C ambient	Freezer: -25°C Fridge: 0°C	Freezer: -25°C Fridge: 0°C
Energy Consumption	25°C ambient 5°C in fridge -18°C in freezer	490 kWhr/yr	513 kWhr/yr
Noise	1m from front 1m above floor	20 dB	23 dB
Defrosting	30°C ambient	No performance dew clogging freezer	Complies at 25°C, 70%RH
Dew condensation	30°C ambient , 85%RH, 5°C in fridge, -18°C in freezer	No dew on fridge surface	Complies
Parts cost		170 USD	218 USD

Figure 14: 126L refrigerator/freezer [**13**]

Through initial experimentation, it was found that heat loads within a conventional fridge were too high for the TE modules to handle. To reduce the heat loads within the refrigerator they had to improve its design. The dry pipe used to remove humidity was given an intelligent controller allowing it to turn on when required, rather than running continuously. Vacuum insulation panels were used in the freezer, in place of conventional polyurethane insulation to reduce conductive losses. They also chose to transfer the heat from the freezer into the fridge compartment rather than expel it directly into ambient conditions. These enhancements allowed a reduction of the freezer ΔT from 43°C to 23°C, enabling the four TE modules to run close to their optimal COP [**13**]. The modules used during testing were Kryotherm Frost 75, capable of 55 W at 16.8 V. The heat transfer fluid was Freezium, (a brine solution) which is liquid, rated to -50°C and has a specific heat of 2.78 kJ/kg°C [**13**]. The TE modules are controlled by a PID controller

allowing the system to adjust to ambient environmental conditions. This means the TE modules are never cycled on and off, which provides accurate internal temperature control.

Proper testing of the system includes running under steady state and extreme conditions. To test under extreme circumstances refrigerator manufacturers have developed a test with the ambient temperature set to 35°C and humidity at 85% [**13**]. The fridge is filled with bottles of beer and the freezer with ice cream. Over a 12 hour period the fridge is opened and cold bottles are replaced with warm ones. After 12 hours the system must be able to recover. In the recovery test the total heat load was 26.0 W with 58.6 W of AC power consumed, giving an overall COP of 0.44. During the performance test it was noted the TE refrigerator performed at a level similar to a compressor driven system [**13**]. The performance results of the Hydrocool refrigerator can be seen in Table 1. This table indicates that the system met the cooling power, defrosting and dew condensation targets while energy consumption, noise and cost were above targets by 4.7%, 15% and 28% respectively. Despite not meeting the stringent performance targets, this research shows that there is potential for TE devices as a means for consumer refrigeration.

1.2.2.5.ii Thermosyphon Fridge

Thermosyphons operate under the same theory as heat pipes with a condenser and evaporator. Thermosyphons, however, rely on gravity to return the condensed liquid to the evaporator rather than a wick [**10**]. This limits the use of thermosyphons to situations where gravity can be utilized. The thermosyphon porous medium (TPM) used in a refrigerator is shown in Figure 15. The main concept behind the TPM is to reduce

thermal resistance which results in a higher overall COP. The TPM works with butane ascending the porous medium through capillary action increasing the surface area for heat transfer [**14**]. Heat is absorbed as the butane ascends converting it to a gas. This gas travels to the cold side of the TPM where the Peltier module is attached. The Peltier module condenses the butane and gravity causes it to return to the bottom of the TPM, then the process is repeated [**14**].

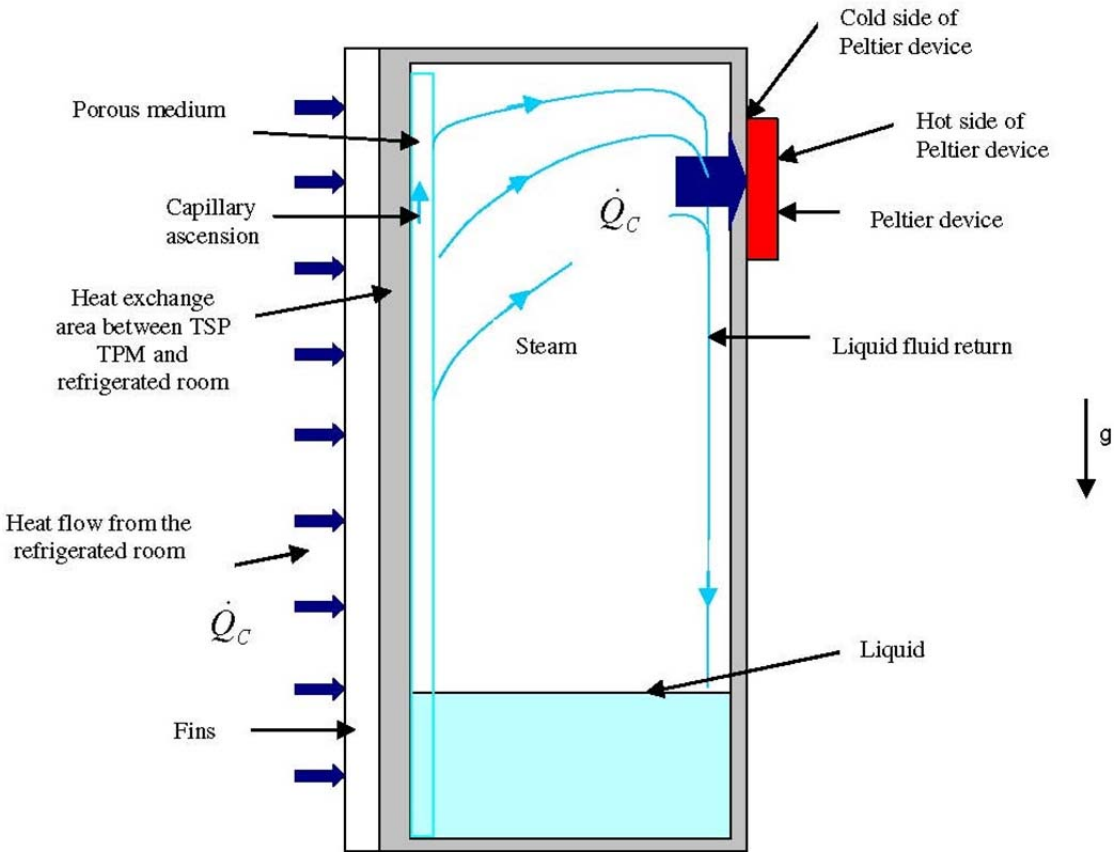

Figure 15: Air-cooled thermosyphon [**14**]

The experiment that was conducted by Vian and Astrain [**14**] consisted of one TE module running at 21°C ambient. A Marlow Inc. 6L TE module capable of 50 W maximum power at 12 V was used. The test ran until the temperature stabilized. To

benchmark the system a test was performed with a standard finned heat exchanger currently found in TE cooling devices on the market. Table 2 summarizes the findings.

Table 2: TPM results

	TPM	Finned Heat sink
T_{amb}-T_{int}	11.2	8.43
Q_c (W)	19.47	14.67
W_e (W)	49.6	49.4
R_{tot} (K/W)	0.323	0.513
COP	0.393	0.297

These results show that the overall thermal resistance is reduced significantly when the TPM replaces the finned heat sink, improving the COP of the system by 32%. However, the COP of the refrigerator with the TPM is only 20% of a standard vapour compressor system. The lower COP limits the commercial appeal of the TE powered device. To become commercially viable, improvements to system efficiency are required. In comparing results from both TE powered refrigerators, the TPM was unable to perform as efficiently as the Hydrocool system, however it is a low cost approach. Hydrocool showed that operating a larger number of modules at lower power consumption improves system efficiency. The Hydrocool system uses four TE modules while the TPM uses a single one. By increasing the number of TE modules in the TPM an improvement to system efficiency could be achieved.

1.2.2.5.iii Challenges

The practical research presented shows how difficult it is to overcome the inefficiencies present in TE devices. Typical household vapour compression systems have COP's of 2-3 [**1**], while the Hydrocool fridge has an experimental COP of 1.15 [**13**]. This is only half of a vapour compression system, but is a drastic improvement over previous designs. It must be remembered that as the mechanical systems are made smaller, their COP also reduces, and can drop below 2.0. In order to compete with present designs the figure of merit and COP values of the TE modules must be improved. Davis et al [**13**] have shown that the cost of a TE fridge can be competitive with existing systems if the production volume is present. The noise level of the TE system can be superior to a traditional fridge with some minor adjustments to the fans and other mechanical components. Reliability is also a concern in any application; Hydrocool performed an accelerated reliability test on nine modules and found that none suffered any performance degradation. They also found that several modules exceeded 10 years and one exceeded 20 years simulated service [**13**]. The highly adaptive control, cost targets, noise levels and tested reliability gives perspective to the potential for TE controlled refrigerators. TE devices have shown they can provide the cooling capacity, and with some improvements in efficiency could offer similar operating characteristics to a vapour compression refrigerator. They are especially suited at the small scale where mechanical systems become increasingly inefficient due to losses stemming from surface area to volume relationships.

1.2.2.6. Automotive

The automotive industry is currently attempting to reduce emissions while improving vehicle efficiencies. Vehicles are also becoming more complex with additional comfort

and convenience features frequently being added. There is simultaneously a shift to the electrification of the automobile causing the redesign of many key components, which were historically driven through mechanical means. Thermoelectrics have unique characteristics that allow them to work well in the evolving automotive market. TE modules have been used in the luxury vehicles for the past decade in: seats, cup holders and cooler/heater compartments [**15**]. More recently, there has been an attempted expansion in their applications to: waste heat recuperative generators and localized zonal heating (HVAC). As the automotive industry continues to evolve and regulations require vehicles to be more fuel efficient, TE technology is one path manufactures can take to deliver advances.

1.2.2.6.i Automotive Seat Temperature control

Consumers are continually asking for more convenience features in their vehicles. Gaining popularity is the addition of temperature controlled seats. The best of these seats have heating and cooling devices that allow each passenger to control their temperature. Thermoelectrics provide a solution as they can be used for both heating and cooling. The concept was first introduced by Amerigon in 1999 and currently exists in 50 different vehicles on the market today [**16**]. There are a variety of manners in which TE technology has been incorporated into seat temperature control. Figure 17 shows a design that has TE modules mounted to the seat, transferring the heat or cold directly to the passenger, while also providing massage functions through shape memory alloys. Figure 16 shows the Climate Controlled Seat (CCS) seat by Amerigon which utilizes a heat exchanger with a fan to provide either hot or cold air. There is one heat exchanger located in the seat back and another in the base; together they provide heat/cool air throughout the entire

seat surface. The advantage to these designs is they can provide hot and cold surfaces, while other technologies can only heat the occupant.

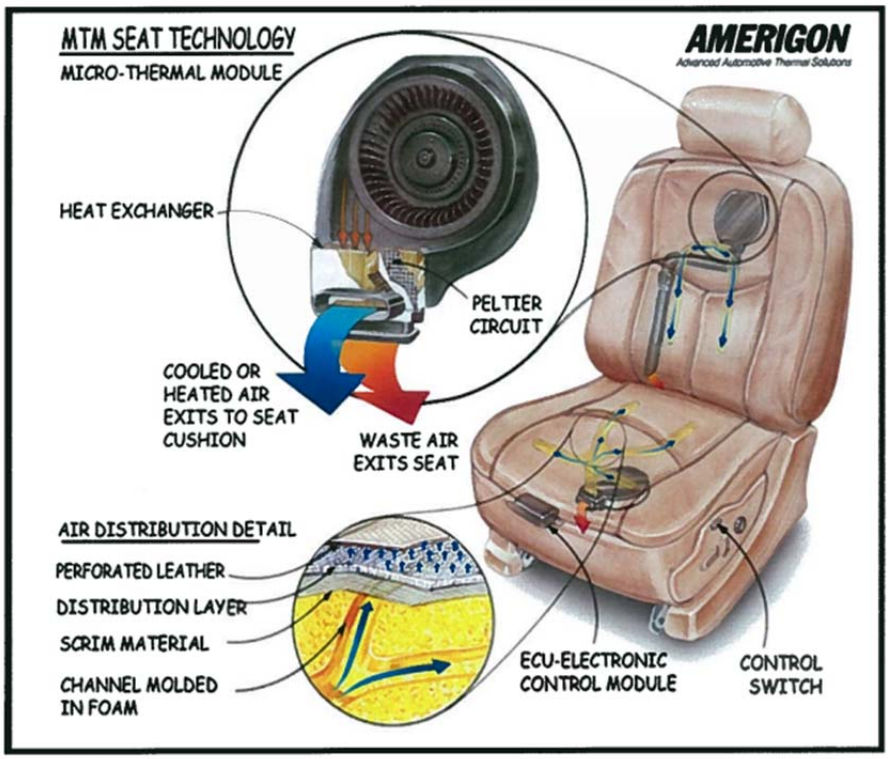

Figure 16: Climate Controlled Seat by Amerigon [**17**]

Figure 17: Iterative temperature control seat [**18**]

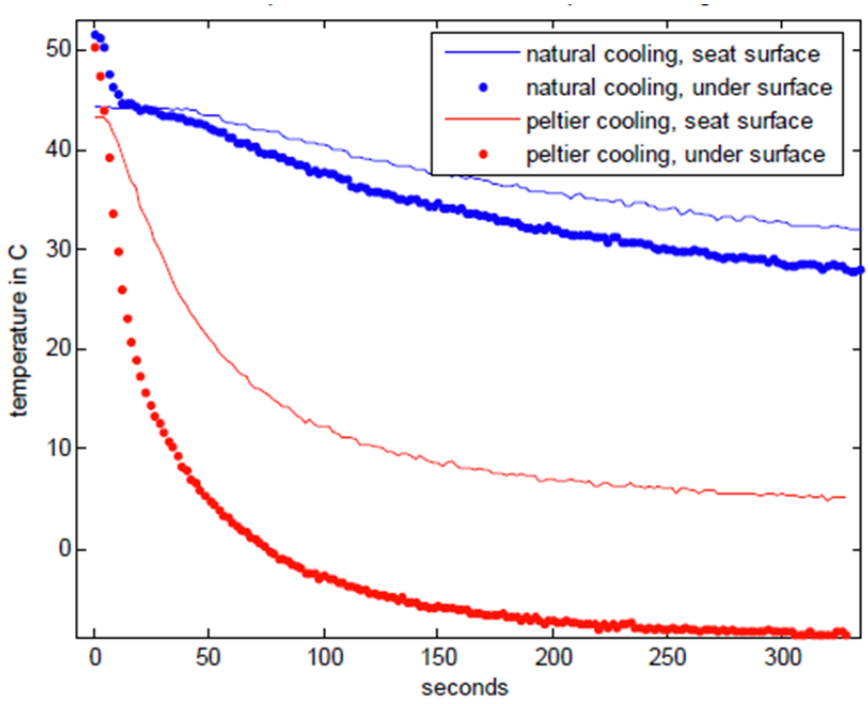

Figure 18: Comparison of natural and Peltier cooling [**18**]

Figure 18 shows the Peltier cooled seat can reach 90% of its peak cooling capacity within 100 seconds, while providing ~20°C cooling below ambient conditions. This effectiveness has led to the widespread use of TE temperature controlled seats. Since the introduction of the CCS seat in 1999 Amerigon has seen a steady increase in the installation of their seat design as depicted in Figure 19. Such market growth can be attested to the benefits that the TE temperature controlled seat provides [**17**].

- CCS is modular and can be integrated into most conventional seats
- Allows each passenger to control their own seat
- System is solid state and has a modular controller
- Adds comfort with very low energy consumption
- Failure rate is a factor of 100 less than traditional cooling systems

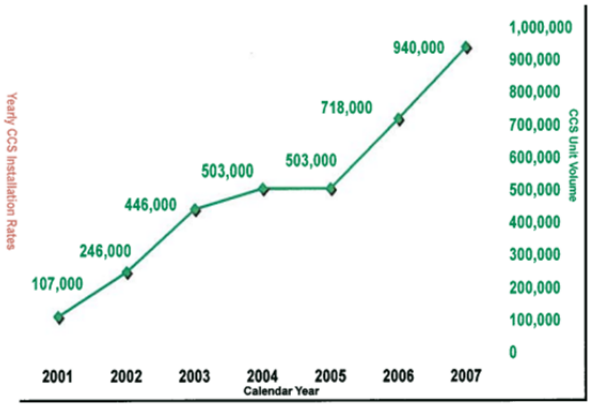

Figure 19: CCS seat installation rate [**18**]

TE temperature controlled seats are primarily a convenience feature that customers use. On their own they offer slight improvements in fuel efficiency and emissions by way of lessened A/C use. If included as part of a TE powered HVAC system design, there is potential for greater improvements to overall vehicle efficiency, fuel economy and emissions.

The popularity of the CCS seat has led Amerigon to become the largest commercial consumer of TE cooling modules. As with most automotive technologies, implementation starts in the luxury brands and gradually moves towards becoming a standard feature. Temperature regulated seats thus offer an avenue for manufacturers to improve vehicle efficiency by reducing the load on the HVAC system. Provided that the heat removed is directly expelled to the vehicle's exterior (presently this is not the case).

1.2.2.6.ii Automotive HVAC Systems

The modern vehicle HVAC system shows minimal improvement from historic systems. To provide heat inside the cabin waste heat is taken from the engine and goes into the cabin heat exchanger. Cold air is provided by an A/C compressor system filled

with a refrigerant that flows through a cabin evaporator as shown in Figure 20. Both systems use either ambient or cabin air to circulate past the subsequent heat exchanger, which is then diverted through a network of ducts to different areas of the vehicle. System inefficiencies are introduced due to the use of one centralized source to heat/cool a very large volume [**15**]. With the introduction of both electric and hybrid vehicles (HEV) these systems have to be adapted to work when the engine is not running, requiring mechanical driven compressors to be converted to electric. A/C and heating systems may use around 3 kW of power [**19**] and can significantly reduce an EVs range. Government regulations are also banning the use of R-134a refrigerant due to concern over harmful greenhouse gas emissions. Europe began phasing out R-134a in 2011 and requires all new vehicles to use an environmentally friendly refrigerant by 2017 [**20**]. TE modules offer an alternative to A/C compressors and heating loops as they do not use refrigerant gases and run directly off DC power.

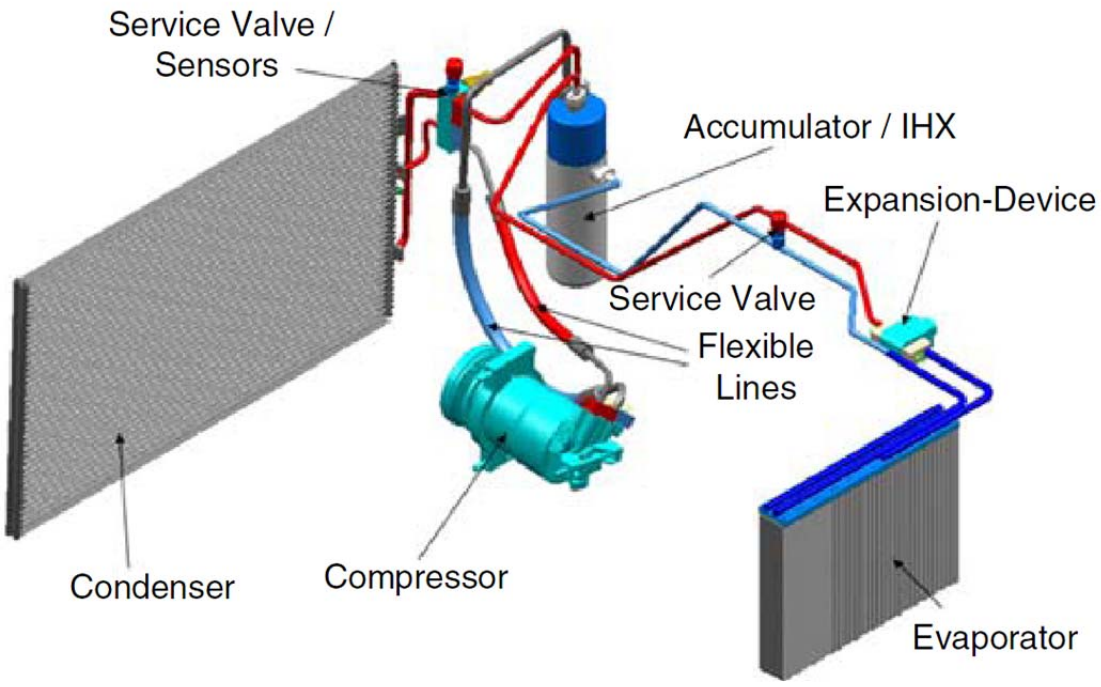

Figure 20: Modern HVAC A/C system [**19**]

1.2.2.6.ii.a. TE Radiator

Research is currently being conducted to replace existing HVAC system with one utilizing TE modules. There are two options being explored: the first is a direct replacement of the A/C module with large TE modules, and the second uses multiple TE modules placed throughout the vehicle. Junior et al [**19**] tested a TE heat exchanger that replaced the main A/C system. The TE device is shown in Figure 21; the working fluid travels through the heat exchanger where the TE modules absorb or supply heat.

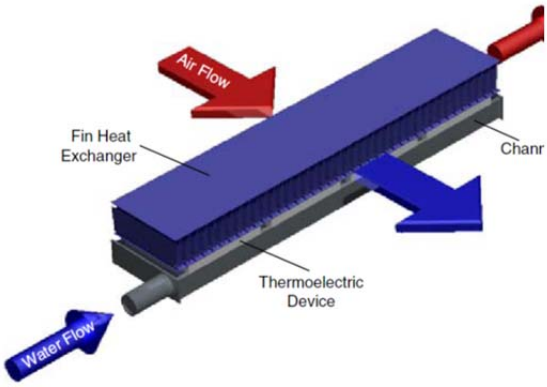

Figure 21: Prototype TE Heat Exchanger [**19**]

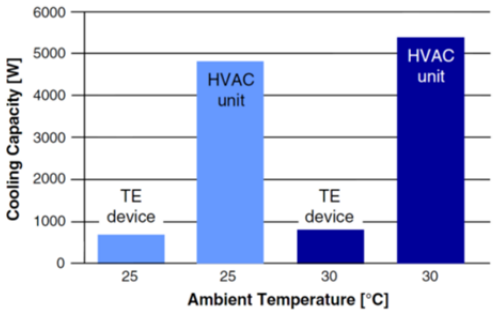

Figure 22: Comparison of HVAC vs. TE powered device [**19**]

Experimentation results confirmed that with current TE efficiencies the system was only able to provide 750 W of cooling [**19**]. A comparison between a modern HVAC and TE powered device is shown in Figure 22. In both cases the TE device was only able to provide approximately 20% of the standard HVAC's cooling capacity. At this time using TE's as a direct replacement of A/C compressors is not practical due to the small cooling capacity.

1.2.2.6.ii.b. TE zone control

The use of seat heating has shown that direct contact with the occupant can reduce power consumption [**21**]. By controlling individual zones within the vehicle the overall heating/cooling loads can be reduced. Installing multiple TE heating/cooling modules throughout the vehicle can accomplish this task.

Figure 23: Zoned HVAC control [**17**]

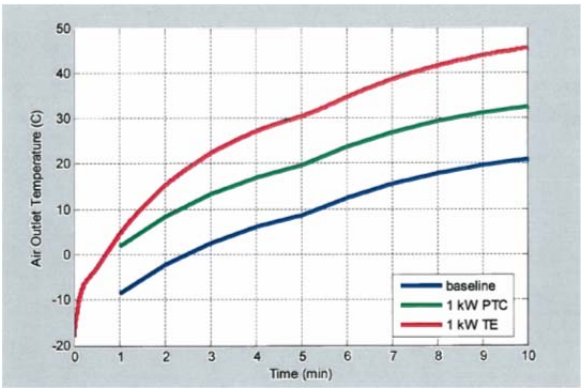

Figure 24: Comparison of HVAC heater performance [**17**]

A cabin with simulated zonal heating using TE modules is shown in Figure 23; each area would have its own TE module which gives the occupant individual control over temperature. This leads to a reduction in load on the system as only the occupied areas would be in operation. The specific location of the individual modules has an effect on the amount of cooling necessary. Sensory receptors in the human face are highly sensitive to temperature change [**21**]. Therefore by directing small amounts of hot or cold air to an occupant's face, the perception that it is warmer or colder than the actual environment can be given. This would allow the HVAC system to run at a lower setting, contributing to an overall reduced load on the vehicle. However the headliner zonal depth is optimistic since cool air also implies a need for heat rejection opposite the cool source, and such systems require packaging space and fans in reality.

Thermoelectrics are more efficient when providing heat compared to cooling due to heat pump characteristics. TE devices extract thermal energy from the environment in addition to the electric energy consumed within, leading to COP values in the range of 1.0-3.0 [**17**]. Presently the common method to generate heat without a combustion engine is with a resistive heater. The limitation of this design is a maximum COP value of 1. Bell [**17**] performed an experiment comparing a typical diesel engine, a resistive (PTC) heater and a TE module. The test was performed at -18°C and the temperature was measured on the outlet of the heating duct.

Figure 24 shows how the TE module was able to outperform both the PTC and stock heater. The TE module reaches 20°C in 2.5 minutes, while the diesel engine and PTC heater require 10 and 5 minutes respectively to reach the same temperature. The TE module would require 60% less energy to perform at the same level as the PTC heater, thus improving the overall efficiency of the system [**17**]. Despite having superior performance when providing heat, limitations to market entry remain, although as performance improves and regulations become stricter TE devices look increasingly promising.

1.2.2.6.ii.c. Market limitations

Automotive HVAC systems offer an opportunity to improve fuel economy and emissions. As with most automotive components, size and cost are the most critical to implementation. An experimental TE heat exchanger was shown to supply only about 20% of the necessary cooling power for a vehicle. The size and cost to implement a TE powered air conditioner prevent it from being a practical solution for automotive applications. The TE zone temperature control promises a more practical solution while

keeping size and cost under control. The main concern over zone control is the ability to provide adequate heating/cooling. To verify performance, additional experimentation is required. One of the benefits to zone heating is the removal of the bulky A/C and heating elements located in the dashboard. The TE system is much lighter and will help to reduce overall vehicle weight, Lofy and Bell [**21**] state "A weight reduction of 90 kg improves fuel mileage by 1 mpg." In the case of a small car, such weight saving can have an impact on fuel economy and emissions.

1.2.2.6.iii Waste heat power generation

Modern combustion engines are still inefficient in the conversion of thermal energy into mechanical energy. The combustion cycle converts only about 30 % of the thermal energy into useful mechanical energy. 40% is expelled as heat through the exhaust and 30% through the radiator as seen in Figure 25 [**22**]. Thermoelectric generators (TEG) can use this waste heat to generate electricity, which can in turn be used to run ancillary systems and remove load from the engine. Park et al [**22**] calculate that if 10% of the waste heat is converted to electricity the fuel economy can improve up to 20%. As fuel economy targets continue to rise TEG's offer a potential solution to reduce fuel consumption. TEG's have been designed to work with waste heat from both the exhaust and radiator. BMW is one manufacturer that has done extensive research and development on the subject and found that introduction of a TEG can reduce CO_2 emissions by 4% to 8% [**17**].

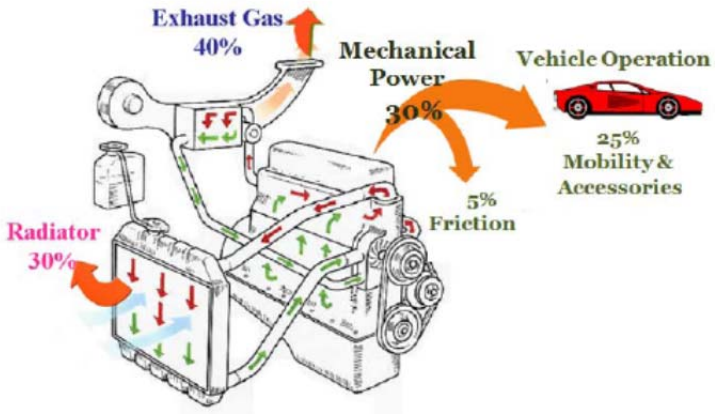

Figure 25: Energy split in internal combustion engine [**22**]

1.2.2.6.iii.a. Radiator TEG

A vehicle's radiator is designed to ensure that engine temperatures are maintained within an acceptable range. Radiators expel the excess heat into the environment through a large heat exchanger surface at the front of the vehicle. Park et al [**22**] developed and tested a TEG that takes the place of the radiator and is able to utilize this excess heat by converting it into electricity. Their prototype can be seen in Figure 26, it's made with 72 TE modules, a liquid heat exchanger and 128 heat pipes. The heat capacity of this system is comparable to that of a conventional radiator and with experimentation it was able to extract 75 W of electricity at 80 km/h, and 28.5 W while stationary.

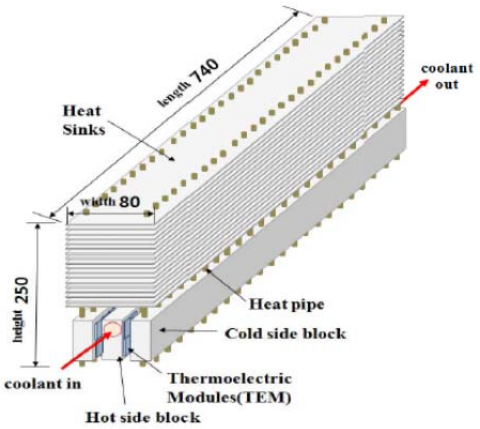

Figure 26: Engine Coolant TEG [**22**]

Through testing of the radiator design, the TEG was only able to extract about 0.4% of the waste thermal energy. The system would require significantly more TE modules to be useful within a vehicle. The addition of more modules requires space and adds to the overall cost. To reach the 10% goal as stated above, the overall cost and size would become impractical for use within a vehicle.

1.2.2.6.iii.b. Exhaust TEG

The exhaust system provides a much better medium to convert heat to electricity due to the higher temperatures. Exhaust systems typically operate between 500°C and 900°C in light duty vehicles and 500°C and 650°C in heavy duty vehicles [**23**]. The recent advancement of TE materials allows the heat to be extracted in a more efficient manner. The location of the TEG within the exhaust system is important, the ideal location of a TEG is downstream of the catalytic convertor to avoid affecting the latter's performance. The power output of the TE module increases with the exhaust temperature as seen in Figure 27.

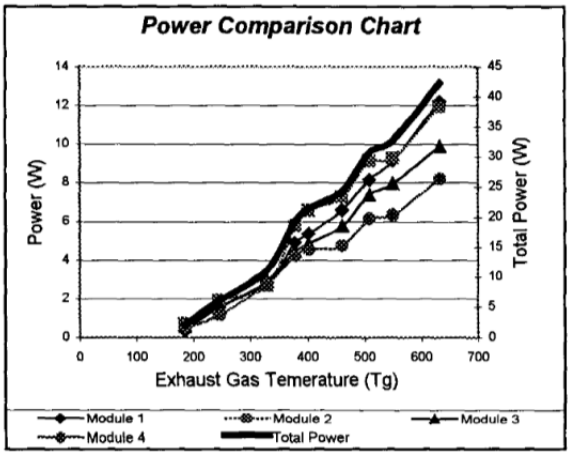

Figure 27: TE Module performance [**24**]

Haidar and Ghojel [**24**] tested a TEG on a Ruston 3YDA diesel engine. The test used four HZ-14 TE modules attached to the exhaust and cooled through the engine's radiator. The experimental results are shown in Figure 27. 42.3 W of power was extracted, which corresponded to 5 % of the thermal energy present. While this number still seems low compared to the overall heat loss, it is an improvement over the 0.4 % converted by the TEG radiator. A 2.2L engine's alternator was also tested to determine the necessary power a TEG would need to produce in order to act as its replacement. The alternator had a maximum output of 980 W, which is equivalent to seventy HZ-14 modules. The price of each HZ-14 module was quoted as US $175 which brought the total cost to US $12,250 [**24**]. This is excessively high and not representative of a production quantity, but it offers some insight as to the difficulty of implementing TEG's economically.

1.3. METAL FOAMS

To effectively utilize thermoelectrics as a heating and cooling source high efficiency heat exchangers must be devised to maintain a commercially viable COP. The small footprint of the TE module limits one to using the most high efficiency heat exchangers available. Ozmat et al [**25**] have conducted research on the effectiveness of high efficiency metal foam heat exchangers. This section will review the background of the technology and its current applications.

1.3.1. BACKGROUND

Metal foams are a relatively new technology that was first introduced in 1967, but didn't see commercial acceptance until the 1990s when it was used for structural applications [**26**]. Metal foams have a unique combination of properties, from their high stiffness to low weight, high permeability combined with high thermal conductivity and

an ability to be manufactured from various materials. [**27**]. They have a basic cellular arrangement that can be found in many different areas of nature as structural members; trees and plants are examples. There are two different types of metal foams, closed cell and open cell, both used by industry today due to their improved characteristics when compared to their solid equivalents. Open cell foams are the focus of this work due to their effectiveness in heat exchange applications. Open cell foams offer increased surface area, have a high coefficient of thermal conductivity while still allowing easy fluid flow through its structure. Foams are generally characterised by the following three main specifics: pore size, relative density and base material [**28**]. The most effective open cell foam for heat exchange is reticulated metal foam due to its open structure allowing the ease of fluid transfer. The difference between standard open cell foam and the result of reticulation can be seen in Figure 28. The reticulation process removes excess material in the polygon shape leaving only the ligaments, thus creating a material with a large surface area and high porosity. These are both ideal characteristics for a high efficiency heat exchanger.

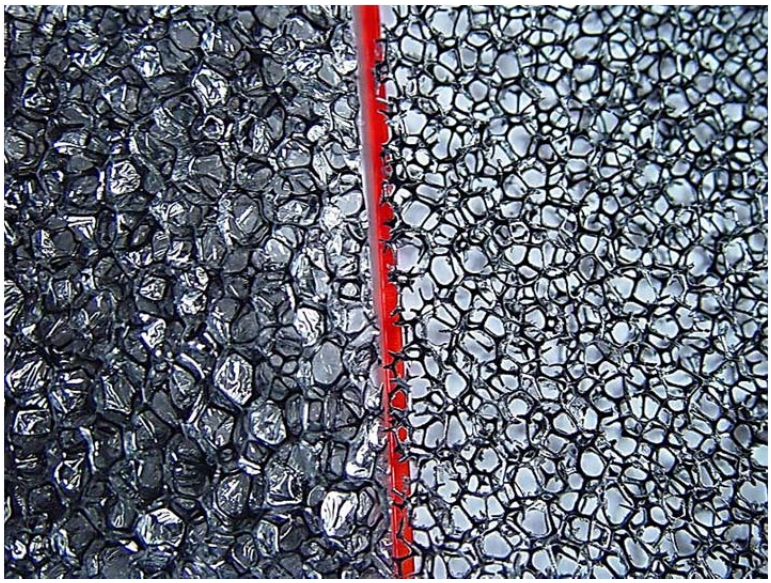

Figure 28: Open cell foam before reticulation (left), after reticulation (right) [**29**]

The surface area of the foams is based on the pore size and density of the material. Figure 29 shows the relationship between these values. The main concern of increasing the surface area is the impact on pressure drop through the foam. Ozmat et al [**25**] have shown that the pressure drop is similar to louvered, plate and pin finned heat exchangers.

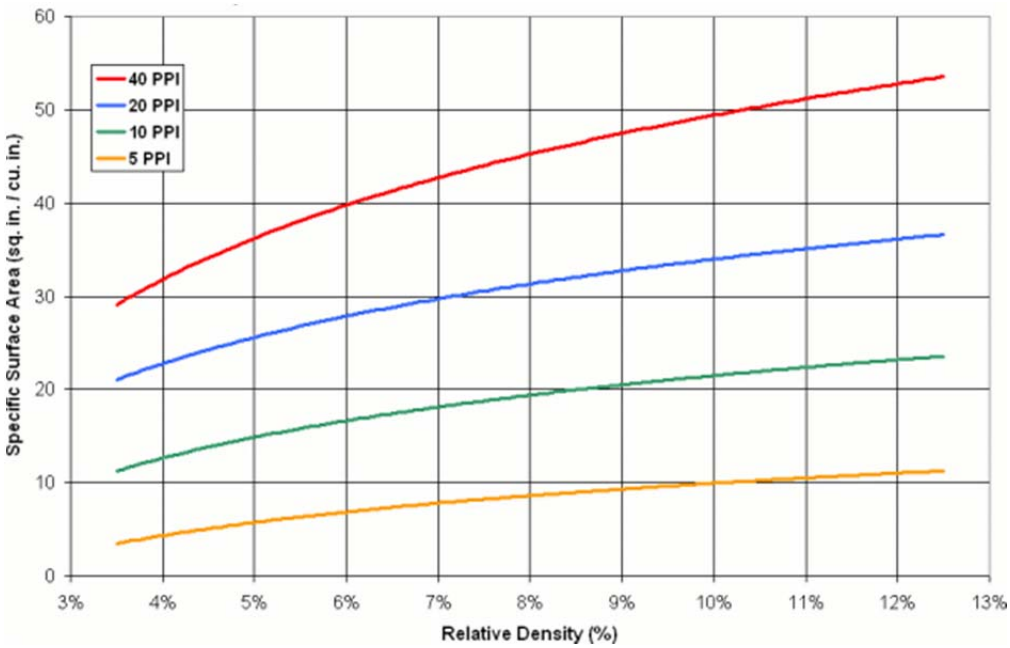

Figure 29: Specific surface area for Duocel® Metal Foams [**28**]

The pore size of the foam is determined during reticulation. Each bubble structure (cell) typically has 14 sides and has the Tetrakaidecahedron shape shown in Figure 30. In any given cell there are multiple pore sizes; for material design these are simplified to an average size and circular shape. The number of these pores that extend one inch defines the foam pore size, the standard unit of measure is pores per inch (PPI) [**28**].

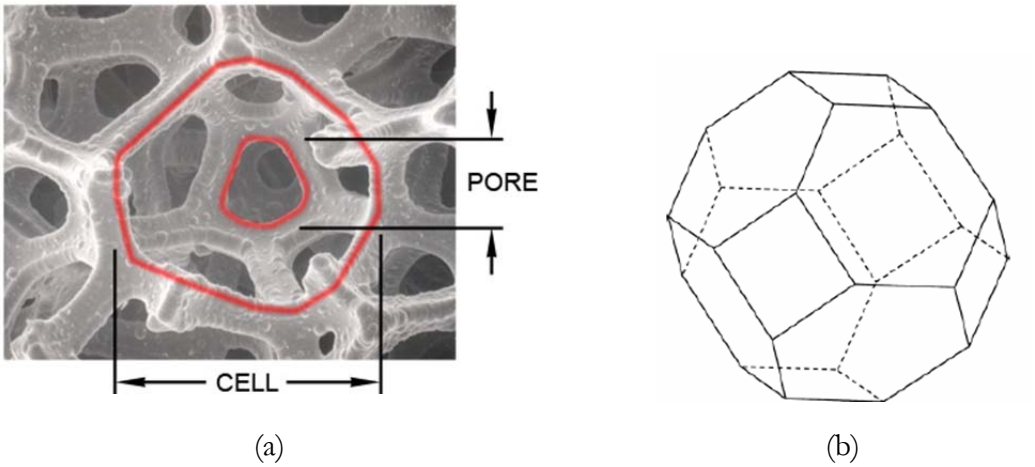

Figure 30: (a) Single Tetrakaidecahedron, (b) Idealized Tetrakaidecahedron [**30**]

The pore size has a direct relationship to the ligament length, cross section, and pore diameter. These parameters will affect the amount of material, weight, surface area and flow resistance. All of these characteristics play an important role in the overall effectiveness of a heat exchanger and must be taken into consideration. Figure 31 shows the difference between 10, 20 and 40 PPI foam. As seen, there is a significant increase in material in the 40 PPI foam compared to its 10 PPI counterpart.

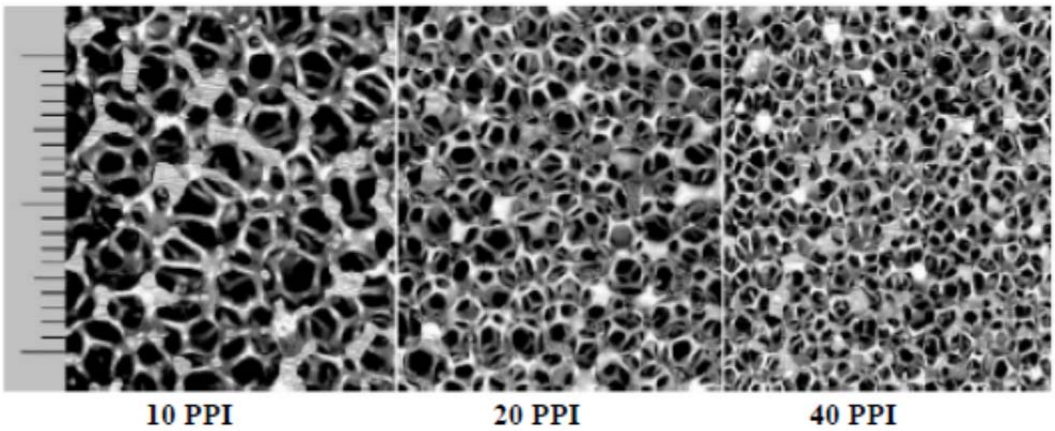

Figure 31: Various aluminum foam pore densities with a graduated mm scale [**30**]

Relative density also plays an important role when determining the proper foam for a given application. The relative density is defined by the density of the block of foam compared to the density of the block in solid form.

$$\rho = \frac{\rho_f}{\rho_s} \tag{3}$$

The relative density has the largest effect on the cross section of the ligaments, whereas the pore size mainly affects the number and nominal size of these ligaments. As the density increases, the ligament cross section goes from a triangular shape to one that resembles a circle, as shown in Figure 32. This can play an important role in the thermal conductivity of heat exchangers as the thermal properties scale with densities.

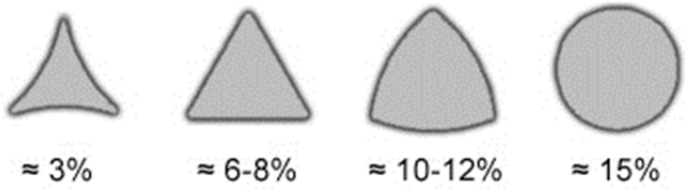

Figure 32: Ligament cross section [**28**]

The third general characteristic is the foam base material; the material chosen depends on the given application. For heat transfer applications the typical materials are aluminum and copper due to their superior thermal conductance. In this thesis, testing is performed on both materials to determine which provides superior heat transfer as a foam.

1.3.2. INDUSTRIES AND APPLICATIONS

Reticulated metal foams were initially developed for structural applications in the 1990s. Their low weight coupled with high strength made them attractive for many applications but high manufacturing costs limited their use to aerospace, ship-building and

defense. Recently new methods have been developed to lower manufacturing costs and introduce new opportunities for RMF's. Some of their current applications include aircraft wing structures, catalytic surfaces for chemical reactions, core structures in high strength panels, containment matrices and burn-rate enhancers for solid propellants and heat exchangers in the electronics industry [**31**].

1.3.2.1. Electronics

Section 1.3.4 discussed how the rapidly expanding electronics industry requires the development of new thermal management principles to achieve the necessary cooling. RMF-based heat exchangers allow engineers to develop new technologies generating higher heat loads, as there is a method to remove the heat. Past HX designs were based on a typical fin-pin array to remove heat but as power demand increases they have become insufficient. RMF's provide a larger heat exchange surface in a smaller volume. For example, 1 cubic inch may provide up to 400 in^2 in effective surface area [**26**]. Figure 33 shows a variety of RMF blocks that have been soldered or brazed to a substrate to allow usage as a heat exchanger. The surface area of the foam depends on the PPI and density, typically ranging from 10 to 40 depending on application and 7 to 10%, respectively.

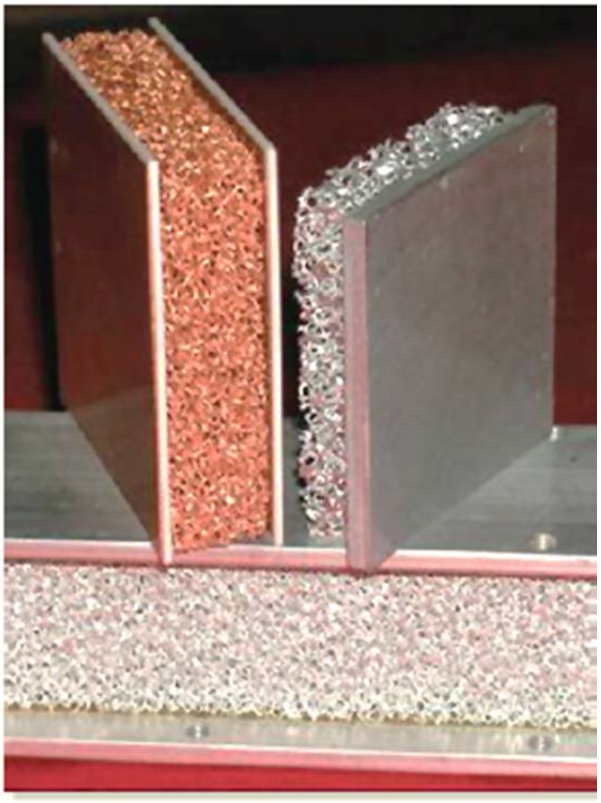

Figure 33: Block of RMF brazed or soldered to substrates [**26**]

Along with innovative systems using TE modules research has been conducted on the use of RMF's to improve the required heat exchanger's efficiencies. One of these applications is for Insulated Gate Bipolar Transistors (IGBT's). As new semiconductor technologies arise, the size of IGBT's are continually decreasing causing the heat load per unit area to increase. Ozmat [**26**] performed experiments looking at two different IGBT modules to show the advantage of a RMF based heat exchanger. The first IGBT is shown in Figure 34a, this is a 600 V/200 A unit that dissipates 300 W. It requires a 10.5 in^2 cold plate, which has a packaging efficiency of 15% and has an overall weight of 12 lbs. The second experiment, Figure 34b, tested a larger half bridge power module rated at 1200 V/400 A which dissipated 800 W, yet only required a base area of 3.5 in^2 resulting in a packaging efficiency of 45% while reducing the weight to only 1.2 lbs [**26**]. The first IGBT was tested with a typical plate-fin heat exchanger while the second one utilized a

RMF-based heat sink. This RMF-based heat sink allowed the use of a newer IGBT technology that not only reduced weight but improved performance.

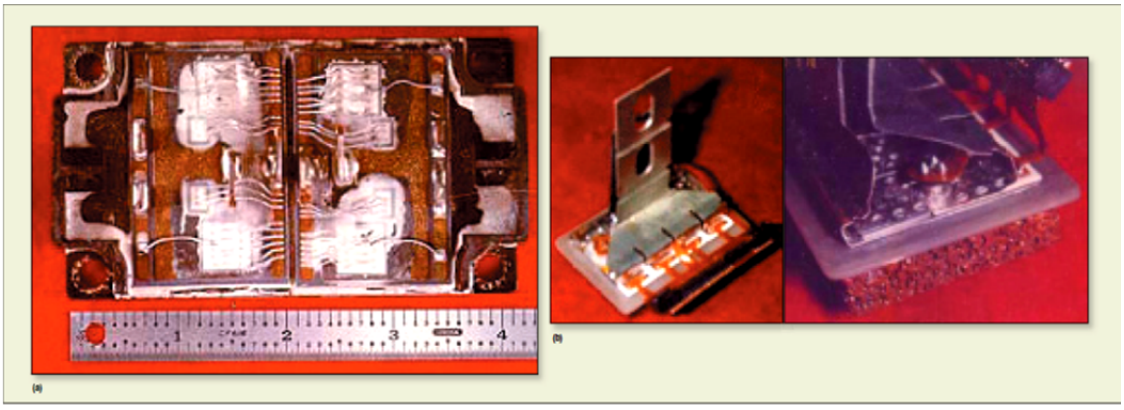

Figure 34: (a) IGBT with coldplate, (b) high power IGBT with RMF coldplate [**26**]

Along with performing experimentation on these two units, Ozmat et al [**25**] compared a standard cold plate to various RMF heat exchangers. The whole experiment was performed using the heat exchanger shown in Figure 35 with both 30 PPI aluminum and 30 PPI copper RMF's that have various relative densities.

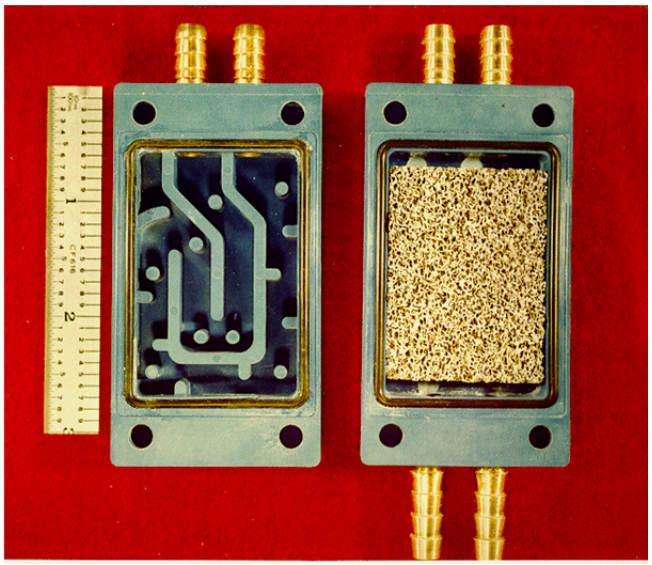

Figure 35: Baffled heat exchanger (left), Heat exchanger with RMF (right) [**25**]

The heat exchanger tested has a surface area of 20.64 cm^2 and 4 IGBT's capable of supplying a 100 W heat load were mounted to the face. Table 3 shows the experimental

results, and it can be seen that with the RMF`s a significant increase in power generation is possible. The copper RMF at 30 PPI and a density of 36% was able to provide a 105% increase over the baffled cavity and a 159% increase to a simple cold plate.

Table 3: RMF FEA and experimental results [**25**]

	Heat Sink	ΔT_{ja}, (^{0}C)	R_{ja} (^{0}C/W)	$P_{max.}$ @ ΔT_{ja} 60 °C
1-FEM	INTEGRAL-30 ppi Cu-36 %	60	0.043	1,400
2	BAFFLED CAVITY	75 °C @ 800W	0.095	640
3	EXTERNAL Cold Plate	95 °C @ 800W	0.120	505
4	INTEGRAL-30 ppi Al-10%	86 °C @ 800W	0.108	560
5	INTEGRAL-30 ppi Al-20%	69 °C @ 850W	0.080	740
6	INTEGRAL-30 ppi Al-36%	47 °C @ 850W	0.059	1020
7	INTEGRAL-30 ppi Cu-36 %	38 °C @ 800W	0.047	1310

1.3.2.2. Aerospace

The aerospace industry has been important in making RMF's available to larger markets. Use within this industry has been widespread from space exploration to satellites, and commercial airliners. ERG Aerospace [**28**] is one supplier that has seen success in the aerospace industry. They currently have products that are used for energy absorption, optics, CO_2 scrubbers, fuel cells, micrometeorite shields, heat exchangers and breather plugs. RMF's are also being explored for improvement to turbine engines. Wassim Azzi [**32**] looked at the feasibility of using metal foams to improve efficiencies and reduce fatigue in such components.

ERG Aerospace produces four different types of foam: aluminum, copper, carbon and silicon carbide. Each of these offers specific benefits in a variety of applications. They

began working with metal foams in 1967, but the work did not see commercial acceptance until the mid-1990's when the military research became declassified [**28**]. While the majority of such usage today is being centered around compact high efficient heat exchangers, metal foams have seen use within many facets of the aerospace industry.

CHAPTER 2 – SYSTEM COMPONENTS

2.1. INTRODUCTION

The most important aspect of electric vehicles is their energy storage systems (ESS). Owners are accustomed to vehicles operating trouble-free for 10+ years, and this standard must be maintained for EV's. In order to maintain a safe and reliable high performance battery for the lifespan of the vehicle, advanced thermal management systems must be employed. Lithium Ion (Li-Ion) batteries are becoming the chemistry of choice due to their power to weight ratios. Li-Ion batteries work best in an environment between 10-35°C [**33**]. Below this value the cell's power degrades, and under -20°C the cells are unable to provide sufficient current. At elevated temperatures, above 40°C, the cells age very quickly and thermal runaway becomes an increasing risk. The safety concern, reduced lifespan and reduction in performance has led manufactures to develop complex battery thermal management systems that incorporate a vehicle's A/C and heating system. The use of thermoelectrics simplifies this design as the heating and cooling can be performed by one dedicated device. This eliminates redundancies in existing designs, reduces weight for the various components and can improve the operating efficiency of the overall system. By maintaining a consistent battery temperature through adequate thermal management, the operation of a vehicle's ESS can more easily meet the required life expectancy without replacement over its lifetime. By educating customers on the benefits to EV's, reducing their range anxiety with larger battery packs, developing fast charge infrastructure and introducing comprehensive warranties, the market penetration of EV's should improve. The addition of an advanced battery thermal management system will also aid in improving the overall efficiencies and allow EV's to travel further before recharging.

Battery thermal management techniques are continuing to advance as their application within the automotive market grows. Current trends show a shift to the electrification of the automobile, along with this shift come new challenges. One of these challenges is adequate temperature control of the vehicle's ESS. Given this is the most expensive and important component in an EV, substantial resources are currently being utilized to develop innovative systems. Existing systems can be categorized into either passive or active thermal management solutions. Passive systems do not condition the cooling medium so they are simple and less expensive but they do not really provide adequate temperature control in extreme circumstances. Active systems condition the cooling medium through a variety of methods and provide an accurate means to control temperature; however this is done at both higher cost and complexity.

Thermal managements systems comprise a few components that perform the majority of the work. Typically the heat exchanger is the heart of the system with the remaining components functioning in conjunction to remove or add heat. In the case of a thermoelectric system there are two main components that operate together to accomplish this task. The vital component is the thermoelectric module, it is tasked with providing the necessary heating or cooling to the various components. The heat exchanger plays a dominant role as it ensures the TE module stays within its peak operating efficiency along with preventing any damage from overheating.

Reticulated Metal foams (RMF's) are currently being used by military, aerospace and the electronics industry as highly efficient heat exchange surfaces. RMF's offer the benefit of being lightweight, allow compact design while maintaining the ability to remove large

heat loads. This technology presents new opportunities for TE modules in providing more efficient operation and gaining acceptance as a commercial product.

2.2. THERMOELECTRICS

In order to understand the usefulness of TE coolers in a battery thermal management application their requirements are outlined to show strengths and weakness. Efficiencies are investigated to determine how current development is improving TE efficiency to levels approaching vapour compressor systems. Reliability is also a concern when applying a new method for thermal management. The system must be able to hold up to the rigors and demands of the automotive environment. Testing has been performed by numerous companies and researchers, results show that the TE modules are able to meet and exceed military specifications for: environmental, mechanical and thermal exposures. Product lifespan has also been validated in the laboratory and under real-world conditions with data showing that average industry modules are able to run steady state for 22.8 years, but only 236 days with large temperature variation [**34**]. The performance of the modules is also under scrutiny as history has shown that the majority of TE devices are unable to hold up to high cooling loads.

2.2.1. TE OPERATING CHARACTERISTICS

Methods to evaluate the performance of the TE modules have improved since their initial conception. The traditional method looks at the semiconductor material parameters as being temperature dependent or constant [**35**]. This method can be expanded and becomes more detailed by including the thermal and electrical contact resistances but is cumbersome [**36**]. A new method is being introduced that looks at the thermal properties under real conditions evaluated through experimentation. The important characteristics of

modern thermoelectric modules are: figure of merit (Z), heat capacity (Q) and coefficient of performance (COP). The formulation and calculation of these variables will be shown for three different evaluation methods.

2.2.1.1. Traditional method

The traditional method looks at the basic physics and thermodynamic principles to generate equations for operational characteristics. A circuit that describes the basic TE cooling is shown in Figure 36.

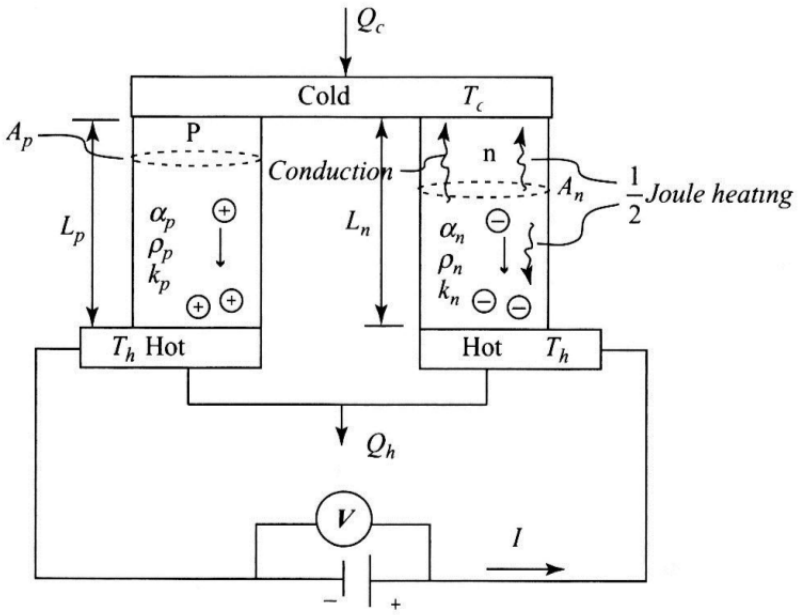

Figure 36: Electric circuit for thermoelectric cooling [**10**]

The first equation that describes the TE effect is the amount of heat absorbed by the system. The heat absorbed at the cold junction (Q_C) is given in Eq. (4) and based on three terms, Peltier cooling, half of the joule heating and thermal conduction. Here α is the Seebeck coefficient (V/K), I is the applied current (A), T_c is the cold-side temperature (°C), ρ_r is the specific resistivity (Ωm), k is the thermal conductivity (W/mK) and T_h is

the hot-side temperature of the thermoelement (°C). The heat rejected for the hot junction (Q_h) can be calculated from the same parameters as seen in Eq. 4 and 5.

$$Q_c = \alpha I T_c - 0.5 I^2 \rho_r - k(T_h - T_c) \tag{4}$$

$$Q_h = \alpha I T_h + 0.5 I^2 \rho_r - k(T_h - T_c) \tag{5}$$

The input electrical power consumed by the module is based on the 1st law of thermodynamics which states that the work exerted on an adiabatic system is based on the change in temperature. From this law, the power equation can be defined by the difference in the hot junction and cold junction, as shown by Eq. 5.

$$P = I^2 \rho_r + \alpha (T_h - T_c) I \tag{6}$$

Efficiency is an important term for the TE process, as it defines how well the system is able to convert the electrical input power to usable cooling. This efficiency is calculated by comparing the input power of the system to the heat absorbed, the COP is defined in Eq. 7.

$$COP = \frac{Q_c}{P} \tag{7}$$

While the COP is a good measure of a systems efficiency it does not provide a direct means to characterize performance of TE modules produced with various materials. This is done by calculating the figure of merit (Z) for each module as shown in Eq. 8. The Z value differs for all materials. If a material has a higher value it is considered superior because it can provide a higher level of cooling while consuming less power.

$$Z = \frac{\alpha^2}{\rho_r k} \tag{8}$$

The foregoing constitute the basic set of equations that most manufacturers base their TE module performance on. While these equations set a benchmark, they are unable to provide a practical method for real world applications. Presently, the parameters supplied by the TE module manufacturer are not application specific which leads to inaccurate performance estimates [**37**]. The main limitation to this method is that k, α, ρ_r are defined as constants when they are in fact dynamic and dependent on temperature [**38**]. To accurately characterize the operating conditions of the modules the equations need to be more dynamic and include temperature dependent variables.

2.2.1.2. Idealized method

After concluding that the traditional model produces errors, Min and Rowe [**36**] and Xuan [**39**] showed that the physical dimensions of the thermoelement within a TE module has a direct impact on its performance. As the size of each thermoelement changes, it affects the surface contact area and thus the thermal and contact resistance values. Xuan [**39**] derives the performance equations by investigating the effect of these thermal and contact resistances.

As with the traditional method the characterization of individual modules is done with the figure of merit. While the Z value provides a means to compare modules, it can be inaccurate. Xuan has expanded the calculation of the Z value to include the TE arm packing density (g), non-dimensional thermoelement length (l) and the non-dimensional term (t). The t term incorporates the thermal conductivity of the thermoelement materials (k), the thermal contact conductivity (k_c) and the reference length (L_{ref}). The

addition of these terms to the standard Z-value provides a more accurate result as the physical size, density and thermal contact is included.

$$Z_{eqv} = \frac{Z}{1 + 2gt/l} \tag{9}$$

Where;

$$t = \frac{k/L_{ref}}{k_c} \tag{10}$$

The inclusion of the thermal and contact resistances also alters the cooling capacity of the TE module. The cooling rate equation has been altered to include the thermal conductance of a TE couple (K), thermal contact conductance (K_c), the adjusted maximum temperature difference (ΔT_{max}), and temperature difference (ΔT).

$$Q_c = K_{eqv}(\Delta T_{max} - \Delta T) \tag{11}$$

Where;

$$\Delta T_{max} = \frac{1}{2} Z_{eqv} T_c^2 \tag{12}$$

$$K_{eqv} = K \frac{1}{1 + \frac{2K}{K_c} - \left(\frac{I\alpha}{K_c}\right)^2} \tag{13}$$

The optimal COP for the system follows a similar approach to the traditional method but with additional terms. Xuan uses multiple non-dimensional terms, W, θ and i to describe the system COP. These complex equations are used to provide an accurate COP value that includes the thermal and contact conductance found in TE modules.

$$COP = \frac{W - \theta}{(1 + W)(\theta - 1)} \tag{14}$$

Where;

$$W = \sqrt{1 + \frac{1}{2} Z_{eqv} T_c (1 + \theta)} \tag{15}$$

$$\theta = 1 + il(1 - git) - \frac{1}{2} i^2 \frac{l^2}{ZT_c} (1 + (\frac{2gt}{l}) - git) \tag{16}$$

$$i = \frac{I\alpha}{2kA/L_{ref}} \tag{17}$$

Through numerical calculations Xuan was able to conclude that the length of the thermoelement is proportional to the COP and inversely to the heat pumping capacity of the Peltier module [**36**]. As the thermoelement length increases so does the COP, while a shorter length is required for higher heat pumping capacity. This creates a contradiction and the TE module designer must compromise between a high COP and high Q_c value. While providing a more accurate method for calculations, it requires very specific knowledge on the material properties, thicknesses and design of each thermoelectric module. This is not practical for an engineer external to the TE manufacturer's organization who is looking to evaluate and apply the product, as most suppliers will not divulge their proprietary materials information.

2.2.1.3. Real method

The real method was first introduced by Ahiska and Ahiska [**38**] and is based on thermoemf values of the TE module. The real model provides engineers a way to analyze individual modules through basic experimentation and calculations. This method is more

effective than the previous two as it tests the actual module under working conditions and produces the following parameters: current (I), voltage (V), thermoemf (E) and surface temperatures (T_c or T_h). To determine the performance of the module V_{max}, I_{max} and E_{max} must be found.

To find these parameters the TE module must be tested while unloaded at a single T_h value. When the maximum ΔT occurs, the voltage, current and thermoemf are recorded, corresponding to V_{max}, I_{max} and E_{max} respectively for that specific T_h value.

For the real model equations derived by Ahiska [**38**], the figure of merit, heat absorption, power consumed, coefficient of performance and maximum thermoemf are summarized below.

$$Z = \frac{V_{max}E_{max}}{0.5(V_{max} - E_{max})^2\, T_h} \tag{18}$$

$$Q_c = V_{max}I - \frac{0.5I^2(V_{max} - E_{max})}{I_{max}} - \left[I + \frac{0.5(V_{max} - E_{max})I_{max}}{E_{max}}\right]E \tag{19}$$

$$P = \frac{I^2(V_{max} - E_{max})}{I_{max}} + EI \tag{20}$$

$$COP = \frac{Q_c}{P} \tag{21}$$

$$E_{max} = \frac{V_{max}\Delta T_{max}}{T_h} \tag{22}$$

$$\alpha = \frac{E}{\Delta T} \tag{23}$$

The benefit of the real method is that results are dependent on the T_h value and show the dynamic characteristics of the modules. It also gives engineers a process through which they can experiment to determine which module will best meet their specific application. Ahiska and Ahiska [**38**] compared calculations from the new and traditional methods to measured experimental values and determined the relative error. The real method produced a Q_c error of 5.1% and COP error of 3.2%, while the traditional method had errors of 15.9% and 19.9% respectively. This shows that the real method improves the accuracy of the calculations compared to traditional methods, and provides engineers a better tool to determine how effective various TE modules will be for their application. If a system will be operational over a temperature range the system should be tested throughout this range to ensure accuracy.

2.2.2. TE OPERATING REQUIREMENTS

Thermoelectrics have been predominately used in the electronics, military, aerospace and medical industries as outlined in chapter one. Their use in the automotive industry is mostly for passenger comfort or experimental power generation. The use of TE devices as part of a battery management system is a new concept with very limited research or development. In order for TE devices to compete with current active cooling systems using vapour compressors certain specifications must be met, i.e. cost, efficiency, reliability and performance must be comparable to existing thermal management systems. Numerous companies are developing innovative ways to improve existing TE device performance in other applications as explained previously. With some refinement these methods can be utilized within the automotive industry to provide an efficient means to heat/cool vehicle ESS's.

2.2.2.1. TE Efficiency

Current production TE modules lack the efficiencies required to compete with vapour compressor systems. Figure 37 compares efficiencies of the R134a vapour compressor cycle to: commercially available, laboratory grade and research grade TE modules. Presently, commercially available TE modules have a Z value between 0.7 and 1.0 while their COP is between 0.3 and 1.5 depending on the thermodynamic cycle [**40**]. To have comparable efficiencies to an R134a vapour compressor system, the Z value would have to increase in the range of 1.6-2.4. TE modules with these Z values have been developed by Research Triangle Institute (RTI) and Massachusetts Institute of Technology (MIT), and Z values greater than 4.0 can be found in the laboratory [**40**]. The efficiency of the TE module fluctuates depending on: T_c, T_h, Q_c, V, I and ΔT values. In automotive ESS applications, the heat load is always changing and requires the thermal management system to adapt and maintain the batteries within the recommended range. To maintain peak COP values, a complex controller is required to continually monitor the system and adjust the applied voltage to ensure maximum efficiency. While research is being conducted to generate modules with higher efficiencies, they are yet to be manufactured on a commercial scale, which leads to higher costs. Figure 37 indicates that BSST, a company specializing in thermodynamic research, has come up with a design approach that shows considerable improvements to the standard thermoelectric implementation.

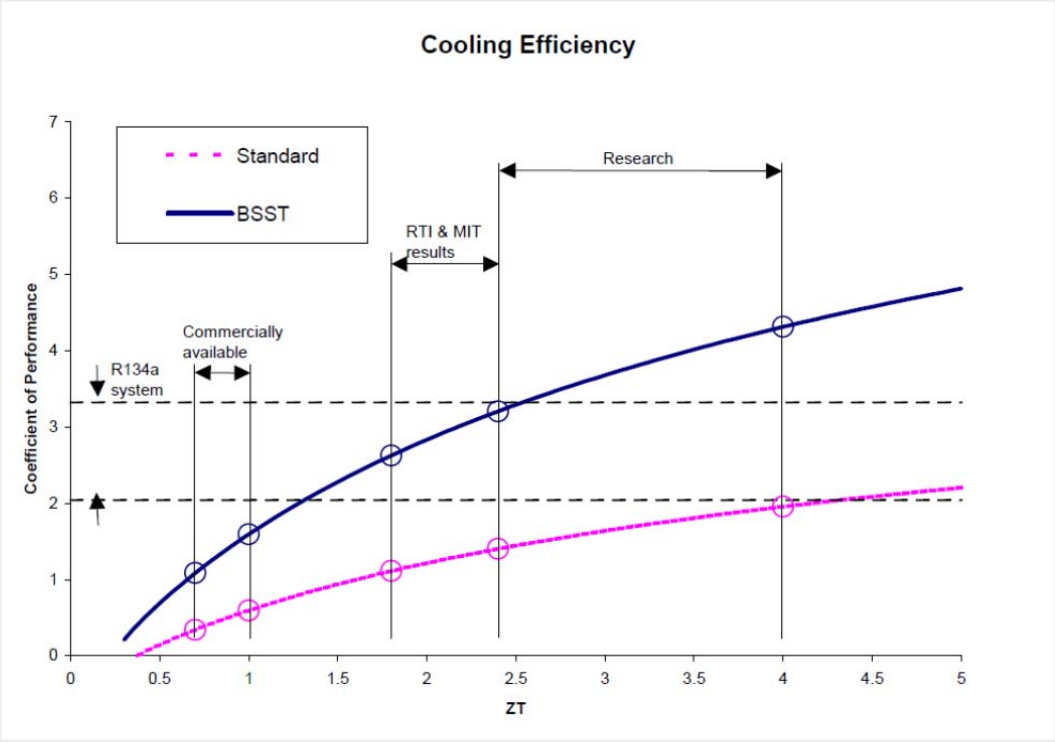

Figure 37: TE module cooling efficiency [33]

2.2.2.1.i BSST Cycle

The "BSST cycle" has been shown to double system efficiency compared to standard TE module implementation [**41**]. The first part of the cycle looks at how the heat flows from the TE module to the working fluid. In standard liquid cooled TE devices, as shown in Figure 38, the hot side and cold side temperatures are inconsistent for all modules. According to Bell [**41**] this prevents each module from running at its peak performance. To provide optimal conditions the thermal gradient across each module should be minimized, with each step being optimized for the specific temperature. The "BSST cycle" can be seen in Figure 39; it capitalizes on the working fluid being gradually heated/cooled as it passes through the device. This allows the engineer to design each TE element to run at its optimal ΔT thus improving efficiencies. The BSST design effectively constitutes a counter flow heat exchanger, thus each TE element needs to only pump heat

across the average temperature difference between inlet and outlet sides of the two fluid loops. This reduces max ΔT across each element and leads to a significantly higher COP, because COP is highly sensitive to ΔT.

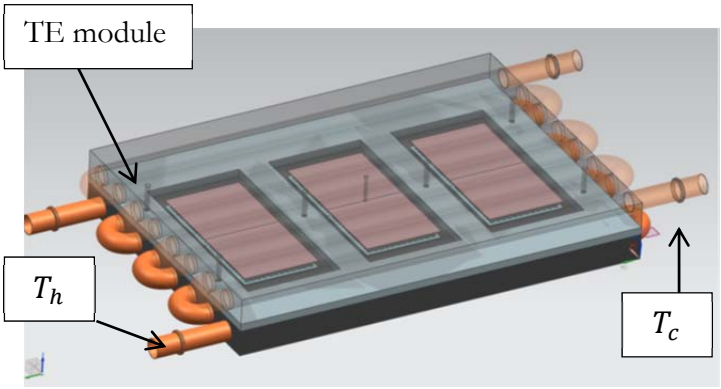

Figure 38: Standard TE liquid cooled device

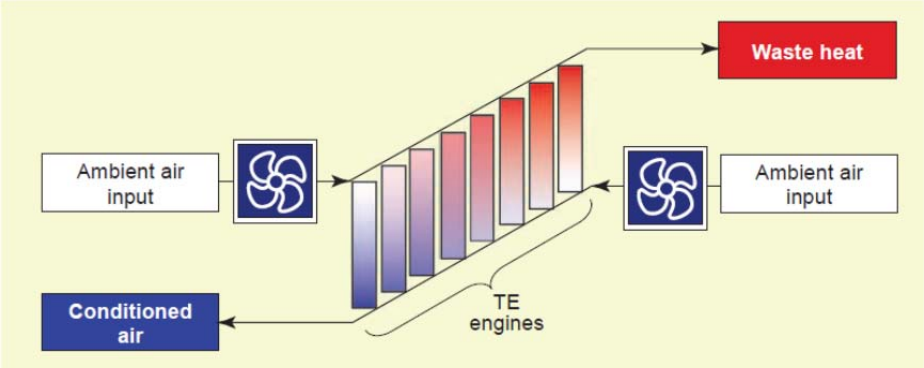

Figure 39: BSST thermal gradient cycle [32]

The BSST implementation also looks at parasitic and thermal losses typically found in TE modules. Modern TE modules, shown in Figure 3, use a substrate that electrically isolates the semiconductors while allowing thermal conductivity. As the TE devices are made smaller, the parasitic and thermal losses increase since the size of the electrical and thermal conductors becomes larger relative to the TE elements. Figure 40(a) shows the traditional design and the path length the electrons must flow is quite long with respect to the element height. Figure 40(b) shows the revised BSST stack design and that the path

for electron flow is significantly decreased as the heat exchanger is used as both an electrical conductor and thermal conductor, without a ceramic insulator.

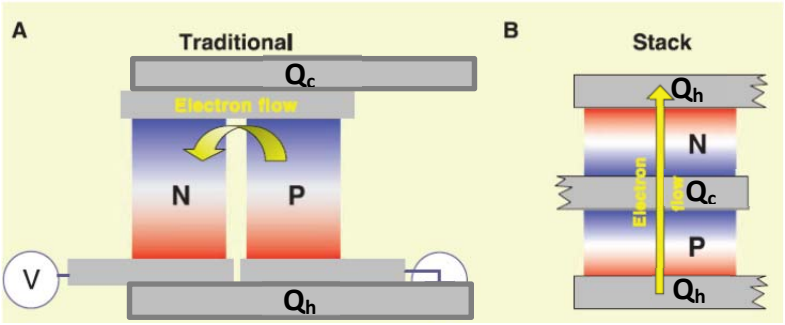

Figure 40: TE junction geometries. (a) Traditional, (b) BSST [**41**]

Experimental results show that running the TE module on the "BSST cycle" improves efficiencies 28-60% compared to the standard cycle [**42**]. With continued research and improvements to the Z values of TE modules, efficiencies are reaching levels previously only found in R134a vapour compressor systems. While the "BSST cycle" offers a method to optimize the efficiency of TE modules there are some inherent drawbacks in an automotive application. First, the system is optimized to work for a given temperature range; automotive applications can have a large dynamic temperature range which affect system efficiencies. Second is the use of a heat exchanger plate as both a thermal and electrical conductor, which can only work for (dry) air. A 50% glycol/50% water mixture is the standard automotive cooling fluid, and does not have dielectric properties, hence shorting such a heat exchanger. Thus the approach taken is not viable in conjunction with water/glycol-based based working fluids.

2.2.2.1.ii TE Module Efficiency

TE module efficiency varies between manufactures and even slightly between individual modules due to the manufacturing process. Some manufacturers provide

generic graphs depicting the module efficiency while others do not. TE Technologies Inc. provides these graphs with their module specifications and one can be seen in Figure 41. It must be appreciated that the input voltage and ΔT values have a profound impact on the system's efficiency. Each ΔT value has a specific voltage at which the peak efficiency occurs, this can be found using the series of calculations outlined in section 2.2.

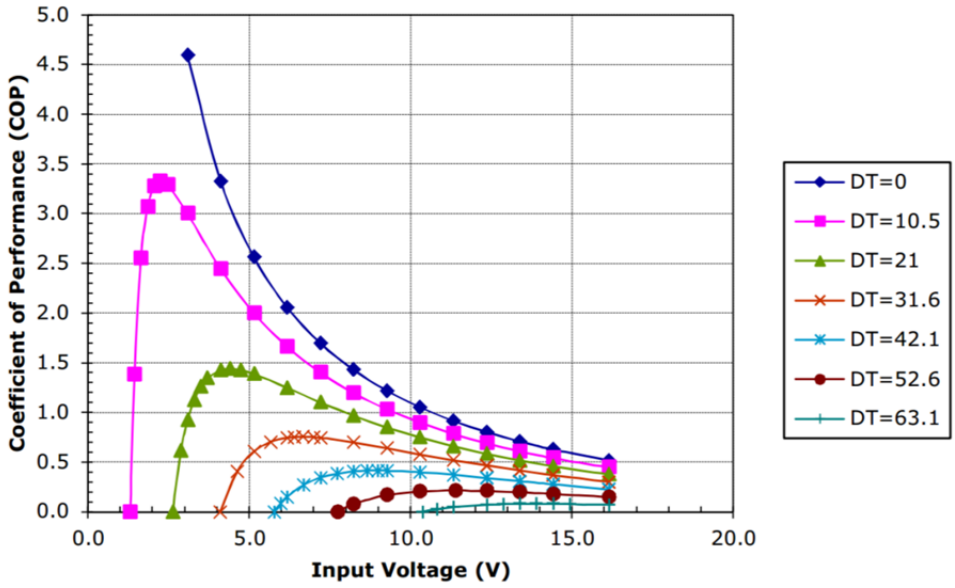

Figure 41: TE technology module HP-127-1.4-1.5-74 COP graph [**43**]

All TE modules follow a similar path with low efficiency at low voltages, quickly reaching peak efficiency then gradually decreasing. The point of maximum cooling power generally has a low COP due to Joule heating being predominant. A highly efficient system requires more modules running at lower voltage to ensure they remain at their peak COP. In automotive applications a balance must be struck between efficiency, cooling power, space requirements and cost.

2.2.2.2. TE Reliability

The reliability of the TE modules is paramount to ensure they will remain effective throughout the lifespan of the vehicle. Durability of TE components should be a minimum of 10 years/150,000 miles without excessive degradation [**44**]. These standards are similar to that which the vapour compressor systems must meet. Since TE devices are solid state components which have the advantage of no moving parts, the likelihood of a system malfunction diminishes. Although it is an improvement, TE modules still risk failure. The main failure modes are: mechanical cracking or splintering of the elements, solid state diffusion, solder joint failure, whisker growth, mishandling, inadequate heat sinking and moisture accumulation [**45**]. To ensure the TE module does not fail, a variety of reliability tests are performed.

The automobile has a unique environment where it can see large temperature, humidity and moisture fluctuations. Chapter 1 reviews the collection of industries that have been using TE modules since the 1950s. The two that stand out for durability testing are aerospace and military. As previously mentioned, TEG's used in NASA spacecraft have stayed operational for 35 years and remain in service. The military has also used TE devices extensively for the past 50 years and the devices routinely meet their shock and vibration requirements [**34**]. Proper mounting is required to meet such specifications. This must be considered when the modules are mounted in compression with the use of thermal grease to aid in heat transfer. The recommended module compression is 200 psi, but some tests have shown they can withstand up to 1000 psi [**34**]. To improve the heat transfer between TE modules and heat exchangers, some designers solder the TE module directly to a solid heat exchanger. This has been found to promote thermal stresses which

causes premature module failure and is not recommended by manufacturers of large modules [**46**].

Table 4: Environmental / Mechanical test conditions [**34**]

High Temperature Operation and Storage	150°C for 30,000+ hours
Low Temperature Operation and Storage	-40°C for 1000+ hours
Thermal Shock	(a) 100°C (15 sec) -100°C (15 sec), 10 cycles
	(b) 150°C (5 min)/-65°C (5 min)/ 150°C, 10 cycles
	(c) MIL-STD-202, Method 107
Mechanical Shock	(a) 100G, 200G 26msec; 500G, 1000G @1 sec 3-axis, three shocks each axis
	(b) MIL-STD-202, Method 213, Test Condition I
Vibration	(a) 10/55/10 Hz, 1 minute cycle, 9.1G, 3-axis, 2-hours each axis
	(b) MIL-STD-202, Method 204A, Test Condition B, 15G Peak

2.2.2.2.i Mechanical testing

The mechanical testing of TE modules looks at the mechanical shock and vibration that the systems can withstand. Ferrotec, a TE module manufacturer, subjects their modules to numerous tests as outlined in Table 4. All of these tests exceed conditions that are found in typical automotive environments. Research has also been conducted at the AT&T Bell Laboratory on the reliability for thermoelectric coolers in laser modules. To test the mechanical shock resistance of the system they soldered 10 modules to individual copper fixtures, then subjected them to: 500G, 1000G, 1500G, and 2000G's of force through a 0.5 ms sine pulse [**45**]. The results from these tests are shown in Table 5 with

failures occurring at the 1000G, 1500G and 2000G tests. These tests are more destructive than ones shown in Table 4 but act as a measure to show the forces TE modules are capable of handling.

Table 5: Mechanical shock data results [**45**]

Shock Level [g]	Direction of Shock pulse	Number failed
500	+X	0
500	+Z	0
500	-Z	0
1000	+X	2
1000	+Z	0
1000	-Z	0
1500	+X	0
1500	+Z	1
1500	-Z	0
2000	+X	0
2000	+Z	1
2000	-Z	0

Vibration testing was also performed along with the shock testing by applying 20G's from 20 to 2000 Hz under sinusoidal vibration. For this test, Corser [**45**] found that the device containing 30 TE modules and the 10 individual TE modules passed without failure. This testing was more demanding than that outlined by Ferrotec in Table 4, reinforcing that with proper design vibration is not an issue for TE modules.

2.2.2.2.ii Thermal Cycle testing

The industry standard for steady state cooling Mean Time Between Failures (MTBFs) is in excess of 200,000 hours [**34**], this is equivalent to running the system 24 hrs/day for 22.8 years. Automotive applications do not run steady state and will see gradual thermal cycling along with on/off power cycling, both of which reduce the MTBF value of the module. Figure 42 shows the results of a thermal cycling reliability test. The system was

cycled from 30°C to 100°C then back to 30°C. One cycle took 5 minutes and the results are graphed by the number of weeks the test system ran. When 50% of the modules failed the test was stopped, all modules achieved 25,000 cycles without failure and the MTBF of the group was found to be 68,000 cycles equivalent to 5666.7 hours or 236 days of continuous operation [**34**].

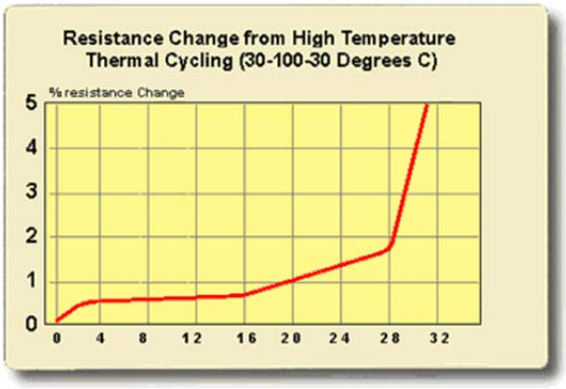

Figure 42: Thermal cycling reliability testing of TE module [**34**]

In an automotive application, TE modules could see an on/off power cycle every time the vehicle is driven, and possibly even parked while the vehicle is attempting to maintain battery temperature under extreme conditions. In another module performance test, Ferrotec applied full rated current for 7.5 seconds, then turned the system off for 7.5 seconds resulting in one cycle. The test was run for 25,000 hours or 6 million cycles. For this test condition the module's calculated MTBF was found to be 125,000 hours equivalent to 14.26 years [**34**].

Another major concern for TE module reliability is the risk of moisture corroding the electrical contacts. When the module is cooling below the dew point, moisture can form within the module if not properly sealed. Automotive applications are particularly at risk as the modules will be subjected to moist environments. To prevent moisture from being

an issue most manufacturers offer an epoxy potting that is added around the perimeter of the module. This prevents water ingress from damaging any of the critical electrical components. Along with potting, it is recommended to try to reduce the risk of moisture by providing a sealed assembly. The one downside is sealing forms a thermal bridge across the TE element's hot and cold sides, thus reducing module efficiency.

Considerable testing has been performed on TE devices to ensure they are able to withstand the harsh environments in military and aerospace applications. TE usage within a battery thermal management system will probably not see the temperature extremes, mechanical stresses or thermal stresses that some modules have been tested at. Automotive applications tend to be less demanding than military or aerospace ones, leading to the conclusion that the reliability of TE modules is likely sufficient for their application within automotive systems if well developed. If a standardized test procedure was designed for automotive applications, Table 4 would be a good start as the conditions fall within automotive operating specifications.

2.2.2.3. TE Performance

The performance of TE devices depends on the heat exchangers they are in contact with. Given the complexity of modern battery systems and move towards Li-Ion batteries, the management system should be an active one with either air or liquid as the working fluid. Due to the inefficiencies with present TE devices, the logical choice is to use a liquid system as a higher heat transfer can be achieved at lower ΔT. The performance required depends on the given application and heat flow requirements. Modern EV and HEV's have different battery chemistries and pack sizes. This leads to a large variation in heating/cooling requirements. The performance of the TE module is also important as

manufacturers offer a variety of products with different: voltage, amperage, cooling capacity, size, and max temperature differences. To choose an optimum module for the application, an analysis must first be performed, then the module(s) can be chosen according to the system requirements.

2.3. METAL FOAM HEAT EXCHANGER

The unique architecture of a metal foam heat exchanger also means that limited documented information exists on the subject in thermal design textbooks and research papers. While convective transport in a porous media has been studied for over 150 years this was mostly done with porosities (ε) varying from 0.3 to 0.6 [**47**]. The type of RMF analyzed has an $\varepsilon > 0.9$ in its native form and its complex structure limits the use of standard heat exchanger theory. To truly understand the benefit possible, a specific analysis is requisite. The literature review was limited to papers written on the subject. Standard non-dimensional heat transfer terms: Reynolds number, Nusselt number and Colburn factor were employed to compare performance of the various configurations tested. Dimensional terms: heat transfer coefficient (h), pressure drop (ΔP) and pumping power (W) are employed to define performance analytically.

2.3.1. HEAT EXCHANGER THEORY

2.3.1.1. Non Dimensional terms

Non-dimensional terms are important in capturing results. They are an accurate way to depict an optimal design when analyzing a variety of configurations. For standard flow in pipes the Reynolds number signifies the presence of laminar or turbulent flow. At small numbers, Re<2300, the viscous forces overcome the inertial forces keeping the fluid in

laminar streamlines. At larger numbers, Re>4000 these viscous forces are unable to overcome the inertial ones causing turbulent flow. The range between 2300-4000 is the transitional period where both laminar and turbulent flows are present. Eq. (24) shows the standard equation for flow without a porous medium. Reynolds number in this equation gets modified based on Darcy's law with the square root of the permeability replacing the hydraulic diameter, Eq. (25) [**48**].

$$Re = \frac{\rho V_m D_{hyd}}{\mu} \tag{24}$$

$$Re_k = \frac{\rho v_d \sqrt{K_p}}{\mu} \tag{25}$$

The Nusselt number is another non-dimensional term used extensively as a representation of the heat transfer coefficient. It represents the ratio of convective conductance to pure molecular thermal conductance over the hydraulic diameter. In laminar flow it is dependent on the thermal boundary condition and flow passage geometry. While in turbulent flow the Dittus-Boelter or Gnielinski correlations with the hydraulic diameter should be used in place of a boundary condition [**49**]. Laboratory testing showed that all flow would fall within the laminar regime, thus a standard Nusselt calculation could be completed, Eq. (27).

$$Nu = \frac{q}{A_{con}\Delta T}\frac{D_{hyd}}{k_c} \tag{26}$$

$$Nu = \frac{q}{A_{con}(T_{pl} - T_{c,inlet})}\frac{D_{hyd}}{k_c} \tag{27}$$

The Colburn factor is a heat transfer term that describes performance by comparing the resulting heat transfer coefficient to the flow velocity required to achieve that value [**50**], normalized for the fluid's energy transport properties, Eq. (28). When plotted against the Reynolds number, it indicates which system is superior for a given flow rate. To accurately compute the Colburn factor, density, specific heat, kinematic viscosity and fluid thermal diffusivity were interpolated for each test point. (50% Ethylene Glycol/50% water mix).

$$j = \frac{h}{\rho C_p v_d}\left(\frac{v}{\alpha_f}\right)^{2/3} \tag{28}$$

2.3.1.2. Dimensional Terms

While non-dimensional terms are one method to compare the thermal performance of different heat exchanger designs, in comparing these parameters we must also look at a number of dimensional terms that help correlate the results. These additional terms can be grouped into thermal properties, power requirements and flow characteristics. The thermal properties define key parameters such as the heat transfer coefficient and thermal resistance. The pumping power requirements are defined by $Q \cdot \Delta P$, the theoretical wattage consumed by the system fluid pumping. Flow characteristics constitute the dimensional parameters which define the differences between the various physical configurations.

The heat transfer coefficient denotes the rate of convective heat transfer that is possible between a solid and fluid interface, a larger h-value indicates a more efficient heat transfer system. This value is dependent on the heat input, temperature differential and contact area between the fluid and solid Eq. (29). The temperature differential used is the plate surface temperature minus the log mean temperature difference (LMTD) of the HX

fluid between inlet and outlet. This is used to determine the average temperature within the HX and given in Eq. (30).

$$h = \frac{Q_c}{A_{con} \cdot (T_{pl} - T_{LMTD})} \tag{29}$$

$$T_{LMTD} = \frac{(T_{c,outlet} - T_{c,inlet})}{LN\left(\frac{T_{c,outlet}}{T_{c,inlet}}\right)} \tag{30}$$

The thermal resistance defines the heat exchanger's performance. A lower thermal resistance indicates a more efficient design.

$$R_{th} = \frac{T_{pl} - T_{c,inlet}}{\dot{m}C_p(T_{c,outlet} - T_{c,inlet})} \tag{31}$$

How effective a heat exchanger is under working conditions also depends on the energy consumed to operate the system. This is accomplished by analyzing the pumping power requirements for a given heat transfer rate. Ultimately a balance must be struck between pumping losses and heat exchanger performance.

$$W = \Delta P \cdot Q \tag{32}$$

The flow characteristics play an important role in determining an effective heat exchanger design. These parameters allow the engineer to configure the heat exchanger to maximize the heat transfer characteristics for the specific application. Three different configurations were tested to determine the more effective design. All three are based on a rectangular duct, Figure 43, with variations in width, height and effective flow length. These dimensions are used to calculate the hydraulic diameter Eq. (33) and cross-sectional area Eq. (34) for all flow paths, and are outlined in Table 6.

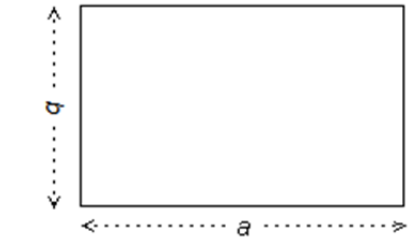

Figure 43: Flow Geometry

Table 6: Flow path Characteristics

	Test 1			Test 2
	U-channel	**S-channel**	**Cross-flow**	**Cross-flow**
Width- a (mm)	31.0	19.0	63.5	63.5
Height-b (mm)	10.0	10.0	6.0	6.0
Cross sectional area (m^2)	3.10E-04	1.91E-04	3.81E-04	3.81E-04
Hydraulic Diameter (mm)	15.1	13.1	11.0	11.0
Contact Area (m^2)	4.01E-03	3.71E-03	4.03E-03	4.84E-03
Effective Length (mm)	128.9	194.7	63.5	63.5

Hydraulic Diameter [**49**]

$$D_{hyd} = \frac{2ab}{a+b} \tag{33}$$

Cross sectional area [**49**]

$$A_{cs} = a * b \tag{34}$$

The effective length of each flow path is measured using the average length of the passage. This is dependent on geometry and outlined in Figure 44, these lengths were measured using the length calculation tool within Unigraphics (NX) 7.5.

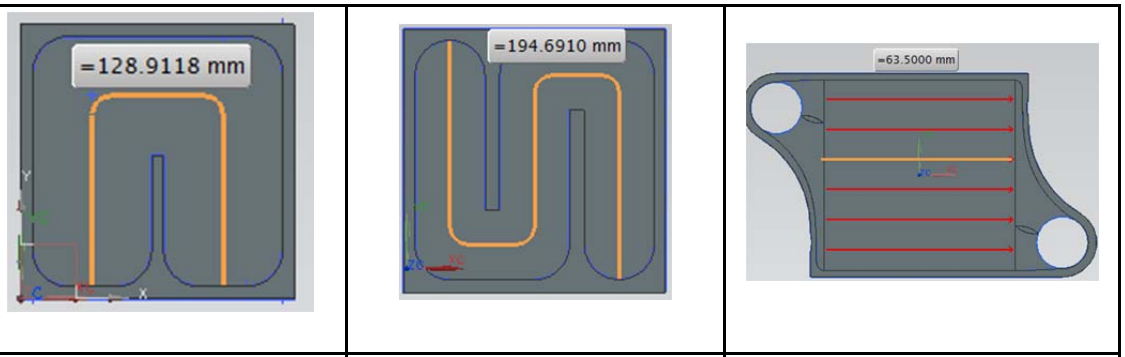

(a) (b) (c)

Figure 44: Effective Flow Length - a) U-path, b) S-path, c) Cross Flow

The surface contact area between the foam and the HX (A_{con}) was similarly measured in NX and is shown in Figure 45 for test #1. Test #2 removes the TE module so the heater is in direct contact with the HX. To fit the larger heater between the inlet and outlet it had to be rotated 12.5°, the resulting contact patch is shown in Figure 46.

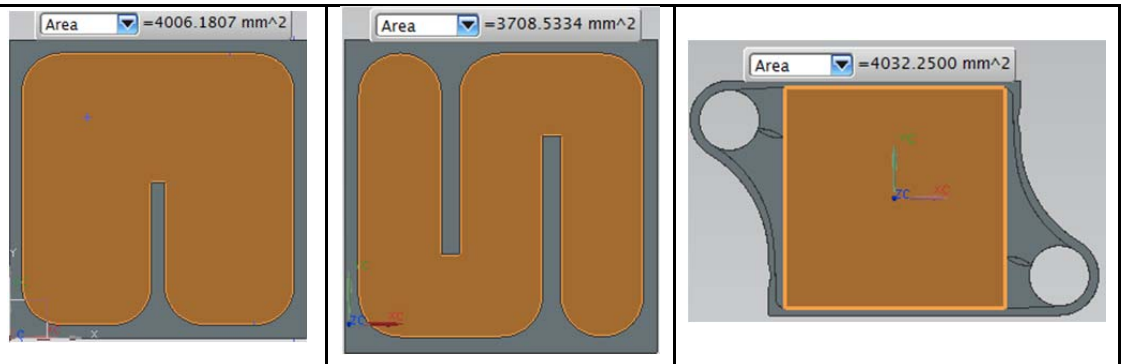

(a) (b) (c)

Figure 45: Contact Area - a) U-path, b) S-path, c) Cross Flow

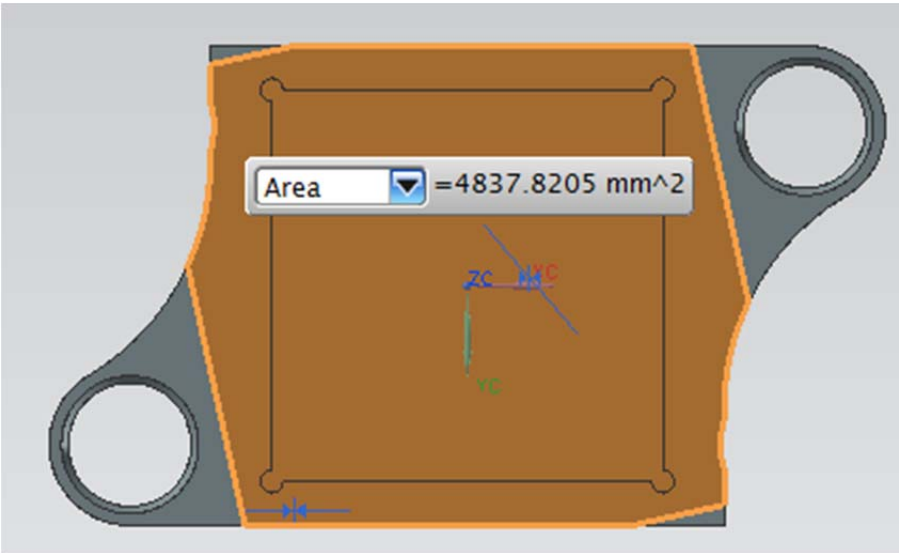

Figure 46: Test 2 contact area

2.3.2. FOAM OPERATING CHARACTERISTICS

Metal foam was chosen as a medium to enhance heat transfer within the heat exchanger due to its ability to increase the effective surface area greatly with a minimal increase in mass. To optimize the use of a RMF, operating characteristics need to be understood. The effects of compression, material, porosity, density and permeability on both the thermal and operational parameters are outlined below. A compromise must be established between the pressure losses in the system and an effective heat transfer coefficient.

2.3.2.1. Permeability

Porous medium was first studied by Henry Darcy in 1856, he was able to show that the pressure drop through a porous material was a function of the flow velocity and permeability [**50**]. Through a continuation of the theories he developed, the pressure drop within porous media is governed by Eq. (35), where: L_f is the effective length, μ is the

dynamic viscosity of the fluid, ρ is the density of the fluid, K_p is the permeability factor and C is the form coefficient.

$$\frac{\Delta P}{L_f} = \frac{\mu}{K_p} v_d + \rho C {v_d}^2 \tag{35}$$

Through experimentation it has been found that Darcy's law only holds true when low flow velocities are present, typically when the Reynolds number falls within the 80>Re_k>5 regime [**48**]. The Darcian velocity is calculated using the volumetric flow rate and passage cross sectional area, Eq. (36). Boomsma and Poulikakos [**48**], showed through experimentation that this theory still holds true when testing RMF's up to 5.00 LPM with a corresponding Re_k of 26.5.

$$v_d = \frac{Q}{A_{cs}} \tag{36}$$

There are multiple methods to calculate the permeability of a porous medium, the most accurate method is to directly measure the pressure drop of the medium through a range of flow rates [**51**]. This method takes into account the specific permeability and form drag coefficients for the system, which are difficult to determine analytically. The quadratic relationship is shown in Eq. (35). A least-squares quadratic curve is fit when the pressure drop per length is graphed against the flow rates, with the coefficients extracted being the permeability and form coefficients. This must be done for each test configuration as the brazing/soldering environment can have an impact on the permeability of each heat exchanger.

2.3.2.2. Physical Characteristics

The benefit to using RMF's is their ability to be configured to meet a specific performance requirement. This can be accomplished by changing the foam's density, porosity or cell size. The most cost effective way to do so is by compressing the foam in a combination of the 3 orthogonal dimensions [**25**]. Compressing the foam reduces the cell size improving its thermal performance [**52**]. A consequence of compressing the foam is the subsequent increase in pressure drop across the medium. Boomsma et al [**50**] performed an experiment by compressing two different porosity foams (92% and 95%) and documenting the heat transfer performance. Table 7 outlines the variance in foam structure that was tested.

Table 7: Foam compression experimental set-up [**50**]

Foam Porosity	Compression	Name	Expected porosity [%]	Measured porosity [%]
Panel A -Compressed foam physical data				
5%	2x	95-02	90.0	88.2
	4x	95-04	80.0	80.5
	6x	95-06	70.0	68.9
	8x	95-08	60.0	60.8
8%	2x	92-02	84.0	87.4
	3x	92-03	76.0	82.5
	6x	92-06	52.0	66.9
Panel B - uncompressed foam physical data				
Foam	Pore diameter[mm]		Specific surface area [m2/m3]	Measured porosity [%]
40PPI	2.3	2700	92.8	92.8

Their experimental results, Figure 47, show how the pressure drop is dependent on the compression and porosity of the foam. Higher compression led to lower foam porosity, which created a greater pressure drop in the system as expected. The pressure drop is velocity dependent, thus at a higher velocity the compression ratio has a more significant impact.

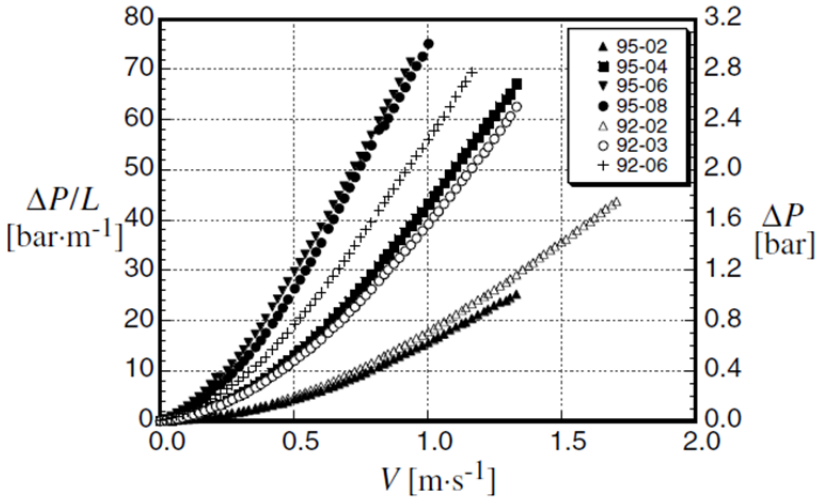

Figure 47: Pressure drop vs. Velocity [**50**]

To measure the heat transfer performance of the compressed foam, the pumping power needed is plotted against the thermal resistance. This allows a measurement that accounts for thermal performance vs. energy input. Figure 48 shows the results of Boomsma's experiment, the configuration that had the best relative performance was 92-06. This is measured as the point closest to the origin, which can be back calculated to a heat transfer coefficient of ~80,000 W/m^{2}K at 1.71 LPM and 45 KPa pressure drop.

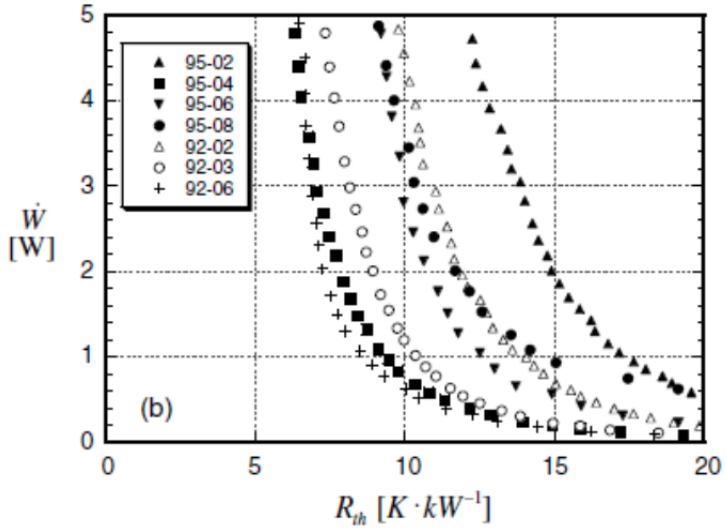

Figure 48: Pumping power vs. Thermal Resistance [**50**]

To maximize the effectiveness of the RMF Ozmat [**26**] describes the necessity of brazing. This completes the thermal bridge between the foam and the exterior of the heat exchanger. The material on the brazing interface is difficult to control, so it is common for excess brazing material to be present within the foam pores after the fact. This excess fills in some of the cells and creates resistance in the flow path. Table 8 shows a comparison of the various compressed foams and the influence on the permeability due to brazing material. All but the highest compressed conditions show an increase in the flow resistance. The cases with high compression (95-08 and 92-06) see a decrease in flow resistance due to the warpage and distortion attributed to the brazing, which formed flow bypasses [**50**].

Table 8: Brazed vs. Unbrazed foam [**50**]

Flow Resistance Comparison				
Foam	Unbrazed		Brazed	
	K_p (10^{-10} m^2)	C (m^{-1})	K_p (10^{-10} m^2)	C (m^{-1})
95-02	44.4	1168	34.4	1276
95-04	19.7	2707	6.87	2957
95-06	5.25	4728	3.16	5066
95-08	2.46	8701	2.52	4731
92-02	36.7	1142	30.8	1472
92-03	23	1785	8.26	2820
92-06	3.88	5518	3.95	3399

Metal foams come in a variety of materials, the two most common are aluminum and copper. Each material has its own benefits when being utilized in a heat exchanger; these are outlined in Table 9. Zhao et al. [**52**] found that the base foam material is influential in determining the relationship of density and cell size to the heat transfer characteristics. Through experimentation they were able to show that due to the high thermal

conductivity of copper, increasing the density of the copper sample had a negligible impact on heat transfer whereas a reduction in cell size can improve heat transfer.

Table 9: Material Specifications, Metal foams

Parameter	Aluminum-6061-T6	Copper-C10100
Cost-Raw material ($US/kg) [**53**]	4.40-6.20	4.00-7.00
Weight (g/cm^3) [**53**]	2.7	8.89
Bulk Thermal Conductivity (W/mK) [**4**] [**54**]	5.8	10.1
Ease of Brazing	Difficult	Moderate

CHAPTER 3 – TE MODULE TESTING

3.1. INTRODUCTION

The performance of a TE module can be estimated by the T_h, T_c, ΔT_{max} and Q_c defined by the manufacturer. These parameters are best established through experimentation. As discussed in Chapter 2, there can be errors between the manufacturer's specifications and the actual values under operational conditions. To evaluate the performance at operating conditions, experiments were performed to cross-validate manufacturer specifications. Two different experiments are used in the validation process, the first is Seebeck coefficient testing which measures the T_h, T_c and ΔT_{max} values, the second utilizes a heat load and measures the Q_c value for the given TE module.

Both of these methods were employed to determine any deviation from the manufacturers' specifications and help understand what performance can be expected from the various supplier's TE modules. A comparison was completed to determine which module showed the highest performance. This module type was then used to perform tests on the heat exchanger designs.

3.2. SEEBECK TESTING

Seebeck coefficient testing was used to evaluate the temperature specifications of the TE module. The hot side of the TE module was placed on a heat exchanger allowing it to dissipate the heat generated while minimizing damage to the TE module, whereas the cold side is open to atmosphere allowing it to reach its minimum temperature ($T_{c_{max}}$). The

manufacturer's maximum voltage specification was applied and the system was allowed to stabilize at ΔT_{max} Once ΔT_{max} has been achieved a Tyco EV200 contactor cuts power to the TE module. All the values are measured the instant prior to the contactor opening, except for E_{max}which is measured 1 millisecond afterwards as this is the point with the highest Seebeck voltage. This was done for each TE module examined; the results were compared to their datasheets in order to calculate deviation from specifications.

The second portion of the recording is the measured Seebeck voltage that each module generates when the voltage source is removed. This is carried out to determine the corresponding Seebeck voltage for a given ΔT. Each module will exhibit slight differences and the test allows one to determine the operating characteristics of the individual modules.

3.2.1. TEST BENCH

Figure 49 shows the test bench configuration, with the individual components outlined in Table 10. The Seebeck test bench was used to evaluate the individual TE modules. The system uses a coolant block along with the TE module to measure its maximum operational characteristics. Traditionally, this evaluation is performed in a vacuum by a manufacturer to achieve the highest possible value. However, the modules will operate in a real world environment so the experiment is performed in ambient air to replicate the actual working condition. To prevent the convective air currents from skewing the test data, a 10 mm thick blanket of Cyrogel Z, also referred to as aerogel, was wrapped around the entire set-up. Figure 50b shows the bench set up with and without aerogel insulation.

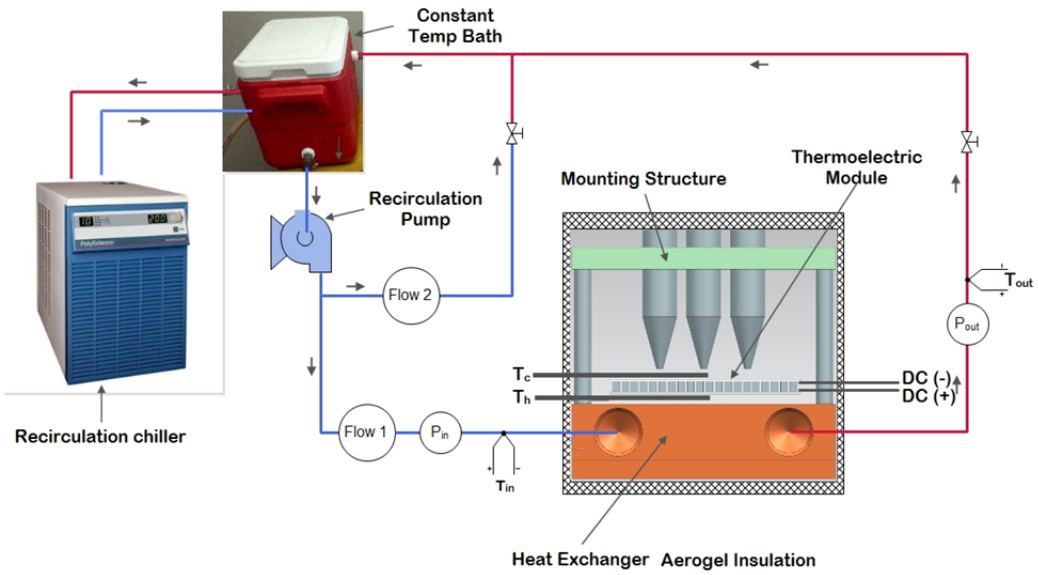

Figure 49: Seebeck test bench layout

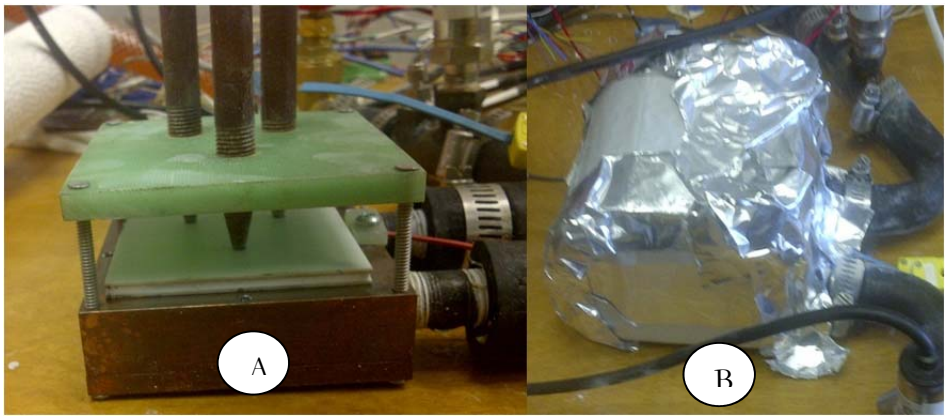

Figure 50: Seebeck Testing A) w/o aerogel, B) with aerogel

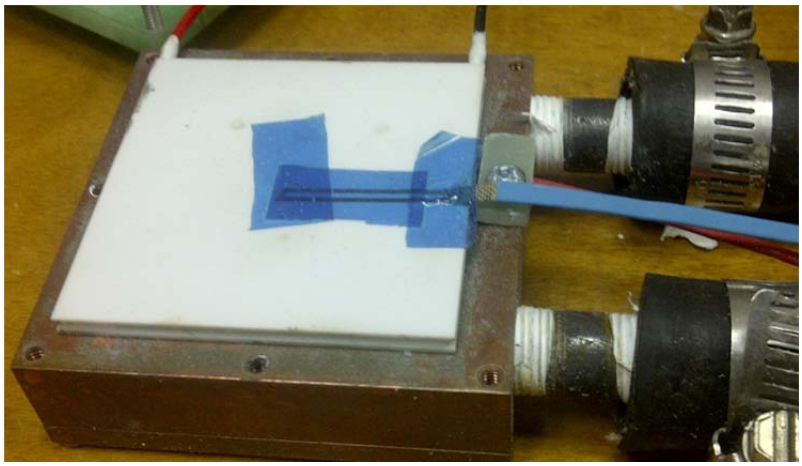

Figure 51: Thermocouple placement with non-conductive tape

To ensure consistent contact with the heat exchange surface, a mounting structure was created to provide uniform pressure along the top face. This structure constituted fibreglass rods machined to a point then threaded into a fibreglass reinforced plastic (FRP) block. It allowed pressure to be applied while minimizing the heat load on the TE module. Each fluid supply line was located after the pump, and had a flow meter and a gate valve to both regulate and measure flow, allowing for consistent test conditions. Temperature and pressure probes were placed in the fluid lines to measure ΔT values across the heat exchanger. Surface temperature was measured using an insulated K-type foil thermocouple placed in the middle of the TE module, as shown in Figure 51. This was done to minimize end effects and provide an accurate reading of the TE face. Amperage was measured using an Allegro Hall Effect sensor. All analog voltages and temperature were read using an IPETRONIKS data acquisition (DAQ) system recording at 10 Hz. Pulses from the flow meter employed a secondary DAQ system, a LabJack U6. It also provided the 5 V source for the hall effect sensor. Two different power supplies were used due to the variance in required voltages. The fluid pumps and IPETRONIKS DAQ ran off a switching power supply which was regulated at 13.0 V. The TE modules ran off dual Sorenson power supplies connected in series. This was required to meet the voltage demands of certain TE modules. The output was further smoothed by the use of a 2200 uF capacitor. Electrical diagrams for this configuration can be found in Appendix A.

Table 10: Test component specifications

Item	MFG	Model #	Range	Accuracy
Chiller	PolyScience	6000	-10° to 70°C	± 0.1°C
Heat exchanger	Custom Thermoelectric	WBA-3.0-0.85-CU-01	Up to 1200 W	N/A
Pump	Bosch	PAD 12 V	0-15LPM	N/A
Water thermocouple	Omega	KMQSS-062G-6	-270° to 1372°C	0.75%
K-type foil Thermocouples	Omega	88309	-270° to 1372°C	0.75%
Pressure Sensors	SSI Technologies	P51	± 5.0 psi	<±1.0%
Flow meter	Omega	FPR301	0.07 to 5.0 GPM	1.0% FS
Heater elements	Omega	CSH-103220/120 V	0 – 220 W	5-10%
TE Power Supply	Sorenson	DCS 20-50E	0-20 V @ 0-50 A	±1.0%
Heater Power Supply	Lambda	ZUP60-14	0-60 V @ 0-14 A	±0.2% + 2 digits
12V Power Supply	Caswell	SPC-9250	0-15V @0-25A	±1.0% + 2 digits
Thermocouple DAQ	IPETRONIKS	M-THERMO K16	-60° to 1300°C	±0.0035% of Temp range
Voltage DAQ	IPETRONIKS	M-SENS 8	± 100 V	±0.13% unipolar voltage range
Hall Effect Sensor	Allegro	ACS576	± 50 A	0.8%
Flow meter DAQ	LabJack	U6	0 to 12 bil DAC	Pulse Counter

In certain applications, water is considered the ideal candidate to use as a liquid cooling medium because of its exceptional heat transfer characteristics. The final use of the TE powered heat exchanger is to be within an automotive thermal management system, susceptible to large fluctuations in temperature. The cooling medium must be able to withstand temperature variations from -40°C to 60°C so a 50% water/50% ethylene glycol is habitually used to prevent the liquid from freezing. One limitation to this mixture is the reduction in heat capacity, as the temperature lowers so does the heat capacity, but not on a linear scale. To accurately determine the heat capacity of the 50% water/50%

ethylene glycol, data was taken from [**55**]. To ensure accuracy a Hanna Instruments refractometer (model 96831) was used to verify the glycol concentration.

3.2.2. TEST SCHEDULE

TE modules were chosen from a variety of companies based on their ability to provide a high cooling power. The list of chosen TE modules and their specifications are shown in Table 11. All modules utilize an aluminum oxide substrate, except for Kyrotherm which employed a metalized aluminum nitride surface improving thermal conductivity and allowing the surface to be soldered.

Table 11: Manufacturer specifications

Company	Kyrotherm		Custom TE	Thermonamic		TE Tech		Crystal
Part #	TB-199-2.0-0.8HT		TC 26311 -5M31-17CW	TEC1-24127T200		HP-127 -1.4-1.5-74		D-288-14-06
T_h	27	50	27	27	50	27	50	25
V_{max} (V)	24.6	26.5	31.5	29.5	33.2	16.7	18.5	36.7
I_{max} (A)	20.6	21.8	17.0	28	28	6.3	6.3	14.9
ΔT_{max} (°C)	69	78	67	68	76	74	84	68
E_{max} *(V)	5.658	6.399	7.035	6.687	7.812	4.119	4.811	8.319
Q_{max} (W)	352	352	331	508.4	559.1	65	71.3	340.3
P* (W)	506.76	577.7	535.5	826	929.6	105.21	116.55	546.83
Z* (1/K)	0.00259	0.0026	0.0025	0.00253	0.00249	0.0029	0.00294	0.00253
α (V/K)	0.082	0.082	0.105	0.0983	0.1028	0.0557	0.0573	0.1223

* Values were calculated from equations (17), (19) and (21)

The test schedule was generated by analyzing each module's datasheet, some companies only provided data at T_h of 27°C while others had both 27°C and 50°C. To determine how the modules performed under various loads, each one was tested throughout its operating range. The test points for each module are outlined in Table 12. Despite not having manufacturer's data at 50°C for the Custom TE and Crystal modules, the test points were estimated to judge their performance compared to that of the other modules. To carry out each test the power supply was set to the V_{max} and the system was

allowed to stabilize, the contactor was then switched off providing an instantaneous voltage cut-off point. All measured values were taken at this cut-off point so it had to be consistent throughout all the tests. Similar tests were also carried out at lower voltage settings for each module

Table 12: Seebeck Test Schedule

Iteration	Temp. (°C)	Voltage (V)				
		TE Tech	Custom TE	Kyrotherm	Crystal	Thermonamic
Test 1	27	8.00	12.00	12.00	15.00	10.00
Test 2	27	10.00	16.00	15.00	20.00	15.00
Test 3	27	12.00	20.00	18.00	25.00	20.00
Test 4	27	14.00	25.00	20.00	30.00	25.00
Test 5	27	16.00	30.00	22.00	35.00	29.50
Test 6	27	16.70	31.50	24.30	36.70	-
Test 7	50	8.00	12.00	12.00	15.00	10.00
Test 8	50	10.00	16.00	15.00	20.00	15.00
Test 9	50	12.00	20.00	18.00	25.00	20.00
Test 10	50	14.00	25.00	20.00	30.00	25.00
Test 11	50	16.00	30.00	22.00	35.00	30.00
Test 12	50	18.50	32.00	24.00	38.00	33.20
Test 13	50	-	-	26.20	-	-

3.2.3. RESULTS

The effective Z value is a comparative measure of a TE module's efficiency as the latter tends to exhibit a lower number in practice. The aim is to quantify this number to better estimate a COP values that can be realized in practice. Through experimentation the module performance could be compared to the manufacturer's data shown in Table 11 (full results in Appendix B). The parameter that most impacts the TE module's performance is ΔT_{max} as it is used to estimate a variety of other parameters including the E_{max} value (Seebeck voltage). When ΔT_{max} is low, it reflects directly on the performance

of that module. To meet the defined performance the ΔT_{max} must be close to the published value.

3.2.3.1. Test Procedures and Equations

Through experimentation seven variables are measured or calculated; V_{max} , I_{max}, ΔT_{max}, E_{max}, P, Z and α. The V_{max} , I_{max} and ΔT_{max} values are measurements taken directly from the test bench immediately prior to the open circuit, while E_{max} is measured from the test bench 1ms after the open circuit. The power (P) is calculated using Eq. 20, figure of merit (Z) is calculated using Eq. 18 and Seebeck coefficient (α) is calculated using Eq. 23. Sample calculations are shown below for the TE Tech module with data taken from Appendix B, line 1.

$$Z = \frac{V_{max}E_{max}}{0.5(V_{max} - E_{max})^2\ T_h} = \frac{18.5 \cdot 2.44}{0.5(18.5 - 2.44)^2\ \cdot 49.89} = 0.00124\ \frac{1}{K}$$

$$P = \frac{I^2(V_{max} - E_{max})}{I_{max}} + EI = \frac{7.48^2(18.5 - 2.44)}{7.48} + 2.44 \cdot 7.48 = 136.50\ W$$

$$\alpha_{max} = \frac{E_{max}}{\Delta T} = \frac{2.44}{59.79} = 0.0408\frac{V}{K}$$

3.2.3.2. Experimental Error and Uncertainty Analysis

Experiments inherently contain measurement error, these can be categorized as either fixed or random. Fixed errors are known as bias and are made up from the tolerance of the components themselves. Random errors are defined as precision and come from the test data [**56**]. To understand the full scope of error that is present during testing an

uncertainty analysis was performed. This uncertainty looks at both the bias and precision errors to estimate the variation that can be expected in the results. To reduce experimental uncertainty the following measures were applied during testing.

- Component calibration was done prior to each test.
  - Value measured for 2 minutes @ 1 Hz
  - Result averaged and applied to calculation in DAQ
  - 6 significant digits used
- Voltage measurements taken at source
- Length and gauge of wire tailored to current level
  - 16ga wire for TE and heater
  - 20ga wire for sensors

The IPETRONIKS DAQ provides high fidelity measurement accuracy with complete galvanic isolation and cold junction compensation. The losses along the wire are considered negligible due to the measures taken, DAQ used and steady room temperature working environment.

Two types of uncertainty are found in the experimental data, single sample and multiple inputs. Single samples are measures such as voltage. The bias is found by taking the root sum of squares of the measuring instruments, outlined in Table 13, while the precision is the standard deviation of the data set measured, which was calculated through a statistical analysis. Multiple input uncertainty is used when a calculation takes places involving more than one measured value. In this case the bias is calculated with Eq. 37 and precision with Eq. 38. Single and multiple uncertainties are calculated using the same formula, Eq. 39.

$$B_R = \left\{ \sum_{i=1}^{N} \left(\frac{\partial R}{\partial X_i} B_i \right)^2 \right\}^{1/2} \tag{37}$$

$$S_R = \left\{ \sum_{i=1}^{N} \left(\frac{\partial R}{\partial X_i} S_i \right)^2 \right\}^{1/2} \tag{38}$$

$$(U_R)_{0.95} = \{ (B_R)^2 + (tS_R)^2 \}^{1/2} \tag{39}$$

A sample calculation is illustrated below using the Seebeck voltage data from the Crystal TE module found in Table 16. For this measurement the uncertainty value is 7.07E-04 V/K which is 0.39% of the calculated value.

$$R = \alpha_{max} = \frac{E_{max}}{\Delta T}$$

$$\frac{\partial R}{\partial \Delta T} = \frac{-E_{max}}{\Delta T^2} = -0.00348$$

$$\frac{\partial R}{\partial E_{max}} = \frac{1}{\Delta T} = 0.0206$$

$$B_R = \left\{ \sum_{i=1}^{N} \left(\frac{\partial R}{\partial X_i} B_i \right)^2 \right\}^{1/2} = \left\{ \left(\frac{-E_{max}}{\Delta T^2} B_{\Delta T} \right)^2 + \left(\frac{1}{\Delta T} B_{E_{max}} \right)^2 \right\}^{1/2} = 5.36\text{E-}05$$

$$S_R = \left\{ \sum_{i=1}^{N} \left(\frac{\partial R}{\partial X_i} S_i \right)^2 \right\}^{1/2} = \left\{ \left(\frac{-E_{max}}{\Delta T^2} S_{\Delta T} \right)^2 + \left(\frac{1}{\Delta T} S_{E_{max}} \right)^2 \right\}^{1/2} = 7.05\text{E-}04$$

$$U_{\alpha_{max}} = \{ (B_R)^2 + (tS_R)^2 \}^{1/2} = \{ (1.89\text{E-}04)^2 + (7.05\text{E-}04)^2 \}^{1/2} = 7.07\text{E-}04 \text{ V/K}$$

$$\%\ of\ measured\ value = \frac{U_{\alpha_{max}}}{\alpha_{max}} * 100 = \frac{7.07\text{E-}04}{0.1804} * 100 = 0.39\%$$

Table 13: Instrument error and uncertainties-Crystal TE

	Component Accuracy				Calculations			
	DAQ	Sorenson Power Supply	Hall effect sensor	Thermocouple	Bias	Precision	Uncertainty	% of measured value
V_{max} (V)	0.13%	1%	-	-	0.0101	0.0114	0.0152	0.04%
I_{max} (A)	0.13%	1%	0.80%	-	0.0129	0.125	0.126	0.89%
ΔT_{max} (°C)	0.00%	-	-	0.75% x 2	0.015	0.191	0.191	0.39%
E_{max} (V)	0.13%	-	-	-	0.01	0.0114	0.0152	0.14%
P (W)	-	-	-	-	0.494	8.91	8.92	1.71%
Z (1/K)	-	-	-	-	8.58E-06	6.22E-05	6.28E-05	2.70%
α_{max} (V/K)	-	-	-	-	5.36E-05	7.05E-04	7.07E-04	0.39%

Such uncertainty analysis gives an indication of the level of accuracy inherent with the test bench. Individual measurements have a high degree of accuracy with less than 1% uncertainty. Some calculated values are based on multiple measurements causing the uncertainty to propagate and increase up to 2.70%. Performing an uncertainty analysis is imperative to validate the accuracy of the test apparatus. These results confirm that the test bench and components used fall within an acceptable range. When the experimental results varied by more than 10% from manufacturer specifications the result is highlighted in the following tables. This was done in an effort to show results falling significantly outside the uncertainty inherent to experimental set-up, and most likely attributable to the product under test.

3.2.3.3. TE Tech

The first module examined was from TE Tech, although this module had the lowest cooling capacity it was still used to validate the test equipment. This module was extensively used for testing prior to the Seebeck specific experiments, thus the data was benchmarked with previous results to calibrate/debug the experimental set-up. The results listed in Table 14 show that when the voltage was set to the manufacturers

specification the corresponding values did not correlate. Experimental results for these modules vary from 0.01% to 57.87% of the computed values based on manufacturer specification.

$$\%\, Difference\ = \frac{Experimental\ Value - Spec\ Value}{|Spec\ Value|} \cdot 100 = \frac{7.48 - 6.30}{6.30} \cdot 100 = 18.77\%$$

Despite high deviation, these values were verified by repeated data runs and are considered to be accurate.

Table 14: Seebeck Testing - TE Tech

TE Tech Module						
	Mfg. specifications		Experimental Results		% Difference	
	(T_h =27°C)	(T_h =50°C)	(T_h =27°C)	(T_h =50°C)	(T_h =27°C)	(T_h =50°C)
V_{max} (V)	16.7	18.5	16.01	18.50	-4.11	-0.01
I_{max} (A)	6.3	6.3	7.18	7.48	13.93	18.77
ΔT_{max} (°C)	74	84	58.92	64.50	-20.39	-23.21
E_{max} (V)	4.119	4.811	2.38	2.70	-42.25	-43.89
P (W)	105.21	116.55	114.94	136.50	9.25	17.12
Z (1/K)	0.00290	0.00294	0.00137	0.00124	-52.86	-57.87
α_{max} (V/K)	0.0557	0.0573	0.0426	0.0439	-23.50	-23.30

3.2.3.4. Custom TE

The Custom TE module was the first of the high powered modules to be tested. The results show that there was a 13.44% deviation in ΔT_{max} from the data sheet. The main concern with this module was its inability to reach the I_{max} and ΔT_{max} specifications. These two variables indicate that the module is underpowered compared to published data. The module was then tested at a T_h of 50°C to see if its performance would improve. Without manufacturer data it was not known how much to increase the supply voltage in compensation for the higher overall operating temperature, so it was simply

maintained. With a higher Seebeck voltage to overcome, the effective voltage on the module is reduced which caused a lower current flow.

Table 15: Seebeck Testing - Custom TE

Custom TE Module				
	Mfg. specifications	Experimental Results		% Difference
	(T_h =25°C)	(T_h =27°C)	(T_h =50°C)	(T_h =27°C)
V_{max} (V)	31.5	32.108	32.035	1.93
I_{max} (A)	17	15.246	13.492	-10.32
ΔT_{max} (°C)	67	57.995	64.565	-13.44
E_{max} (V)	7.035	6.914	8.589	-1.72
P (W)	535.5	489.507	427.222	-8.59
Z (1/K)	0.00247	0.00258	0.00310	4.58
α_{max} (V/K)	0.1050	0.1279	0.1333	21.83

3.2.3.5. Crystal

The Crystal TE had the second largest ΔT_{max} deviation of all the modules tested, at 28.63%. This error drives the remaining discrepancies and provides insight that this module is an underperformer. When tested at a T_h of 50°C the module showed a reduction in current as seen with the Custom TE module.

Table 16: Seebeck Testing - Crystal

Crystal Module				
	Mfg. specifications	Experimental Results		% Difference
	(T_h =25°C)	(T_h =27°C)	(T_h =50°C)	(T_h =27°C)
V_{max} (V)	36.7	36.703	38.061	0.01
I_{max} (A)	14.9	14.197	12.900	-4.72
ΔT_{max} (°C)	68	48.529	54.551	-28.63
E_{max} (V)	8.319	8.205	9.526	-1.37
P (W)	546.83	514.682	477.935	-5.88
Z (1/K)	0.00253	0.00249	0.00275	-1.54
α_{max} (V/K)	0.1223	0.1804	0.1879	47.49

3.2.3.6. Thermonamic

The thermonamic module had the poorest performance across the board. This module was the largest measuring 62 mm x 62 mm and had the highest power rating at

559.1 W. The biggest concern with these modules was their inability to meet the published ΔT_{max} levels, at a discrepancy of ~30%. The cooling block used during these tests was rated to 1200 W so that was not the limiting factor. Upon inspection after the test, it was found that the leads had unsoldered themselves from the TE module. To verify if it was an issue with an individual module 2 others were tested at a reduced voltage. In both cases the modules had unsoldered leads upon final inspection. With a failure rate of 100% after three modules in a controlled environment, it was determined that these modules were nowhere near able to withstand the rigors that would be required in the desired application. No further experimentation was performed due to these poor results.

Table 17: Seebeck Testing - Thermonamic

Thermonamic Module						
	Mfg. specifications		Experimental Results		% Difference	
	(T_h =27°C)	(T_h =50°C)	(T_h =27°C)	(T_h =50°C)	(T_h =27°C)	(T_h =50°C)
V_{max} (V)	29.5	33.2	29.500	33.257	0.00	0.17
I_{max} (A)	28	28	20.682	20.605	-26.14	-26.41
ΔT_{max} (°C)	68	76	47.481	52.544	-30.17	-30.86
E_{max} (V)	6.687	7.812	6.090	7.018	-8.93	-10.17
P (W)	826	929.6	610.115	673.201	-26.14	-27.58
Z (1/K)	0.00253	0.00249	0.00218	0.00210	-13.59	-15.79
α_{max} (V/K)	0.0983	0.1028	0.1200	0.1377	22.02	34.00

3.2.3.7. Kyrotherm

The final module tested provided the best results. This was the only module able to meet and exceed the expected ΔT_{max} values. In testing, voltage was increased in steps and performance was evaluated at lower current levels. During testing the module met the performance metrics prior to being run at the 24.3 V_{max} indicated by the manufacturer. To prevent damage to the module, no further testing was performed at the T_h of 27°C.

Table 18: Seebeck Testing - Kyrotherm

Kryotherm Module						
	Mfg. Specifications		Experimental Results		% Difference	
	(T_h =27°C)	(T_h =50°C)	(T_h =27°C)	(T_h =50°C)	(T_h =27°C)	(T_h =50°C)
V_{max} (V)	24.3	26.2	22.60	26.48	-6.99	1.07
I_{max} (A)	22.9	24.3	20.83	22.47	-9.04	-7.53
ΔT_{max} (°C)	68	77	69.17	78.56	1.73	2.02
E_{max} (V)	5.508	6.246	5.36	6.27	-2.74	0.35
P (W)	556.47	636.66	469.22	595.01	-15.68	-6.54
Z (1/K)	0.00253	0.00254	0.00271	0.00252	7.36	-1.10
α_{max} (V/K)	0.0810	0.0811	0.0843	0.0853	4.02	5.19

3.2.3.8. Overall

The modules were tested to varying degrees, the Kyrotherm module performed very close to the published values, while the Thermonamic modules repeatedly failed under the stated operating conditions, with others falling somewhere in between. A comparison of all modules examined is summarized in Table 19. The Kyrotherm module clearly outperformed all the competitor products tested when comparing to their manufacturers' specifications. The remaining modules are ranked based on their performance during the experiments. The Custom TE module had a ΔT that was only 15% off target, but the balance of testing showed significant deviation from published values. The evaluation continued utilizing a heater to determine the cooling capacity of different modules.

Table 19: Seebeck Testing - Deviation from Mfg., Specifications

Deviation from MFG Specs								
	Kryotherm Module		TE Tech Module		Crystal	Custom TE	Thermonamic	
	T_h=27° C	T_h=50° C	T_h=27° C	T_h=50° C	T_h=25° C	T_h=27° C	T_h=27° C	T_h=50° C
V_{max} (V)	-6.99	1.07	-4.11	-0.01	0.01	1.93	0.00	0.17
I_{max} (A)	-9.04	-7.53	13.93	18.77	-4.72	-10.32	-26.14	-26.41
ΔT_{max} (°C)	1.73	2.02	-20.39	-23.21	-28.63	-13.44	-30.17	-30.86
E_{max} (V)	-2.74	0.35	-42.25	-43.89	-1.37	-1.72	-8.93	-10.17
P (W)	-15.68	-6.54	9.25	17.12	-5.88	-8.59	-26.14	-27.58
Z (1/K)	7.36	-1.10	-52.86	-57.87	-1.54	4.58	-13.59	-15.79
α (V/K)	4.02	5.19	-23.50	-23.30	47.49	21.83	22.02	34.00
Ranking	1		3		4	2	5	

In carrying out the foregoing tests the Seebeck voltage was graphed as the system cooled from the ΔT_{max} to room temperature. The graphs generated for each TE module can be reviewed in Appendix B, with an exemplar graph depicted in Figure 52. These graphs show the Seebeck voltage (E) as a function of ΔT which gives the Seebeck coefficient (α). The graphs for each of the modules follow a similar pattern. In time sequence the graph is generated right to left; after the power source is removed there is a decreasing slope curve before the data follows a linear path towards zero. The initial trace was an unexpected result, but can in part be attributed to the location of the thermocouple on the TE module's surface. A cross section of the TE module's temperature profile is shown in Figure 53. The graph on the right side of Figure 53 shows the internal temperature distribution within a TE module under load. As the outer ceramic surface and copper conductor cool, their temperature profiles reverse to eventually assume a gradient in the same sense as the P and N thermo active materials within. It is postulated that within this period the temperature at the semi-conductor/copper interface decreases rapidly as it equilibrates, faster than at the surface,

thus the Seebeck 'E' is falling more rapidly than the recorded surface temperature. This effect could give rise to the initial non-linearity during the cooling response.

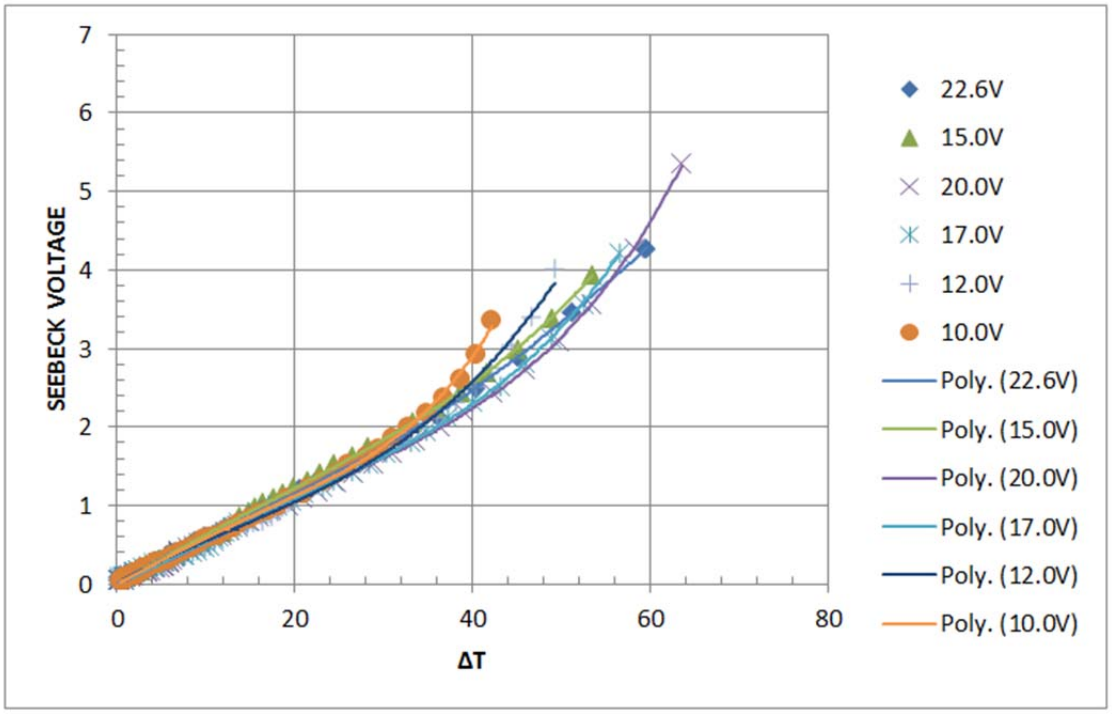

Figure 52: Kyrotherm Seebeck Voltage @ T_h=27

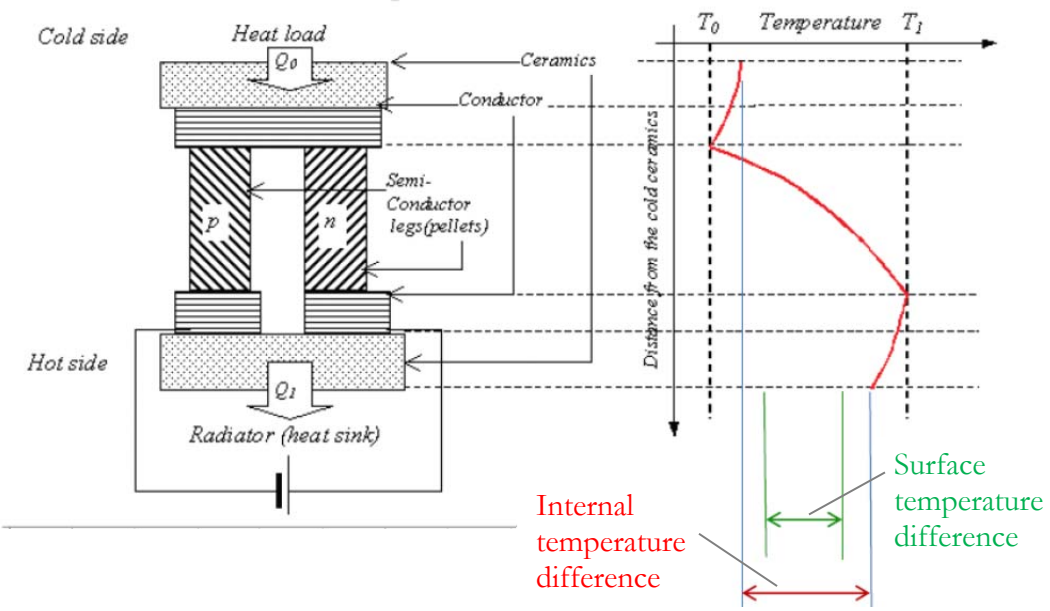

Figure 53: TE system limitations

The only TE module that did not follow this characteristic response was the Thermonamic unit after it was run at higher voltage. It shows signs of experiencing failure, with resistive heating apparently superimposing itself upon the characteristic response resulting in $E < 0$ over a portion of the range.

Although these tests provide insight on the characteristics of the individual modules when "unloaded", they do not guarantee performance under typical operations. For such evaluation a known heat source must be used.

3.3. TE MODULE VALIDATION

With the initial benchmarking of the various TE modules completed, it was imperative to test each one to determine the real cooling capacity. While the Seebeck test provided an operating characteristics of the individual module it was unable to measure the amount of cooling each is capable of. The next test ran each module under various steady loads to determine the level of cooling it was able to provide for a given current. This was accomplished by sandwiching a heater between two TE modules and running the assembly at different heat loads. Given a defined heat input, the cooling can be measured using the temperature difference across the TE's heat exchanger and fluid flow rate. The same bench setup utilized for the Seebeck testing was modified to include a heater. The results from this test were then compared to the Seebeck values found with the previous experiments to confirm module performance.

3.3.1. TEST BENCH

While the major components for the test bench remain the same, a second fluid loop was added to measure and run the additional TE module. This second loop contains the

same apparatus as the first with, flow meters, pressure sensors, thermocouples and an independent pump. To accurately measure the heat input, a heater plate was made from a solid block of copper machined to hold six 120 V/220 W heating elements, for a total output of 1320 W. These were evenly placed within the block to give uniform temperature throughout and powered with a Lambda ZUP60-14 power supply. Current and voltage sensors were placed directly on the leads and recorded with the IPETRONIKS DAQ system. A system diagram is shown in Figure 54 and the electrical schematic can be found in Appendix A. The structure to mount the heat exchanger was modified to hold both heat exchangers, the TE modules and the heater as an assembly. FRP plates were again utilized to ensure minimal thermal and no electrical bridge exists between modules. Four aluminum rods are used to provide the clamping force necessary to ensure adequate surface contact (Figure 55). The assembly was then surrounded by a 10 mm thick blanket of Cryogel Z to prevent data from being skewed by ambient conditions.

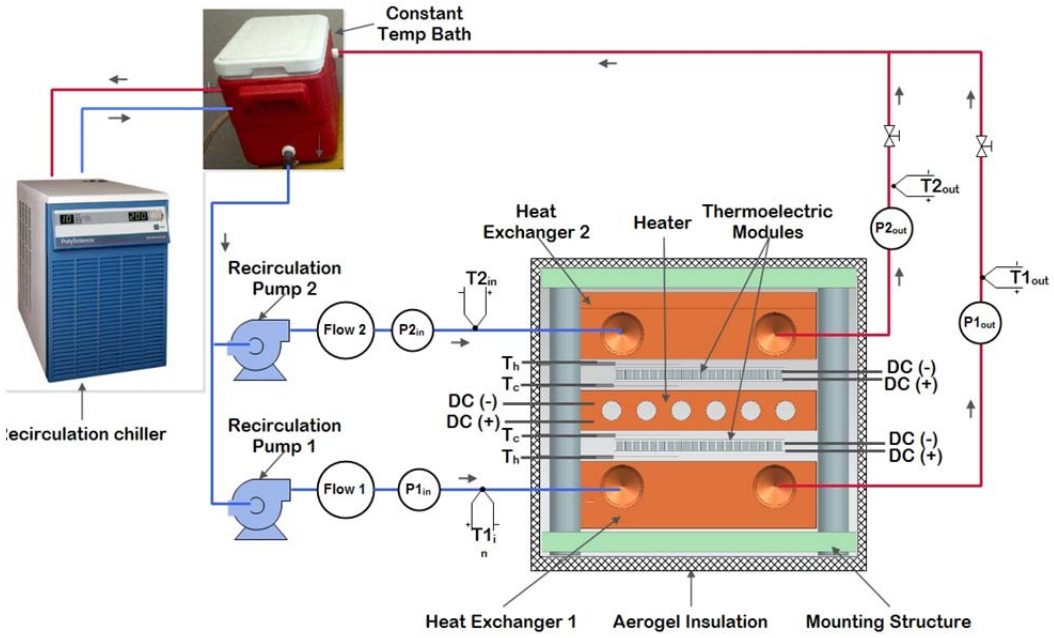

Figure 54: Heater testing system diagram

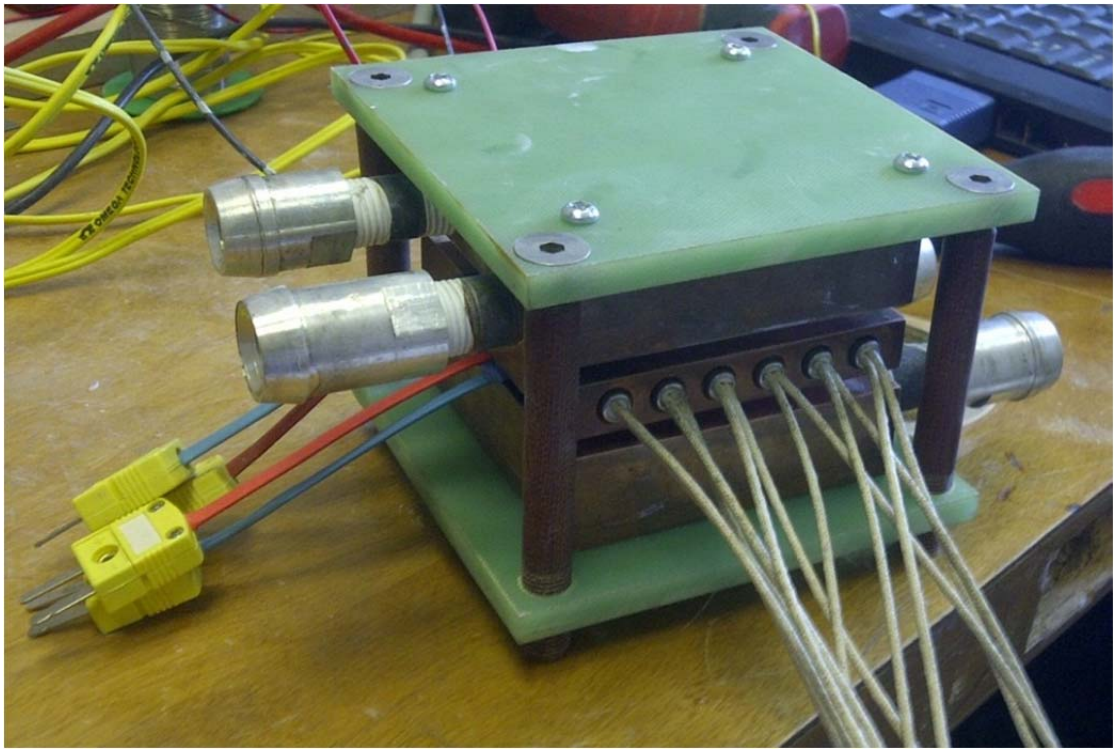

Figure 55: Heating block

3.3.2. TEST SCHEDULE

While the previous tests examined how the TE module performs at the maximum operating conditions, this experiment examines the recommended range. To prevent damage to the TE module, manufacturers typically recommend that they be run between 30% and 70% of I_{max}. In the previous experiment, it was found that there are deviations from the datasheets to actual testing. For this experiment, the resulting I_{max} values were used to determine the operating points, this was done to protect the module along with providing verification. A total of 24 tests were performed under varying loads. These are outlined in Table 20.

Table 20: Heat Test Schedule

Operating Parameters					Custom TE		Crystal		Kyrotherm	
Iteration	**% Imax**	**Th (°C)**	**Tc (°C)**	**ΔT (°C)**	**I (A)**	**E**	**I (A)**	**E**	**I (A)**	**E**
Test 1	30	27	17	10	4.57	0.661	4.26	0.628	6.25	0.537
Test 2	50	27	17	10	7.62	0.661	7.10	0.628	10.41	0.537
Test 3	70	27	17	10	10.67	0.661	9.94	0.628	14.58	0.537
Test 4	30	27	7	20	4.57	1.368	4.26	1.232	6.25	1.074
Test 5	50	27	7	20	7.62	1.368	7.10	1.232	10.41	1.074
Test 6	70	27	7	20	10.67	1.368	9.94	1.232	14.58	1.074
Test 7	30	27	-3	30	4.57	2.090	4.26	1.615	6.25	1.625
Test 8	50	27	-3	30	7.62	2.090	7.10	1.615	10.41	1.625
Test 9	70	27	-3	30	10.67	2.090	9.94	1.615	14.58	1.625
Test 10	30	27	-13	40	4.57	2.992	4.26	2.866	7.08	2.294
Test 11	50	27	-13	40	7.62	2.992	7.10	2.866	10.41	2.294
Test 12	70	27	-13	40	10.67	2.992	9.94	2.866	14.58	2.294
Test 13	30	50	40	10	4.05	0.712	3.87	0.713	6.74	0.578
Test 14	50	50	40	10	6.75	0.712	6.45	0.713	11.24	0.578
Test 15	70	50	40	10	9.44	0.712	9.03	0.713	15.73	0.578
Test 16	30	50	30	20	4.05	1.386	3.87	1.444	6.74	1.155
Test 17	50	50	30	20	6.75	1.386	6.45	1.444	11.24	1.155
Test 18	70	50	30	20	9.44	1.386	9.03	1.444	15.73	1.155
Test 19	30	50	20	30	4.05	2.027	3.87	1.935	6.74	1.724
Test 20	50	50	20	30	6.75	2.027	6.45	1.935	11.24	1.724
Test 21	70	50	20	30	9.44	2.027	9.03	1.935	15.73	1.724
Test 22	30	50	10	40	4.05	2.813	3.87	2.630	6.74	2.350
Test 23	50	50	10	40	6.75	2.813	6.45	2.630	11.24	2.350
Test 24	70	50	10	40	9.44	2.813	9.03	2.630	15.73	2.350

The 24 iterations are broken down into two categories; a T_h of 27°C and T_h of 50°C. Within each of these categories the modules were then run at a ΔT of: 10, 20, 30 and 40 accomplished by setting the T_c to the correct respective value. To get a range of operating conditions for each ΔT the modules were tested at 30%, 50% and 70% of the $I_{max}/\Delta T_{max}$ condition measured during the Seebeck test.

Only three modules were tested at this time as the previous work confirmed that the TE technology modules did not have the required cooling capacity and that the Thermonamic devices had failed in all 3 attempts. The remaining 3 modules were evaluated using this test schedule to determine which would exhibit the best performance

3.3.3. RESULTS

The operation of the test bench was a challenge due to the multitude of operating parameters that had to be met. Since the Seebeck voltage is based on the temperature difference, it causes many fluctuations while testing. Initially the current was set to the required value. The heater voltage was then adjusted to bring the ΔT into the necessary range. Due to the Seebeck effect a TE voltage could change by 2.5V from a ΔT of 10 to a ΔT of 40, all while the TE current remained constant. This was quite a challenge as fine tuning of the fluid flow rate, heater voltage and TE voltage was required to produce accurate results. Two types of results are shown, the tables contain all the information used to determine the performance of the module. The important factors are Q_c, Q_h, COP and the ΔT's. Q_c is the ability of the TE module to remove heat, while Q_h indicates how much work the heat exchanger is doing. The COP is the efficiency of the system, measured by comparing the heater input power and that of both TE modules. The ΔT's and flow are used to measure Q_h indicating which TE module is performing more work.

3.3.3.1. Custom TE

The Custom TE module did not perform to its expected potential. Figure 56 compares the experimental values to those on the datasheet. The experimental values are significantly lower in all cases, with the largest deviation occurring at a ΔT of 10°C. Through experimentation it was found that under real conditions the TE modules are unable to perform as they would in a vacuum. Table 15 shows a portion of the collected data, one of the main concerns is the low COP value found. To be competitive with present cooling technologies, the COP must be > 1, and testing shows that this is only

possible at low ΔT's which occur when small amounts of cooling are required. This module gave only 5 test points that exhibit a COP above 1.0. Due to the fact the manufacturers' spec does not correlate to the experimental results this module would have to be tested throughout its entire operating ranger to determine accurate operating characteristics, however its results were not at all impressive.

Table 21: Cooling Capacity Testing - Custom TE

Test	Qc (W)	Qc/ Module (W)	TE 1 Power	TE 2 Power	ΔT-TE 1 fluid	ΔT-TE 2 fluid	ΔT TE 1	ΔT TE 2	COP	Qh TE 1 (W)	Qh TE 2 (W)	Qh Total (W)
ΔT-10 @27°C	94.3	47.1	29.7	30.9	0.3	0.3	10.1	9.8	1.6	82.9	78.3	161.2
	210.5	105.2	82.6	82.8	1.1	1.2	10.3	9.3	1.3	158.3	180.4	338.7
	278.0	139.0	160.2	160.0	1.1	1.0	11.1	9.2	0.9	282.0	264.4	546.4
ΔT-20 @ 27°C	63.0	31.5	33.4	33.5	0.3	0.6	20.3	20.5	0.9	61.9	88.7	150.6
	146.7	73.3	86.1	85.9	0.6	0.6	20.4	19.8	0.9	160.3	152.1	312.3
	213.3	106.7	164.9	163.6	1.2	1.2	20.7	19.2	0.7	253.8	255.8	509.6
ΔT-30 @ 27°C	4.7	2.3	34.5	35.6	0.1	0.1	29.4	29.5	0.1	34.1	24.0	58.0
	84.3	42.1	89.9	89.4	0.5	0.4	30.1	29.7	0.5	122.9	115.4	238.3
	138.4	69.2	167.7	166.7	1.5	1.3	30.9	29.6	0.4	248.3	218.5	466.8
ΔT-40 @ 27°C	0.0	0.0	73.0	73.1	0.3	0.6	39.9	39.9	0.0	0.0	0.0	0.0
	19.9	10.0	94.3	93.7	0.7	0.6	40.1	40.0	0.1	102.4	90.8	193.1
	69.8	34.9	172.0	171.7	1.0	0.9	40.8	39.7	0.2	205.8	181.9	387.7
ΔT-10 @50°C	148.6	74.3	36.9	33.6	1.2	1.2	10.1	9.3	2.1	92.1	94.3	186.5
	247.1	123.5	95.5	91.7	0.7	0.7	10.2	7.9	1.3	207.2	198.0	405.2
	313.6	156.8	182.3	175.7	1.1	1.0	11.1	8.1	0.9	322.0	310.4	632.4
ΔT-20 @50°C	100.2	50.1	42.2	38.9	0.3	0.3	20.2	19.0	1.2	77.6	73.0	150.6
	185.0	92.5	98.3	97.4	0.7	1.2	20.3	20.4	1.0	176.6	251.9	428.4
	245.9	123.0	189.9	182.4	1.1	1.0	23.0	20.3	0.7	304.7	290.4	595.1
ΔT-30 @50°C	31.5	15.8	40.1	36.3	0.4	0.5	30.2	29.3	0.4	47.1	45.5	92.6
	109.4	54.7	94.9	89.6	0.5	0.6	30.5	29.0	0.6	130.9	121.9	252.7
	179.2	89.6	188.6	180.1	1.0	1.2	30.6	28.7	0.5	264.2	249.4	513.5
ΔT-40 @50°C	0.0	0.0	56.2	56.6	0.1	-0.6	39.4	40.1	0.0	0.0	0.0	0.0
	43.4	21.7	92.1	86.2	0.4	0.4	40.3	38.8	0.2	105.2	86.7	191.9
	112.0	56.0	197.2	187.5	0.9	1.0	40.3	38.8	0.3	254.8	221.3	476.2

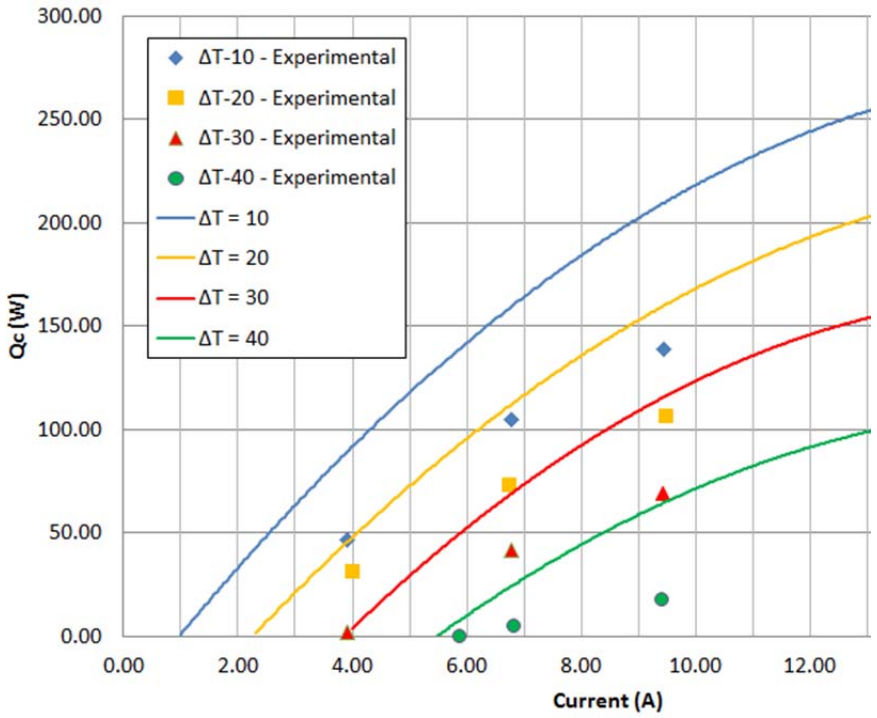

Figure 56: Standard Performance graph Qc vs. I @ T_h = 27 - Custom TE

3.3.3.2. Crystal

Crystal provides minimal specifications for their modules, this presents a challenge when attempting to benchmark to their data. The performance graph at T_h = 27°C, Figure 57, outlines the cooling capacity for the Crystal TE module. The only information provided was a max Q_c value of 340.3 W. For this module that would occur at ΔT = 0°C with a V_{in} of 14.9 V. Looking at the experimental graph, the values obtained are significantly below these targets. For each 10°C lower ΔT the Q_c, improves by about 20 W. Extrapolating the data would indicate a value of about 185 W peak cooling, 45% less than the data sheet indicated it was capable. These results are similar to previous testing which showed the module was only capable of 60% the rated current. As with the Custom TE module the COP values are also very low, with only 4 tests showing COP

greater than 1.0. The inability of this module to perform hinders its use within a high powered heat exchanger.

Table 22: Cooling Capacity Testing - Crystal

Test	Qc (W)	Qc/ Module (W)	TE 1 Power	TE 2 Power	ΔT-TE 1 fluid	ΔT-TE 2 fluid	ΔT-TE 1 (°C)	ΔT-TE 2 (°C)	COP	Qh TE 1 (W)	Qh TE 2 (W)	Qh Total (W)
ΔT-10 @27°C	148.5	74.2	46.3	46.3	0.5	0.5	10.1	10.1	1.6	110.6	108.9	219.4
	232.3	116.1	119.0	119.7	1.1	1.1	10.1	9.9	1.0	224.6	229.1	453.7
	291.5	145.7	223.5	224.7	1.8	1.5	10.4	9.7	0.7	349.0	349.3	698.3
ΔT-20 @ 27°C	90.0	45.0	48.8	48.3	0.4	0.5	20.1	20.3	0.9	98.4	87.1	185.5
	168.7	84.4	116.5	116.8	0.9	0.9	20.0	20.0	0.7	186.4	186.0	372.4
	241.5	120.8	243.9	244.3	2.1	1.6	20.1	20.0	0.5	409.7	347.9	757.6
ΔT-30 @ 27°C	31.1	15.5	49.8	49.9	0.3	0.3	30.0	30.2	0.3	65.0	61.1	126.1
	111.3	55.6	124.8	125.0	0.9	0.9	29.9	30.0	0.5	184.7	178.2	362.8
	169.5	84.7	236.9	237.5	1.7	1.4	30.3	29.9	0.4	312.0	290.3	602.3
ΔT-40 @ 27°C	50.9	25.5	128.8	128.6	0.7	0.7	40.5	40.8	0.2	157.9	144.9	302.86
	106.5	53.3	241.7	242.4	1.7	1.4	39.9	40.0	0.2	293.2	277.0	570.2
	-	-	-	-	-	-	-	-	-	-	-	-
ΔT-10 @50°C	148.5	74.2	40.2	40.4	1.1	1.2	10.4	9.4	1.8	100.6	101.5	202.0
	247.4	123.7	112.5	111.9	0.8	1.1	10.5	9.4	1.1	220.1	230.1	450.2
	316.0	158.0	211.5	210.7	1.2	1.7	10.2	9.4	0.8	343.6	344.6	688.3
ΔT-20 @ 50°C	97.9	49.0	42.8	43.0	1.3	1.4	20.4	19.8	1.1	78.3	64.2	142.4
	190.5	95.3	117.1	116.7	0.7	1.0	20.5	19.6	0.8	195.1	194.4	389.5
	250.6	125.3	216.8	215.3	1.2	1.6	20.6	19.7	0.6	331.2	324.7	655.8
ΔT-30 @ 50°C	46.1	23.1	47.0	47.5	0.2	0.2	30.2	29.7	0.5	53.3	44.4	97.6
	125.8	62.9	110.5	110.1	0.5	0.8	29.4	29.6	0.6	153.5	159.6	313.1
	186.9	93.5	213.2	212.2	1.1	1.4	30.3	29.7	0.4	295.3	288.6	583.9
ΔT-40 @ 50°C	-	-	-	-	-	-	-	-	-	-	-	-
	56.9	28.5	130.2	129.7	0.8	0.8	39.6	43.5	0.2	153.7	140.5	294.2
	130.1	65.0	218.2	217.6	1.0	1.2	40.5	40.0	0.3	276.7	257.1	533.8

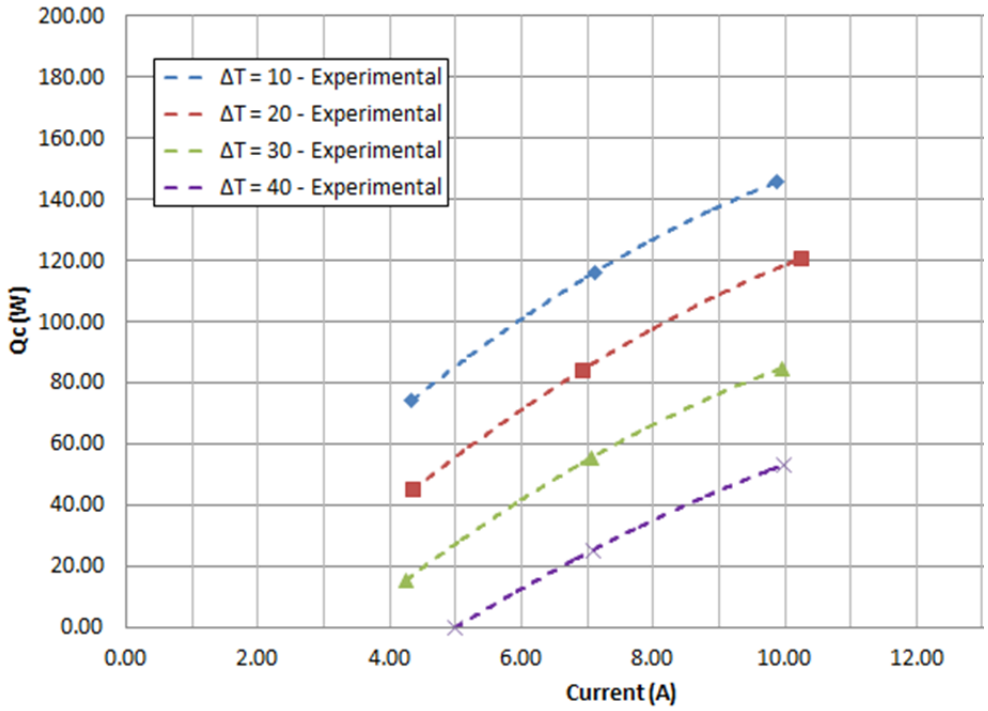

Figure 57: Standard Performance graph Qc vs. I @ T_h = 27 - Crystal

3.3.3.3. Kyrotherm

Kyrotherm is one company that provides software enabling the user to determine which module will perform the best for their given application. This software allows the generation of detailed graphs based on the specific operating conditions. As with the earlier tests, this module outperformed its competition. Figure 58 shows the performance of the module, the dotted line indicates the measured values while the solid line represents the specifications from Kyrotherm. In all cases, the deviation is less than 10%, and might be partially experimental error. While the rated cooling capacity of this module was on par with those from Custom TE and Crystal, experimental results show it achieved 65 W more cooling than Crystal, and 71 W more than Custom TE at ΔT = 10°C, while achieving a much higher COP than both. By having access to the Kyrotherm software graphs showing expected COP could be generated. Figure 59 compares supplier's the

computed and the experimentally measured values. The results again show that the measured values are within a 10% deviation of the manufacturer specifications. This brings some confidence towards the use of their software and product.

From Table 23, the basic information required for heat exchanger design can be extracted. It can be seen that the hot side of the module would require a heat exchanger with at least 500 W capability as Q_h was 497 W when ΔT = 10°C and T_h was 50°C.

Table 23: Cooling Capacity Testing - Kyrotherm

Test	Qc (W)	Qc/ Module (W)	TE 1 Power	TE 2 Power	ΔT-TE 1 fluid	ΔT-TE 2 fluid	ΔT-TE 1 (°C)	ΔT-TE 2 (°C)	COP	Qh TE 1 (W)	Qh TE 2 (W)	Qh Total (W)
ΔT-10 @27°C	191.5	95.8	40.4	40.7	0.5	1.0	10.0	10.3	2.4	130.7	164.8	295.5
	317.4	158.7	105.0	106.2	1.1	1.6	10.0	10.2	1.5	231.6	252.3	483.9
	421.8	210.9	203.7	205.5	1.8	2.7	9.9	10.1	1.0	375.2	394.4	769.6
ΔT-20 @ 27°C	125.6	62.8	43.9	44.5	0.9	1.0	19.6	20.0	1.4	145.0	105.0	250.0
	242.2	121.1	111.9	112.8	0.8	1.3	20.2	20.7	1.1	201.5	225.5	427.0
	330.7	165.4	203.9	206.0	1.8	2.6	20.0	20.6	0.8	335.0	349.4	684.4
ΔT-30 @ 27°C	53.5	26.8	48.5	49.2	0.2	0.4	30.0	30.0	0.6	60.7	80.3	140.9
	170.4	85.2	118.4	120.2	0.7	1.1	29.6	29.6	0.7	141.8	201.4	343.2
	253.8	126.9	214.2	216.1	1.7	3.1	30.2	30.7	0.6	305.9	403.0	708.9
ΔT-40 @ 27°C	0.0	0.0	60.7	61.8	0.7	0.8	40.5	40.4	0.0	51.6	57.4	109.0
	88.9	44.5	119.7	120.8	0.7	1.2	40.1	40.3	0.4	137.9	166.8	304.7
	176.6	88.3	221.8	224.1	1.5	2.6	39.6	39.8	0.4	274.0	335.2	609.2
ΔT-10 @50°C	239.9	119.9	51.0	51.1	1.0	1.5	9.6	10.1	2.4	115.6	117.6	233.2
	393.2	196.6	136.7	138.5	1.1	2.0	9.9	10.3	1.4	279.9	302.5	582.4
	503.4	251.7	267.2	267.7	1.8	3.1	9.8	10.3	0.9	469.1	497.2	966.3
ΔT-20 @ 50°C	170.4	85.2	53.0	53.7	0.6	1.0	19.8	20.1	1.6	51.0	48.0	99.0
	313.4	156.7	139.4	140.1	1.9	2.1	19.9	20.0	1.1	255.1	208.6	463.7
	416.7	208.3	267.9	270.4	1.5	2.8	20.1	20.8	0.8	421.0	456.8	877.8
ΔT-30 @ 50°C	98.1	49.1	59.0	59.3	0.4	0.4	30.1	30.5	0.8	102.4	65.2	167.6
	234.8	117.4	144.9	146.3	0.9	1.5	29.9	30.1	0.8	162.4	185.2	347.6
	333.0	166.5	281.4	281.4	2.2	3.6	29.6	30.2	0.6	415.9	436.8	852.7
ΔT-40 @ 50°C	30.3	15.2	59.1	59.7	0.7	1.1	39.8	39.9	0.3	53.7	50.9	104.6
	157.9	78.9	145.4	146.6	0.6	1.1	39.8	39.9	0.5	118.9	138.9	257.9
	251.3	125.7	283.6	285.3	1.7	2.7	40.2	40.4	0.4	370.3	402.1	772.4

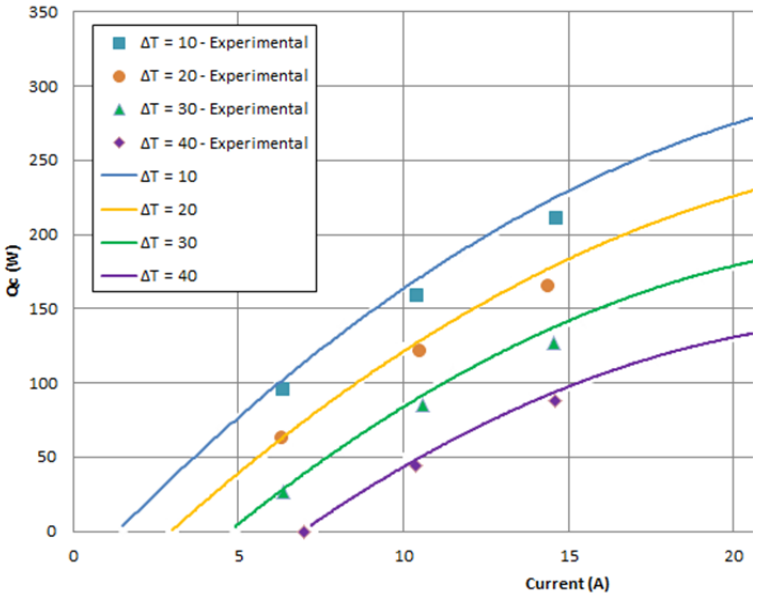

Figure 58: Standard Performance graph Qc vs. I @ T_h = 27 - Kyrotherm

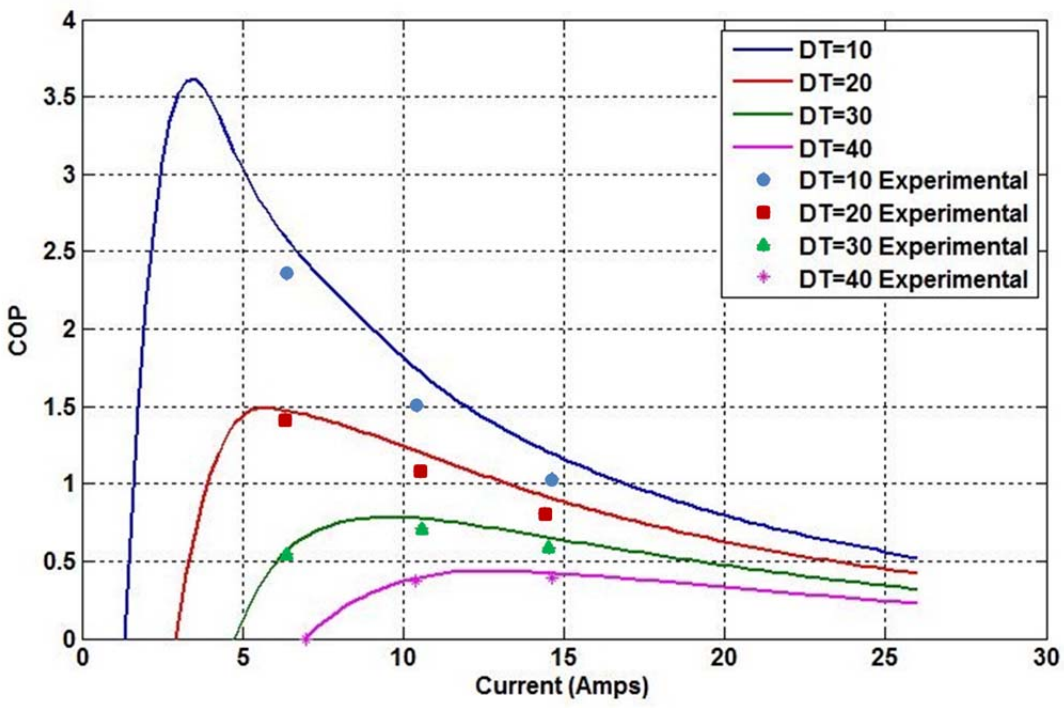

Figure 59: Standard Performance graph COP – Kyrotherm, and measured points

3.4. CONCLUSIONS

Testing the modules under steady heat load confirmed the results from the previous Seebeck experiments as the modules exhibited commensurate performance levels. The Kyrotherm unit performed the best by far, followed by Custom TE, TE Tech, Crystal and finally Thermonamic. When looking solely at the manufactures' specifications, suppliers appeared to offer products of similar performance, claiming cooling capacities around 350 W, with input power requirements of ~ 500 W and nearly the same ΔT_{max}. Experimentation showed only the Kyrotherm module met the claims, a take-away being that only high quality TE modules need be considered. Doubtless, suppliers other than the ones examined may carry equally good or perhaps even slightly better products, but experimental verification of performance is truly an essential step.

During testing the importance of uniform pressure within the test apparatus became quite apparent; uneven pressure resulted in the failure of a TE module. This was ascertained when the testing results appeared skewed and a positive lead unsoldered itself, as shown in Figure 60. Upon removal the module showed signs that the thermal paste had not contacted the positive terminal side against the heat exchanger. Figure 61 compares this particular assembly (a) with one that had good thermal contact (b). To prevent failure of modules during subsequent tests much extra care was taken to ensure uniform pressure was always applied to the TE modules.

Figure 60: TE module failure

(a) (b)

Figure 61: Thermal paste after TE removal, a) TE failure, b) successful test

To achieve high efficiency thermo-electric cooling/heating, the TE module must be paired to the best possible heat exchanger. For testing performed up to this point, an off the shelf flat plate multipass copper heat exchanger was used with thermal paste at the interface. To achieve its theoretical performance, the Kyrotherm module chosen for development efforts had to be paired with an even higher efficiency heat exchanger. The next chapter will look at heat exchange designs that greatly aid in the goal of achieving a higher efficiency battery thermal management system based on thermoelectrics.

CHAPTER 4 – HEAT EXCHANGER TESTING

4.1. INTRODUCTION

With an appropriate TE module selected for the given application, an extended effort was now to put into developing a heat exchanger that would provide optimal performance for the system. A variety of designs were researched, with application of RMF's becoming the clear choice to pursue. Traditionally high costs have limited their application but with the product becoming available through the Asian market, RMF's can offer a lightweight, cost competitive and efficient solution. To determine which foam might be optimal for the application, different copper and aluminum samples were tested; along with a variety of pore sizes and flow paths. The data collected was analyzed to determine each configuration's thermal performance, pumping energy consumption and pressure drop. Suitable performance trade-offs were sought for applicability to the automotive Environment.

4.1.1. TESTING PARAMETERS

4.1.1.1. Flow rate and Pressure

The ideal operating range of the heat exchanger is dependent on the system it is operating within. The HX designed for the EV battery requires it to have the highest performance while minimizing energy consumption. The coolant pump found in the thermal management system on the vehicle was used to define reasonable pressure and flow limitations for the heat exchanger. A Bosch PAD circulation pump is used in the vehicle's coolant system, the pump operating curves with 50% ethylene glycol/50% water are shown in Figure 62. The vehicle's ESS was designed to operate at a maximum of 5 psi,

while the pump itself can attain 10 psi at low flow rates. To ensure the ESS maintains a pressure below 5 psi, there must be approximately 5 psi pressure drop throughout the rest of the system. This can in part be obtained by engineering a pressure drop though the addition of foam in the HX. As the pump's flow rate increases the pumping power required increases and the working pressure decreases. To maximize the pump's effectiveness a flow rate should be chosen to balance the HX performance and pressure loss. Analyzing the pump's operating characteristics, it peaks in efficiency between 15-20 LPM, and thus the system would ideally maintain flow in this range, with the flow divided across the number of TE-HX units operating.

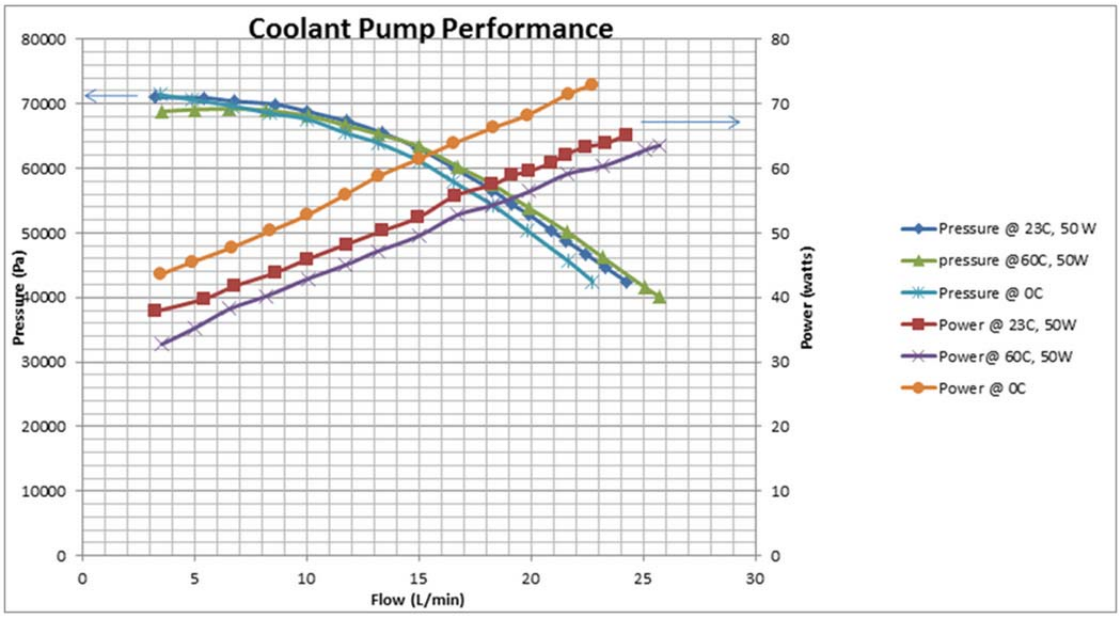

Figure 62: Bosch PAD water circulating pump characteristics

The fluid path impacts flow velocity and thus performance of the various configurations. Figure 63 shows the velocity characteristics of 3 flow paths, the S-path has the highest velocity, while the cross flow has the lowest in an open cross section. In the same respect the S-path sees the largest pressure difference while the cross flow has the

smallest for the same pumping effort. The internal velocity chosen must be balanced with the heat capacity of the fluid, pressure losses and pumping effort.

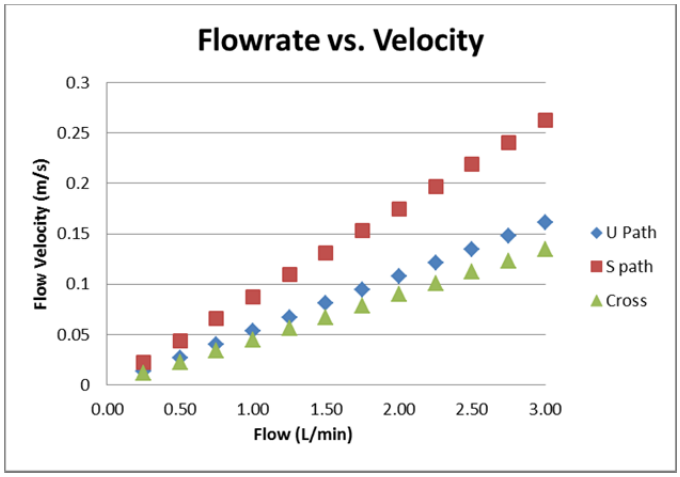

Figure 63: Path dependent flow velocity

To determine which flow rate provides optimal performance and efficiency each heat exchanger was tested at: 1.0 L/min, 1.5 L/min and 2.0 L/min for test #1, while test #2 was performed through the pump's entire range. It must be stated that analysis outside this work indicated that up to ~10 heat exchanger units working in parallel might constitute a viable heat pump unit, supplied by a single pump, hence the range of flow rates examined. If the pumping power increases linearly in relation to the heat transfer capacity the net effect on system efficiency is relatively low. Since the operative ΔT across the TE module inevitably includes losses across the two HX's, achieving the highest heat transfer coefficient is key to lowering the total ΔT, and thereby raising the system COP. The primary investigative goal was to identify a HX design that maximized h for a practical pumping pressure loss of ~20-30 KPa (3-5 psi) and 2 LPM flow rate.

4.1.1.2. Foam

As outlined previously the porosity and compression of the foam plays a vital role in its effectiveness as a heat exchange medium. For experimental purposes both 10 PPI and 40 PPI foams are used as these are both commercially available in aluminum and copper. Through research, Ozmat [**26**] has shown that compressing the foam improves its effectiveness in heat exchangers. Once baseline measurements for each flow path were taken, foam was compressed to determine the improvements possible. The amount of compression possible is dependent on the flow path, due to variation in flow velocities. Table 25 outlines the various testing configurations, foam characteristics and compression ratios examined.

The compression ratios for tests # 2 to 6 were determined by the available material, flow path height and heat exchanger design. Lessons learned from the first 6 tests led to the design and manufacturing of the heat exchangers used in tests # 7 to 12. This later design was optimized for manufacturing, packaging space, compression ratio, cost and performance. Certain assumptions were made when designing the cross flow heat exchanger, these are outlined below.

- The material will have even brazing on both sides, with minimal pressure losses due to build-up of braze alloy.
- Uniform material crush can be accomplished.
- Uniform heat distribution will occur over the surface area.
- Flow bypasses and material warpage will not be present.

4.1.1.3. Temperature differential

The temperature range across which the heat pump operates must be minimized to ensure its effectiveness in a TE system. Chapter 2 outlines the theory behind the TE module's performance, as shown, a lower ΔT value corresponds to much higher system COP. Thus a more effective a heat exchanger translates directly and powerfully towards the efficiency of the entire system. Ideally one would like to maintain a total $\Delta T < 10°C$, as this is the range with mostly superior COP values.

The input temperature used for testing is set at 40°C; this was chosen as a severe, but not worst case, condition for the vehicle. To simulate driving conditions each flow rate was tested under different heat loads. The initial tests were run under 4 heat loads: 50 W, 100 W, 150 W and 200 W. After analyzing the results, the 50 W heat input data was found to contain noisy data attributed to the low flow rate operating condition across the HX, thus it was omitted from further tests.

4.1.2. TEST #1 – HEAT EXCHANGER WITH TE MODULE

A heat exchanger utilized in a battery thermal management system will encounter variable working conditions. To understand how each variant performs under such conditions, a test schedule was developed to replicate key parameters in order to lead to an optimized configuration. The range of test points enabled a comparison of the HX designs throughout their operating range. As outlined in Table 24, the key factors can be categorized in three distinct areas: the TE module, heat load and flow rate. The TE module was run at 30%, 50% and 70% of its I_{max} value. The second variable is the heat load, which fluctuates with usage and demand. A copper heater plate was used to simulate

the heat load and operated at 3 test points: 100 W, 150 W and 200 W. The third variable is the heat exchanger design itself. To improve heat transfer, the system was tested at flow rates of 1.0, 1.5 and 2.0 LPM. The drawback to higher flow rates is the higher pumping power requirement along with greater pressure drop in the system. Trade-offs among these parameters are not well understood for RMF heat exchangers, thus the data is key to determining the viability of the technology discussed.

Table 24: HX Test Schedule A

% I max	Current (A)	HTR Wattage (W)	Flow rate (LPM)
30	6.74	100	1.0, 1.5, 2.0
		150	1.0, 1.5, 2.0
		200	1.0, 1.5, 2.0
50	11.24	100	1.0, 1.5, 2.0
		150	1.0, 1.5, 2.0
		200	1.0, 1.5, 2.0
70	15.73	100	1.0, 1.5, 2.0
		150	1.0, 1.5, 2.0
		200	1.0, 1.5, 2.0

Each HX flow path configuration was tested to the above schedule. Table 25 lists the major differences between each test. For the non-production intent designs, a baseline was taken, followed by insertion of 10 PPI and 40 PPI foams. Tests 1-6 were run first, the results from these early experiments led to the brazed and cross flow design using 40 PPI foam with variations in foam compression. Compression was performed in the z-direction for the initial tests than biaxially (x-y) for the remainder.

Table 25: Heat exchanger configurations

	Flow Path	Foam	Compression
Test 1	U Block	No foam	-
Test 2	U Block	12.7 mm x 10 PPI Aluminum	23% z-direction
Test 3	U Block	12.7 mm x 40 PPI Aluminum	23% z-direction
Test 4	S Block	No foam	-
Test 5	S Block	12.7 mm x 10 PPI Aluminum	23% z-direction
Test 6	S Block	12.7 mm x 40 PPI Aluminum	23% z-direction
Test 7	Cross Flow – No Foam	No foam	-
Test 8	Cross Flow – No Crush V0	6.35 mm x 40 PPI Copper	6% z-direction
Test 9	Cross Flow – No Crush V1.0	6.35 mm x 40 PPI Copper	6% z-direction
Test 10	Cross Flow – No Crush V2.0	6.35 mm x 40 PPI Copper	6% z-direction
Test 11	Cross Flow – 4x Crush V1.0	6.35 mm x 40 PPI Copper	4x-75%- Biaxial
Test 12	Cross Flow – 4x Crush V2.0	6.35 mm x 40 PPI Copper	4x-75%- Biaxial

KR Reynolds metal foam density: 7-9%

4.1.3. TEST #2- HEAT EXCHANGER

Testing the heat exchangers independent of the TE modules is an important step to understand and verify their performance. Such tests were inspired by the experiments performed by Boomsma et al. [**50**]. The difference between these experiments and the earlier ones is the absence of the TE module, with the heater placed in direct contact with the HX. This removes the uncertainty that the TE module introduces, helping to limit the experimental error. For these tests the heater output was increased to 880 W in an attempt to improve experimental accuracy by generating larger temperature signals and reducing the fraction of extraneous losses to the environment. To obtain data over a larger range, two pumps were tied in series increasing the system flow rate. The only input parameter adjusted was the flow rate, the first test point was dependent on the maximum resultant flow for a given foam compression. It was then reduced incrementally giving a range of values to plot; the test schedule is outlined in Table 26.

Table 26: HX Test Schedule B

Foam Configuration	Flow rate (LPM)
No Foam	2.0-8.0; 7pts
Foam-No Crush V0	1.0-6.0; 11pts
Foam- No Crush V1.0	1.0-6.0; 11pts
Foam- No Crush V2.0	1.0-6.0; 11pts
Foam-4x Crush V1.0	0.5-2.75; 6pts
Foam- 4x Crush V2.0	0.5-2.75; 6pts

For consistent results the system test was allowed to stabilize for 10 minutes prior to recording the first data. For the subsequent test points the flow rate was adjusted and stabilized for 5 minutes before recording data. Such tests were only performed on the cross flow configuration. There were 3 different tests with uncrushed foam. V0 and V1.0 were trial runs for manufacturing. When the second batch of HX's were made, it was decided to test different foam densities, including an extra uncrushed version to see if the results were repeatable.

4.2. HEAT EXCHANGER EXPERIMENTS

The heat exchanger tests were designed to compare different materials, flow paths and foams densities. Two test bench configurations were employed, the first one is the same as described in chapter 3, with the addition of a flow bypass line in the plumbing. The second was an improved version based on lessons learned featuring greater flexibility and testing accuracy. Experiments began with benchmarking the open flow path and ended with testing foams of various compression.

4.2.1. TEST BENCH

4.2.1.1. Initial Set-up

The initial heat exchanger test bench set-up was the same as used for the TE module testing. As shown on Figure 64, a fluid bypass line was added to better simulate the actual working conditions of the pump, as it is designed to operate at a certain minimum flow rate. This setup was useful to achieve good flow rate control for the large range of backpressures encountered. One modification included the addition of two aerogel blankets to limit the heat flow into the mounting plates. Figure 65 depicts this configuration with an S flow path heat exchanger installed. The electrical schematic can be found in Appendix A.

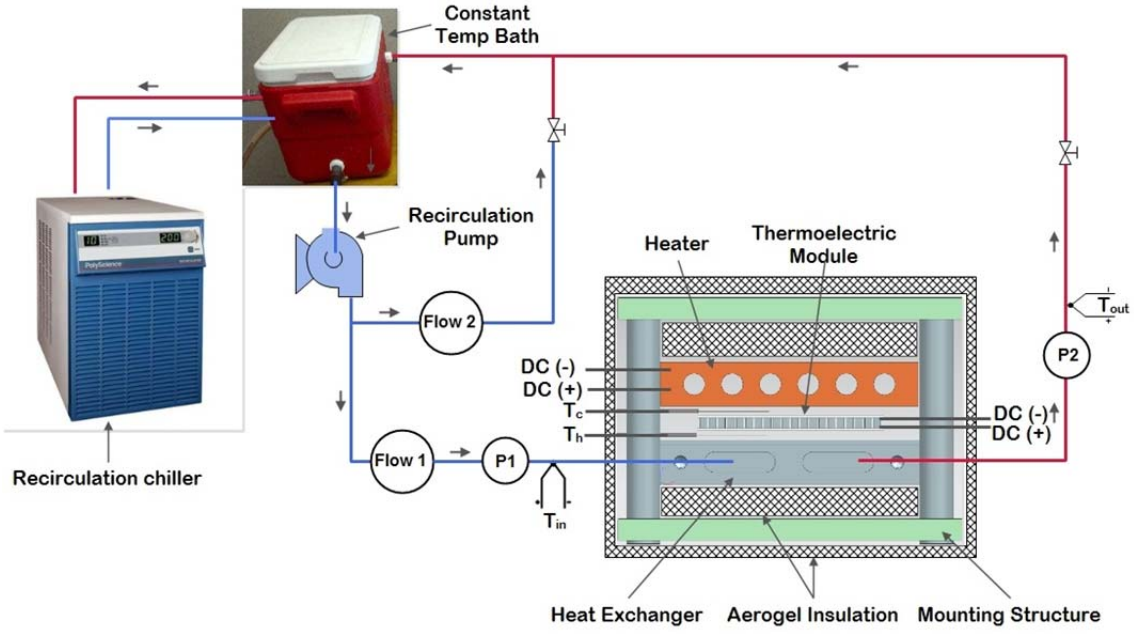

Figure 64: Heat Exchanger test bench

Figure 65: Heat exchanger set-up

The test bench was designed to fit different heat exchanger configurations. The first two HX's were machined in-house out of 6061-T6 aluminum plate, then wet sanded with 1500 grit on a surface plate for a flat and smooth finish. The first flow path examined was U shaped, i.e. the inlet and outlet are on the same side. Figure 66 shows both an empty cavity and one filled with 10 PPI foam. The second flow path was S shaped which increased the mean fluid velocity at a given flow rate. This flow path is depicted in Figure 67, with an empty cavity and one filled with 10 PPI foam. The dimensions for both of these heat exchangers were 65 mm x 65 mm allowing the largest of the TE modules to fit atop the fluid cavity. The cavity depth was 10 mm, into which a 12.9 mm thick block of aluminum foam was compressed to fit, amounting to a 23% crush in the Z-direction.

(a) (b)

Figure 66: Heat Exchanger - U flow path, a) without foam, b) with foam

(a) (b)

Figure 67: Heat Exchanger - S flow path, a) without foam, b) with foam

4.2.1.2. 2nd Set-up

Analysis from the initial tests showed inconsistent results and warranted a redesign of the test bench, Section 4.3.2.1. outlines the inclusive results. The deviation was rooted within the thin flat strip temperature sensors used and their location. Despite this fact the failure was not solely a consequence of the temperature measurements. It was deemed necessary to improve measurement accuracy through a redesign. With the knowledge gained from the initial set-up a few key features were found to be required:

- Pressure sensors need be consistently at the same height to ensure accurate differential readings.
- Stationary flow meters, as they can be affected by position.
- Uniform pressure application upon the TE modules.
- Expandable thermal insulated housing to accommodate various geometries.
- Temperature sensors need to be embedded into their respective surfaces.
- Better wiring and plumbing for repeatability.

The new set-up used the same fluid flow path and electrical set-up. The major difference was in the assembly mounting apparatus. The initial test bench used 4 pins around the HX periphery to apply pressure and hold the components together. The re-designed version uses two rods centrally located that are able to apply approximately 1000 lbs of load upon a fulcrum which spreads uniformly on the assembly. It also rigidly mounts all the flow meters, pressure and fluid temperature sensors. To measure the temperature at the face of the TE module, 4 thermocouples were embedded into the ceramic face by grinding shallow trenches and covering in epoxy. Also, 0.020" holes were drilled into the walls of the HX and heater respectively to measure their face temperatures. These locations and the general arrangement are depicted in Figure 69 & 69. The electrical schematic is shown in Appendix A.

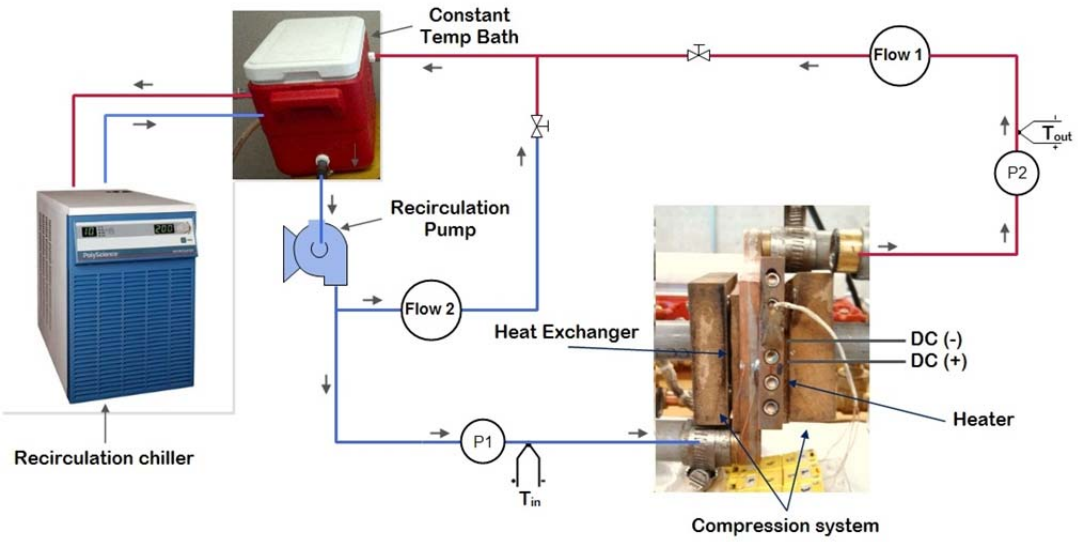

Figure 68: Revised HX Test Bench

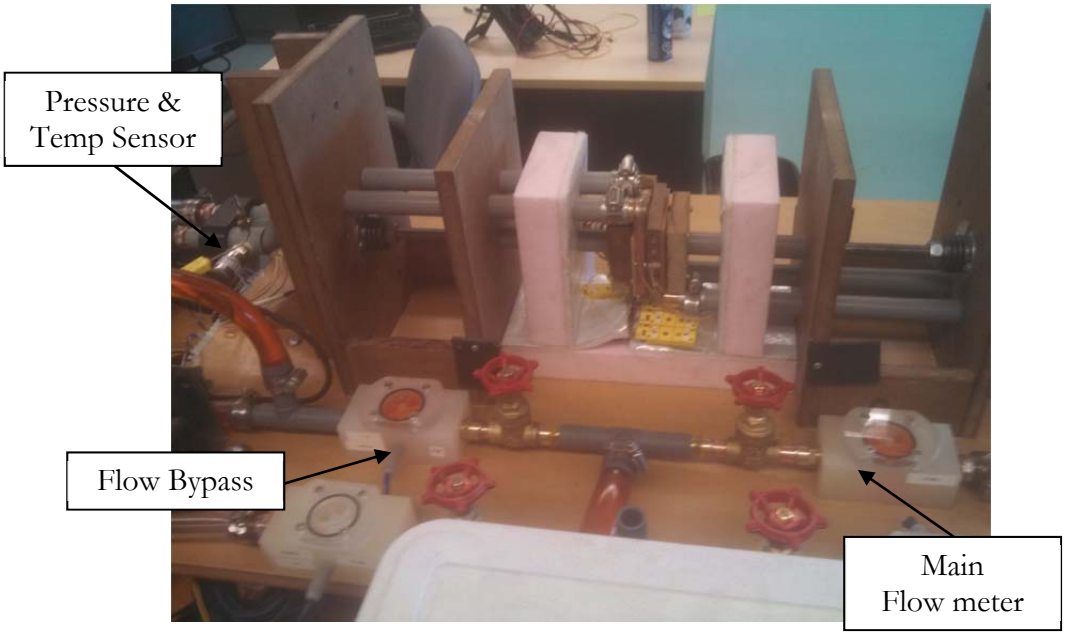

Figure 69: Revised HX Test Bench

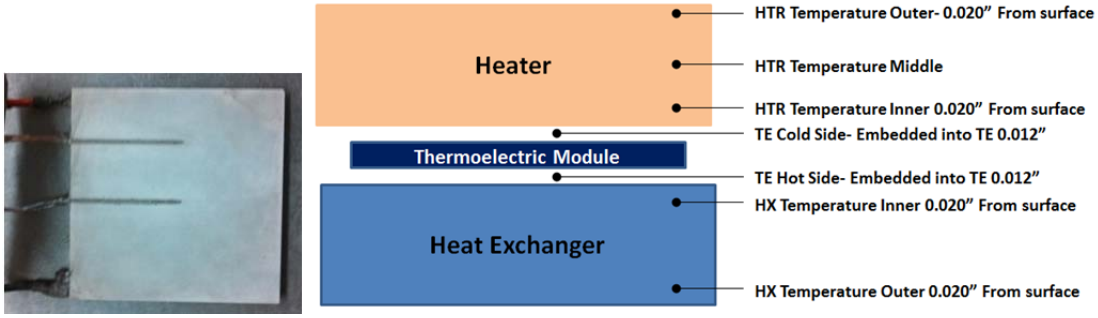

Figure 70: Thermocouple arrangement

The initial HX configurations tested used a gasket and were fastened together with screws. Their construction was meant to gain some initial experience prior to further refinement. The results from these tests led to the CNC machined and vacuum furnace brazed cross flow designs which minimize pumping losses and capitalize on full contact of the foam with the base plate. This locates the inlet and outlet in an optimal location for the scaling of a modular HX system closer to a production intent. The shape of the inlet and outlet flow passage remained the same for all the later configurations; the only difference was using foam of various compressions. The foam samples only came in one

size, when crushed this required multiple pieces to be fitted within the flow channel. The uncrushed foam was one piece while the 4x foam had four. Figure 71 shows how the foam was arranged within the HX for each configuration. Brazing was carried out within a vacuum oven; this process begins with a silver alloy brazing paste applied to all contact surfaces. For the uncrushed foam this constituted the two sides in contact with the outer walls, and the walls themselves. For the crushed foams all 6 sides of the foam along with the walls of the HX were coated. At this point the HX's were placed in a compression jig designed to apply pressure uniformly, to aid the distribution of solder and seal the two halves. The assembly was then placed in the brazing oven with the temperature profile gradually increasing over a 6 hour span to ~ 800°C then the metal is cooled with the introduction of nitrogen gas.

(a) (b)

Figure 71: Heat Exchangers, a) No Crush, b) 4X Crush

4.2.2. RESULTS

The thermal performance was quantified via the overall heat transfer coefficient, thermal resistance, Nusselt's number, Reynolds number and Colburn factor. Work input was quantified through the pumping power, pressure losses, flow velocity and ΔP/L values. Plots are generated as a visual aid to give a thorough understanding, and show which HX performs the best under the conditions outlined. The results are broken up in 2 groups. The first round of testing was performed with a TE module in place. Testing in this manner was time consuming and results varied significantly. The revised test bench provided stable results, as long as care was taken when assembling the module. The thermal performance graphs are first reviewed for each HX configuration. The numerical results are then discussed, looking specifically at the heat transfer coefficients in each system.

4.2.2.1. Initial Test Bench

The initial test bench was unable to provide consistent results. This did not become apparent until the data was plotted using the non-dimensional thermal properties. These plots showed the configurations which had realistic results, and identified ones with excessive experimental error. The set-up was used for 6 months before it was determined a revised test bench would be required to ensure greater experimental accuracy. It was theorized that the thermocouple's position were a key source of the problem. The permeability plots for the 4 flow paths are shown in Appendix C. The S-path had higher velocity due to the smaller cross sectional area. Most of the ΔP was due to the small fittings used, not the foam or flow path. Secondly the thermocouples were tested against a benchmark. Results later showed the thermocouple style (a metal foil strip at the

interface) was easily damaged and could not provide consistent readings. In addition, with each side of the thermocouple exposed to a hot and cold face, it was impossible to assign the measured temperature to either side.

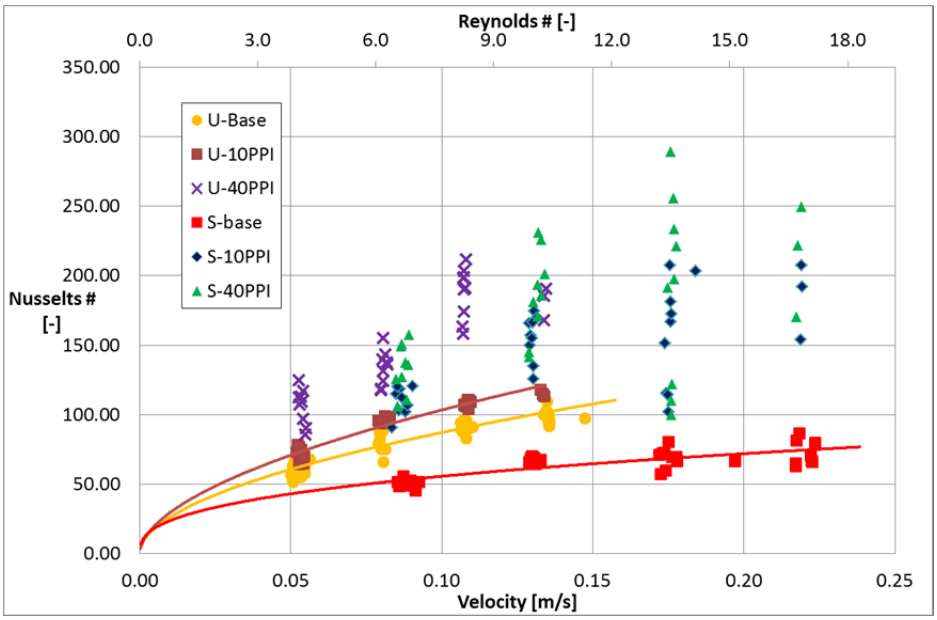

Figure 72: Initial testing - Convective heat transfer

The average heat transfer coefficients measured are outlined in Table 27, and represented graphically in Figure 72. The large standard deviation seen within a given flow rate were pointing to large experimental uncertainty stemming from the experimental set-up. To improve accuracy the bench and HX housing were redesigned, as mentioned.

Table 27: Initial testing Heat transfer coefficient

	S-Path h_{system}	U-Path h_{system}
Flow path	**(W/m^2 C)**	**(W/m^2 C)**
1.0 LPM @ Base	2287.90	2682.60
1.5 LPM @ Base	3110.10	3810.97
2.0 LPM @ Base	3134.49	3953.60
1.0 LPM @ 10 PPI	5554.24	3201.20
1.5 LPM @ 10 PPI	7864.72	4220.46
2.0 LPM @ 10 PPI	7801.68	4736.75
1.0 LPM @ 40 PPI	7001.88	4957.69
1.5 LPM @ 40 PPI	9788.45	6123.80
2.0 LPM @ 40 PPI	9912.31	8757.21

4.2.2.2. Revised Bench HX Results-Test #1

The thermal performance of the HX must not come at the expense of high energy consumption from pumping fluid. A balance needs to be reached to attain a high COP for the entire system. One way to show this relationship for the HX is to graph the pumping power against its thermal resistance, Figure 73 depicts this relationship. During testing the only variable was the foam and brazing inside the HX. One can thus conclude that the No Crush V1.0 foam HX performed the best as its locus of performance points lies closest to the origin. The test point that best balances the thermal performance with pumping power occurs at a flow rate of 2.0 LPM, thermal resistance of 0.015 K/W, pumping power of 0.083 W for an overall heat transfer coefficient of 7,939 W/m^{2}K. Another method that could be used to evaluate performance is entropy production or exergy destruction. However such sophistication tends to be more suitable in a system wide analysis rather than single component evaluations.

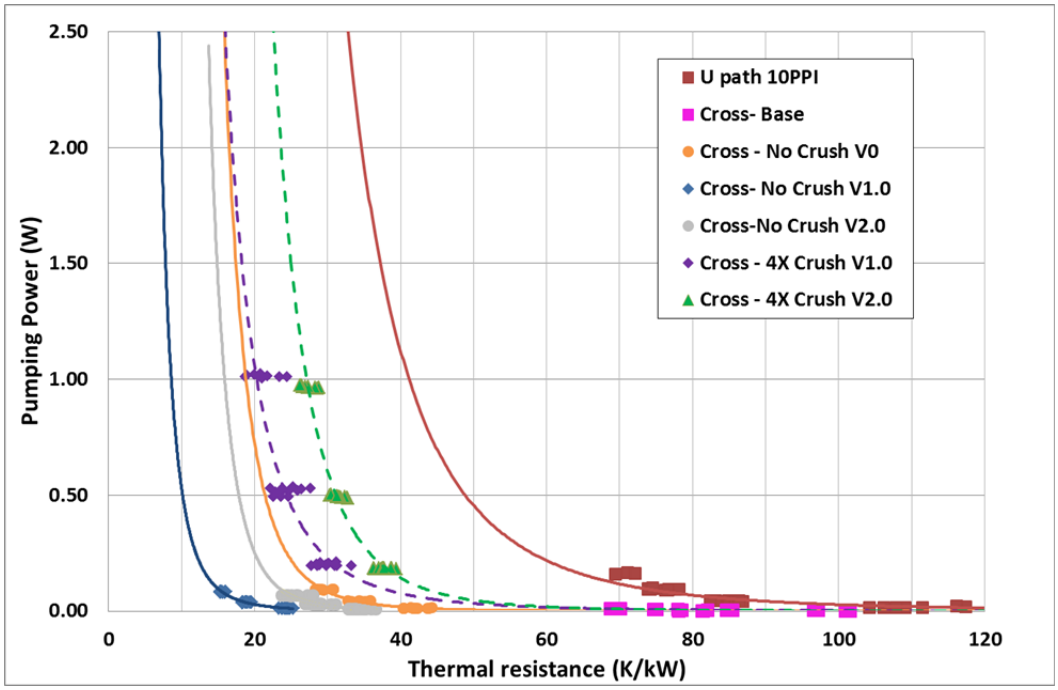

Figure 73: Thermal performance vs. Energy consumption

The second graph, Figure 74, looks at the convection heat transfer within the system. Larger Nusselt numbers indicate there is superior heat transfer between the surface and the fluid flowing past it. An incremental improvement from the No Crush V2.0, V0 and 4x foams is seen but their performance was lower than the No Crush V1.0 foam. These results were unexpected and gave indication something had gone very wrong.

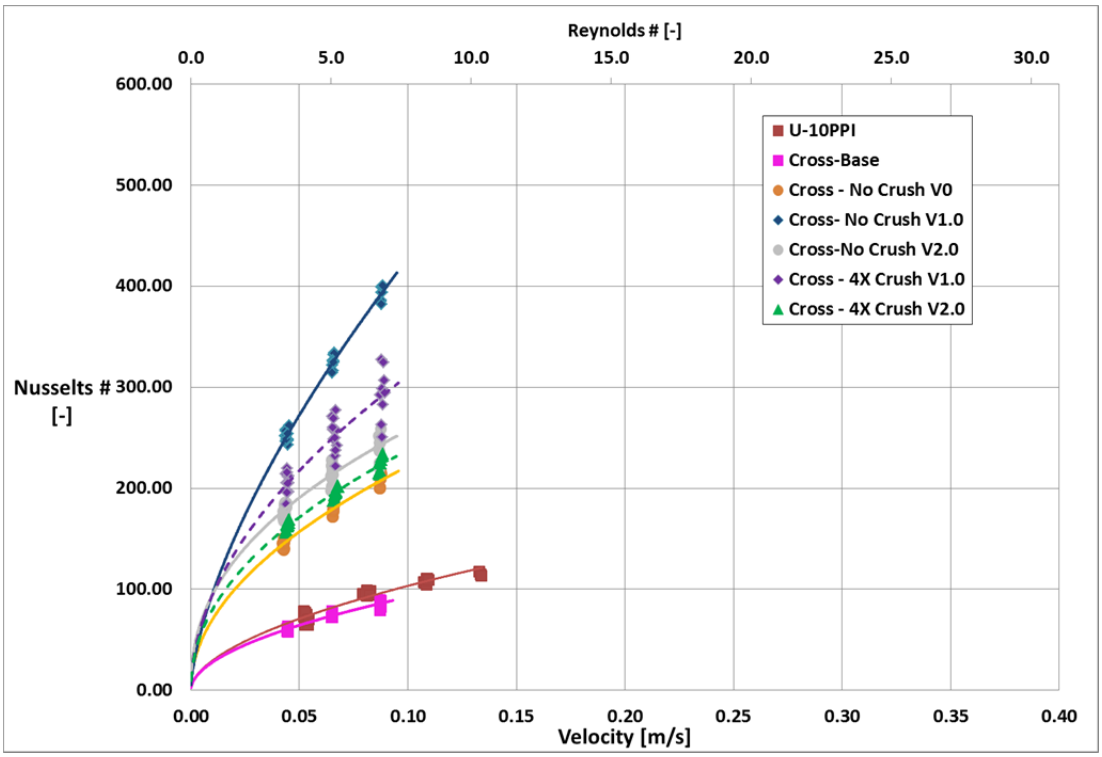

Figure 74: Heat Convection - HX Test 1

The last graph plots the Colburn factor against Reynolds number. This gives the heat transfer performance normalized for fluid properties, comparing the convection coefficient to the required flow rate for heat transfer. From an overall efficiency standpoint, it is always better to run any HX system at lower flow, since the heat transfer does not keep pace with the increased flow rate. However the best performing HX's are still the No Crush configurations as these exhibited the highest Colburn j factor for a given Reynolds number.

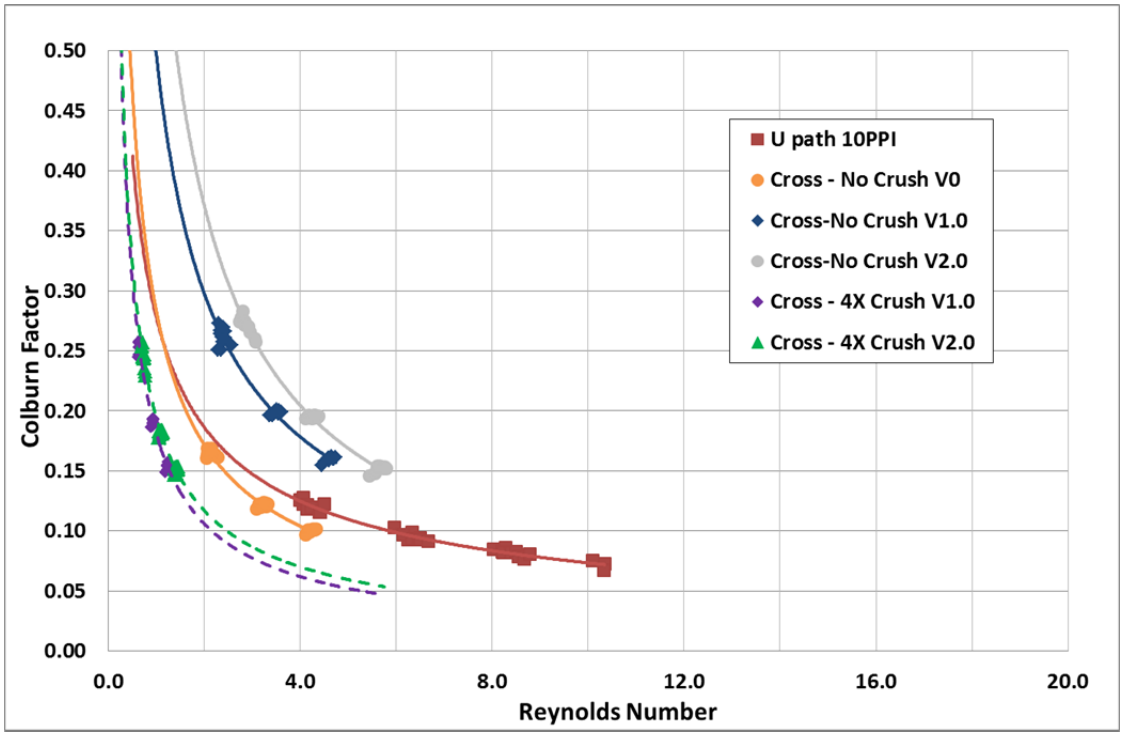

Figure 75: Colburn factor vs. Reynolds Number - HX Test #1

Table 28 outlines the heat transfer within the system. The interaction between the TE module, thermal paste, HX and heater is shown along with the HX's internal convection heat transfer. It becomes apparent there is an issue with the inconsistent contact resistance h_c values. Large fluctuations in the results indicate there is inconsistency in the experimental set-up or data. After some analysis the error was traced to the thermocouples embedded into the TE module. The TE module was tested in two orientations; at first it was used for the No Crush V0 testing; the TE module was then flipped over and the polarity reversed. This orientation was used for the remaining tests, and caused a disconnect in the V0 results for h_c.

Table 28: Cross flow heat transfer results - Test 1

	h_{system}	"$h_{Contact}$" TE thermal paste to HX	"$h_{Convective}$" Fluid Inside HX	"$h_{Contact}$" Heater to TE thermal paste
Flow path	**(W/m² C)**	**(W/m² C)**	**(W/m² C)**	**(W/m² C)**
1.0 LPM @ Base	1796	3660	2649	27286
1.5 LPM @ Base	2134	4099	3273	27162
2.0 LPM @ Base	2263	4134	3633	27896
1.0 LPM @ No Crush V0	3910	6466	7430	36910
1.5 LPM @ No Crush V0	4361	7012	8664	39307
2.0 LPM @ No Crush V0	4746	7436	9851	38315
1.0 LPM @ No Crush V1.0	6396	9265	15500	19969
1.5 LPM @ No Crush V1.0	7113	9930	18821	19518
2.0 LPM @ No Crush V1.0	7600	10292	21804	19742
1.0 LPM @ No Crush V2.0	6472	13120	9631	20165
1.5 LPM @ No Crush V2.0	6913	13255	10898	20719
2.0 LPM @ No Crush V2.0	7130	13182	11725	21164
1.0 LPM @ 4x Crush V1.0	6312	10792	11512	23238
1.5 LPM @ 4x Crush V1.0	6882	11378	13258	24256
2.0 LPM @ 4x Crush V1.0	7348	11795	14871	24923
1.0 LPM @ 4x Crush V2.0	5999	12888	8452	24355
1.5 LPM @ 4x Crush V2.0	6627	13788	9576	25630
2.0 LPM @ 4x Crush V2.0	7160	14334	10740	26233

The overall accuracy of the test bench can be cross-checked by an energy balance approach. The heater's input plus the I^2R losses of the TE module must appear as heat removed by the HX at steady state (minus ambient, plumbing / electrical conduction & radiation losses). An example calculation is presented below in Eq. 40, a small correction is also included here for the fluid pumping heat contribution. Experimental results showed on average 15 W or ~5% goes missing to extraneous convection and conduction losses through the insulation and plumbing. A sample calculation is shown below with data from Appendix C, Table 31, no crush V0 at 150 W heater input.

$$Heat\ Load = V_{HTR} \cdot I_{HTR} + (V_{Applied} - \propto \Delta T_{TE}) \cdot I_{TE} + \left(\left(P_{Pump} \cdot 0.8 - \dot{V} dp \right) \cdot \left(\frac{Q_{main}}{(Q_{main} + Q_{bypass})} \right) \right) \quad (40)$$

$$Heat\ Load = 40.31 \cdot 3.73 + (12.57 - 1.11) \cdot 11.45 + \left((11.44 \cdot 0.8 - 0.0438) \cdot \left(\frac{1.51}{(1.51 + 5.35)} \right) \right)$$

$$= 150.44 + 129.73 + 2.00 \ = 282.2\ W$$

$$Heat\ Loss = Heat\ Load - Q_h$$

$$= 282.2 - 267.7 = 14.5\ W$$

4.2.2.3. Revised Bench HX Results-Test #2

The second test set reviews the performance of the heat exchanger independent of the TE module. The results from all heat exchangers tested are reviewed based on performance graphs derived from the methods introduced by Boomsma et al. [**50**]. The data spans a large range of the coolant pump's flow rate, where the previous experiment only looked at an operational range anticipated with the cooling needs of the TE module.

The permeability factor k_p defines how easily liquid flows through the foam, values of 1 indicate fully open passages, while 0 indicates complete blockage. This is shown graphically in Figure 76 with pressure loss/unit length vs. the flow velocity; the results are generated using Eq. 35. Permeability tests showed a difference between the two uncrushed foams. During post mortem analysis V1.0 was found to contain foam with smaller pore size which led to a higher pressure loss. During this analysis the 4x Crush V2.0 foam was also found to have no solder present between the foam and HX walls. This caused 1 segment of foam to shake loose, creating flow bypasses, and the net result was a permeability factor lower than the 4x Crush V1.0 configuration. The in depth post mortem analysis can be found in section 4.3.2.4.

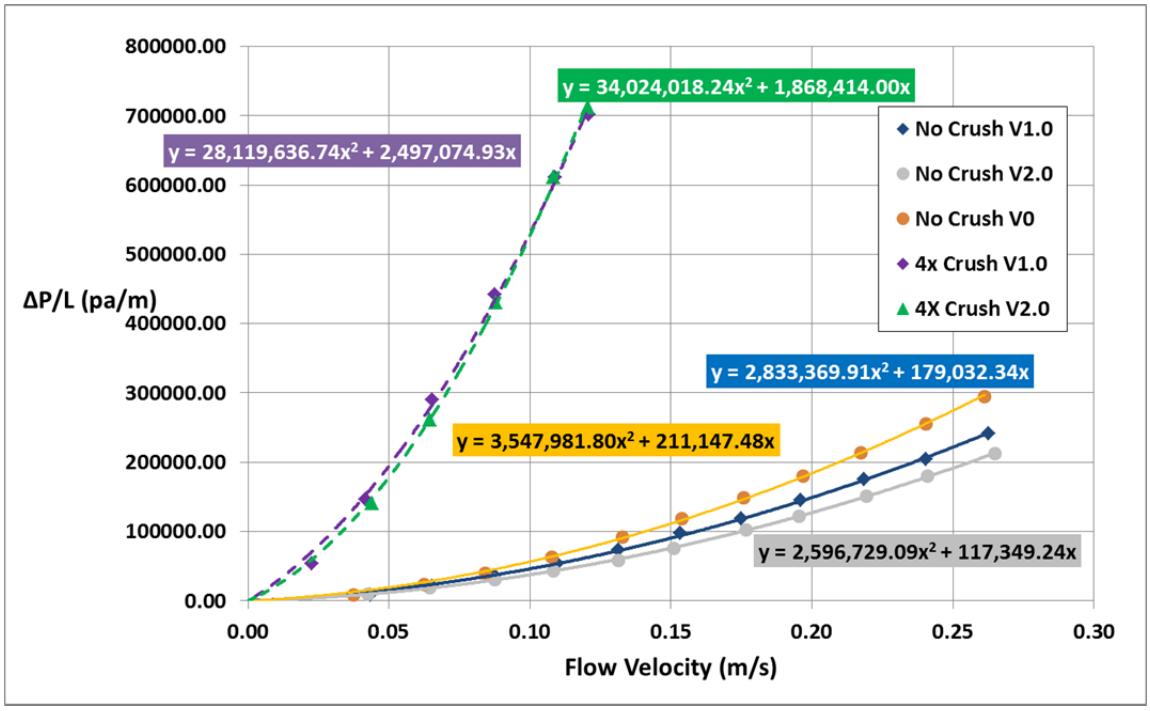

Figure 76: Pressure loss/ unit length vs. Flow Velocity

Table 29: Permeability factors

Flow Configuration	Permeability Factor (K_p)	$\frac{\mu}{K_p}$ (from graph)
No Crush V0	1.06E-08	211,147
No Crush V1.0	1.25E-08	179,032
No Crush-V2.0	1.91E-08	117,349
4x Crush V1.0	8.99E-10	2,497,074
4x Crush V2.0	1.20E-09	1,868,414

The No Crush V1.0 HX had the highest tested thermal performance. This result is best captured in Figure 77, and Figures 84-85 which can be found in Appendix C, Table 33. Reviewing the data in Figure 77, an optimal balance between thermal performance and energy consumption occurs at a flow rate of 2.5 LPM where the pumping power is 0.142 W, a thermal resistance of 0.0180 K/W and heat transfer coefficient of 18,107 W/m^{2}K results. Its locus of data points lies closest to the origin. Upon inspection this HX was the only configuration that showed any significant bonding between the foam and HX walls.

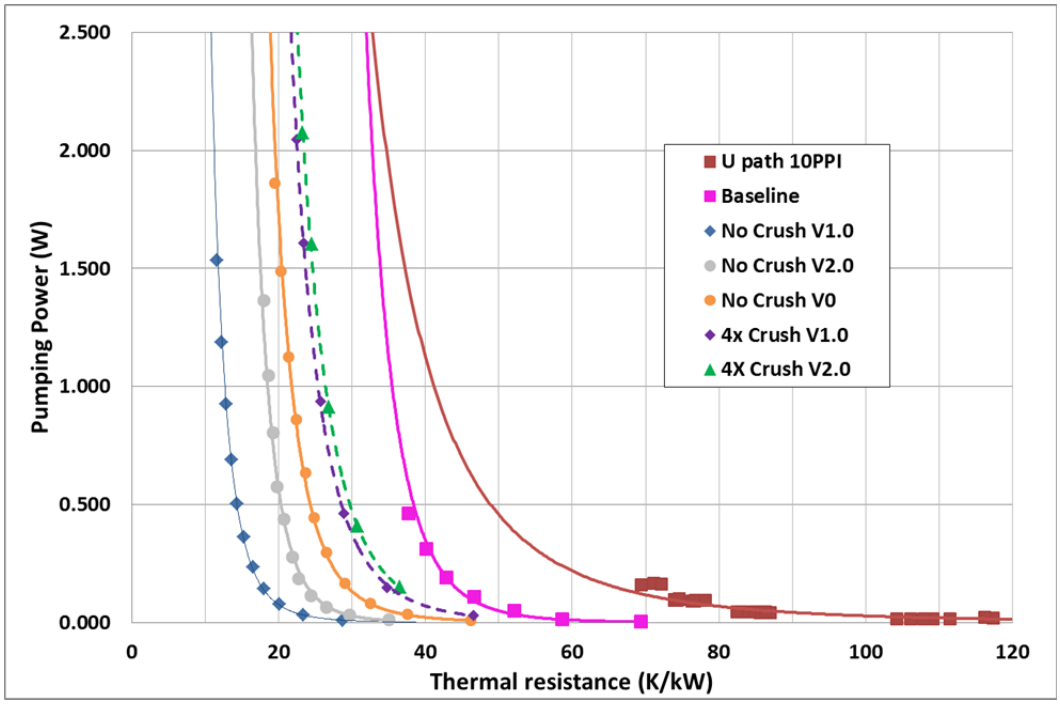

Figure 77: Pumping power vs. Thermal resistance

The heat transfer coefficient values were noticeable different between the two sets of tests. Table 30 outlines the results from test #2 at 2.0 LPM, the full results are shown in Appendix C, Table 33. The measured $h_{contact}$ values during test #1 varied from 19,518 to 39,307 W/m^{2}K, likely as a result of poor setup. Test #2 had more stable results with $h_{contact}$ values ~55,000 W/m^{2}K. This demonstrated that there was better surface contact and less measurement error. Convective heat transfer coefficients indicate the internal performance of a HX, both sets of tests confirmed that the No Crush V1.0 performed the best, but with a deviation of 24% (16,558 vs. 21,804 W/m^{2}K) the exact result remains elusive. The $h_{contact}$ values measured ranged 2 to 16% change within these individual test set-ups. The placement of thermocouples, superior surface contact and removal of TE module is attributed for reducing the source of this difference. The results from test #2 gave better indication on the potential performance of the HX's with respect to the attainable contact conductance.

Table 30: Cross flow heat transfer results @ 2.0 LPM-Test 2

	h_{system}	"$h_{contact}$" Heater to HX	"$h_{convective}$" Fluid Inside HX
Flow path	**(W/m^2 C)**	**(W/m^2 C)**	**(W/m^2 C)**
2.0 LPM @ Base	4966	46646	5450
2.0 LPM @ No Crush V0	8092	50675	9335
2.0 LPM @ No Crush V1.0	13212	54479	16558
2.0 LPM @ No Crush V2.0	10212	57715	11978
2.0 LPM @ 4x Crush V1.0	10584	58224	12474
2.0 LPM @ 4x Crush V2.0	10063	58667	11741

The brazing of the foam is a key step to ensure the thermal performance of the HX. While performing the experiments it was demonstrated that the $h_{contact}$ values can be ~55,000 W/m^{2}K. During two of the test runs h_c was down around 33,000 W/m^{2}K, shown in Table 31. To verify this data the heater was placed on the opposite side of the HX; these tests resulted in $h_{contact}$ values of ~55,000 W/m^{2}K. Such inconsistency might have been due to the flatness of the faces or variation of the thermocouple signal from either side of the HX. Another suspicion was that brazing joint existed mostly on one face of the HX, causing a difference in the temperature gradient across the copper, hence influencing contact value results.

Table 31: HX Test results – No Crush V0 & 4x Crush V1.0

Flow rate 1 (Main)	HTR Power	Δ Pressure	ΔT- Fluid	HX Fluid LMTD	HTR Wall Temp	HX Wall Temp	Heat into coolant (Qh)	ΔT From Heater to HX	Pumping Power	"$h_{contact}$" HX to Heater interface Input Q	HX, "$h_{convective}$" based on input Q	"h", System, based on input Q	"h", System, based on exit Q
LPM	W	psi	°C	°C	°C	°C	W	°C	W	W/m^{2}K	W/m^{2}K	W/m^{2}K	W/m^{2}K
No Crush V0 (Side A)													
6.0	879	2.72	2.3	42.0	60.1	56.9	819	3.2	1.86	55,977	14,693	12,056	11,225
5.5	877	2.35	2.5	42.1	60.7	57.5	818	3.3	1.49	55,230	14,153	11,662	10,878
5.0	879	1.97	2.7	42.2	61.6	58.2	812	3.4	1.12	53,421	13,600	11,220	10,366
4.5	878	1.66	3.0	42.3	62.4	59.0	810	3.4	0.86	52,857	13,040	10,816	9,988
4.0	879	1.37	3.3	42.6	63.5	60.0	807	3.5	0.63	51,995	12,490	10,406	9,551
3.5	871	1.10	3.8	42.9	64.5	61.2	812	3.2	0.44	55,594	11,796	10,023	9,342
3.0	890	0.85	4.4	43.2	65.9	62.6	815	3.3	0.30	56,079	11,355	9,715	8,894
2.5	880	0.58	5.5	43.7	68.2	64.7	817	3.5	0.16	52,247	10,363	8,893	8,260
1.9	870	0.37	7.0	44.4	71.1	67.5	816	3.6	0.08	50,675	9,335	8,092	7,587
1.4	886	0.22	9.4	45.5	75.0	71.6	815	3.4	0.04	53,234	8,406	7,428	6,840
0.9	890	0.07	16.2	48.5	83.5	79.9	846	3.5	0.01	52,267	7,020	6,313	6,004
No Crush V0 (Side B)													
6.0	883	2.72	2.3	41.9	62.3	57.1	821	5.2	1.88	35,235	14,407	10,745	9,991
5.4	884	2.30	2.4	41.9	63.0	57.8	807	5.2	1.44	35,328	13,798	10,410	9,507
5.0	884	1.94	2.7	42.0	63.8	58.5	814	5.2	1.11	34,863	13,306	10,095	9,292
4.5	882	1.62	3.0	42.2	64.7	59.4	817	5.3	0.83	34,175	12,690	9,691	8,976
3.9	885	1.31	3.4	42.3	65.8	60.5	817	5.3	0.59	34,477	12,048	9,331	8,611
3.5	884	1.06	3.8	42.5	67.0	61.6	811	5.4	0.42	34,100	11,458	8,951	8,212
3.0	884	0.81	4.5	42.8	68.6	63.1	810	5.4	0.28	33,696	10,787	8,515	7,801
2.5	883	0.56	5.4	43.1	70.6	65.1	814	5.5	0.16	32,955	9,988	7,974	7,351
2.0	883	0.41	6.6	44.1	73.2	67.6	816	5.6	0.10	32,693	9,299	7,517	6,951
1.5	882	0.22	9.3	45.2	77.3	72.0	832	5.4	0.04	34,075	8,186	6,820	6,428
1.0	847	0.09	14.4	47.6	84.2	78.7	851	5.5	0.01	31,962	6,751	5,740	5,764
4x Crush V1.0 (Side A)													
2.8	886	6.46	4.9	43.3	62.4	59.2	815	3.2	2.05	57,841	13,792	11,506	10,587
2.5	891	5.62	5.4	43.6	63.2	60.0	814	3.2	1.61	58,251	13,430	11,266	10,290
2.0	888	4.07	6.7	44.2	65.0	61.8	813	3.2	0.93	58,224	12,474	10,584	9,690
1.5	893	2.67	9.0	45.2	67.7	64.5	817	3.2	0.46	57,893	11,483	9,854	9,016
0.9	869	1.35	14.4	47.6	72.8	69.7	832	3.1	0.15	57,390	9,734	8,528	8,163
0.5	877	0.50	27.2	53.0	84.0	80.8	863	3.2	0.03	57,401	7,838	7,037	6,921
4x Crush V1.0 (Side B)													
2.7	881	6.71	5.0	42.9	64.8	59.3	811	5.5	2.08	33,188	13,274	9,955	9,160
2.5	883	6.04	5.4	43.4	65.7	60.3	819	5.4	1.75	33,713	12,968	9,819	9,111
2.0	880	4.35	6.7	44.1	67.7	62.3	819	5.4	1.00	33,972	11,968	9,251	8,603
1.5	880	2.72	9.2	45.3	70.8	65.6	822	5.2	0.46	35,099	10,762	8,572	8,007
1.0	881	1.54	13.8	47.4	75.3	70.4	848	4.9	0.18	37,010	9,477	7,810	7,519
0.5	878	0.54	27.2	52.9	86.7	82.9	884	3.8	0.03	47,535	7,281	6,457	6,501

The second test set-up was an essential tool to better understand the limitations and issues with the HX. Initially the errors were believed to be a by-product of the test set-up rather than the HX's. Later analysis indicated that the issues stemmed from the HX construction, with the brazing and foam compression as the main culprits. The following section provides an overview of the issues uncovered after disassembling the HX's.

4.2.2.4. Post Mortem Analysis

The dissection of the HX's provided insight on their poor performance. It was apparent the brazing techniques had failed with limited bonding between the foam ligaments and HX wall surfaces. The multiple pieces of foam required to fill the cavity also played a role in reducing HX performance.

The No Crush V0 was the first HX to be manufactured in the crossflow configuration, and thus did not benefit from a compression jig later utilised to clamp the HX's together in the vacuum furnace. The periphery of the foam had good bonding while the remainder of the surface showed none. The darker colour in Figure 78 indicates the area where no silver solder was present. This was apparent on both sides of the foam indicating the foam had minimal thermal contact with the HX surface, leading to its poor results.

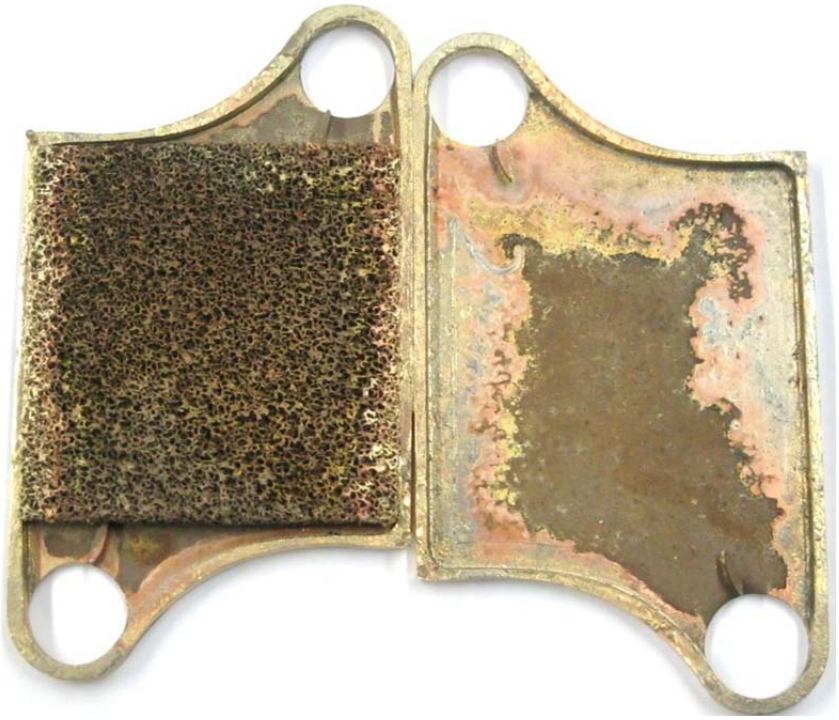

Figure 78: No Crush V0 HX

Upon initial inspection both the No Crush V1.0 & V2.0 foams were contaminated with a dark oily sludge seen in Figure 79. While the origins are unknown, it is believed to be a mixture of oil/ethylene glycol emanating from a piece of test bench tubing in the loop. During manufacturing the uncompressed foams were constructed with two different silver solders. A comparison of the V1.0 and V2.0 after cleaning is shown in Figure 80. The high fluidity silver solder used in No Crush V1.0 showed some bonding, while other areas ~1/2" wide were able to be lifted. V1.0 appears to have smaller pores, with no contamination, while V2.0 had larger pores and was also contaminated by a soft solder. The dark areas in the V2.0 HX are a soft solder that was used to seal the HX's outer periphery after the vacuum brazing had failed to fully seal the unit. This solder leaked into the main cavity plugging some pores and distributing itself on the surface; it had a lower thermal conductivity than its silver based counterpart reducing the HX's overall thermal performance.

Figure 79: No Crush V2.0 prior to cleaning, showing oily sludge

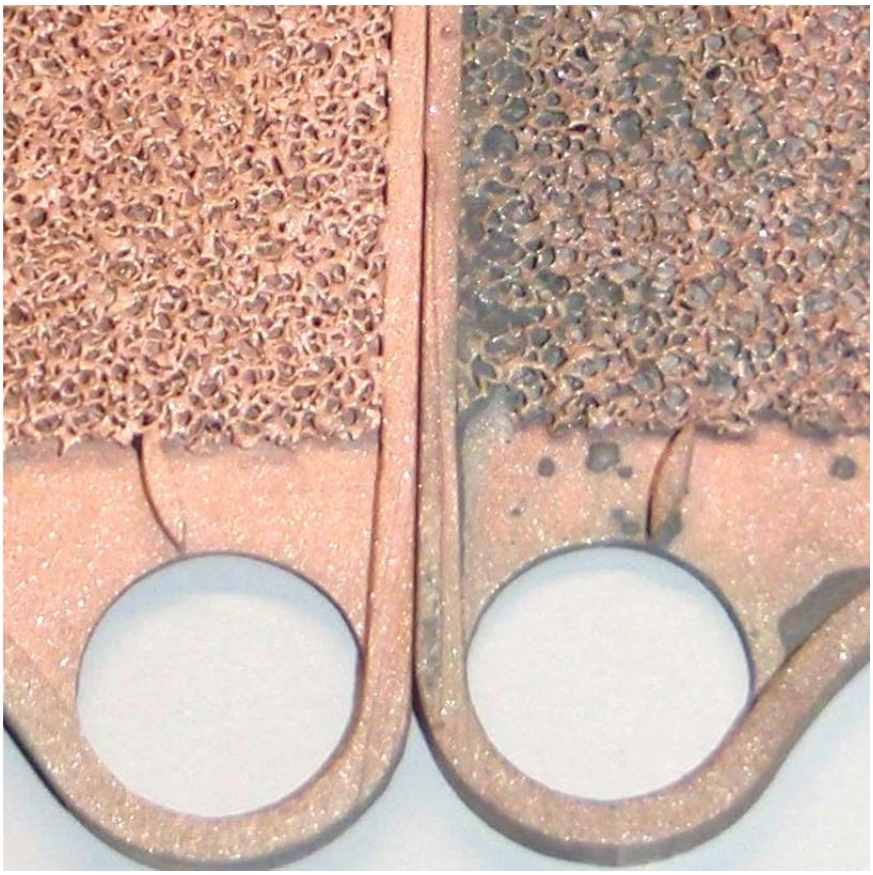

Figure 80: No Crush V1.0 (Left), No Crush V2.0 (Right), after cleaning

The compressed foams were all manufactured at the same time and using the same composition silver braze as No Crush V2.0. Initial inspection showed the 4x Crush V1.0 HX had minimal bonding near the openings. During disassembly the foam pieces in Figure 81 were easily removed as bonding was limited to their edges. Under closer inspection only a light coating of braze was found on the ligaments. The dark areas are believed to be contamination which hindered the foam's ability to effectively bond to the HX. The copper shim seen in Figure 82 had some bonding and was difficult to remove; this was the only HX which showed reasonable bonding to the copper shim.

Figure 81: 4X Crush V1.0 HX

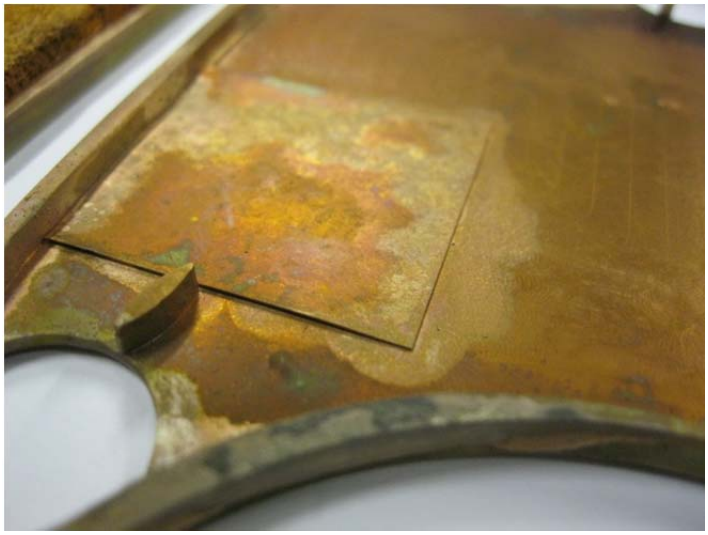

Figure 82: Copper shim in 4X Crush V1.0 HX

Prior to disassembly a loose piece of foam could be heard in the 4x Crush V2.0 HX. When the HX was cut in half the pieces of foam fell out due to zero bonding between the foam and HX. Figure 83 shows the HX cut in half, after the top face was machined down and peeled back to reveal the lack of bonding. The foam only appeared to hold a light coating of braze on the ligaments suggesting an insufficient amount of braze alloy was used, and a preference of the alloy to flow into the foam by capillary action rather than first bonding with the substrate.

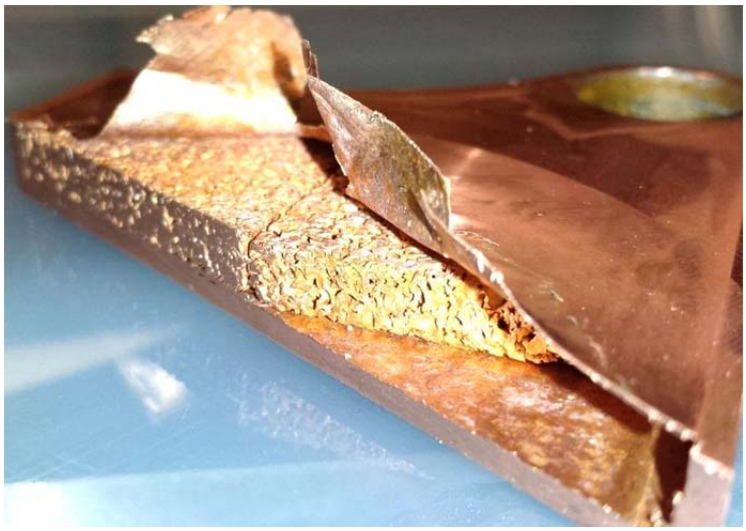

Figure 83: 4x Crush V2.0 foam HX

Vacuum furnace brazing the foam to the copper HX halves was more difficult than anticipated. Prior to testing there was no indication that the brazing had not done its job inside the HX. When each unit comes out of the oven the coverage and level of bonding is unknown without destructive disassembly. The first indication that the joint failed to establish properly was during testing when the experimental values didn't meet theoretical expectations. The second indication was the discovery of a loose piece of foam inside the 4x Crush V2.0 HX. The two types of silver braze were tested afterwards with the second exhibiting inferior capillary properties. Appropriate wicking of the silver is essential when brazing foam as it enables the alloy to reach the end of the ligaments in all positions (flowing against gravity), thereby thermally connecting them to the walls without creating blockages.

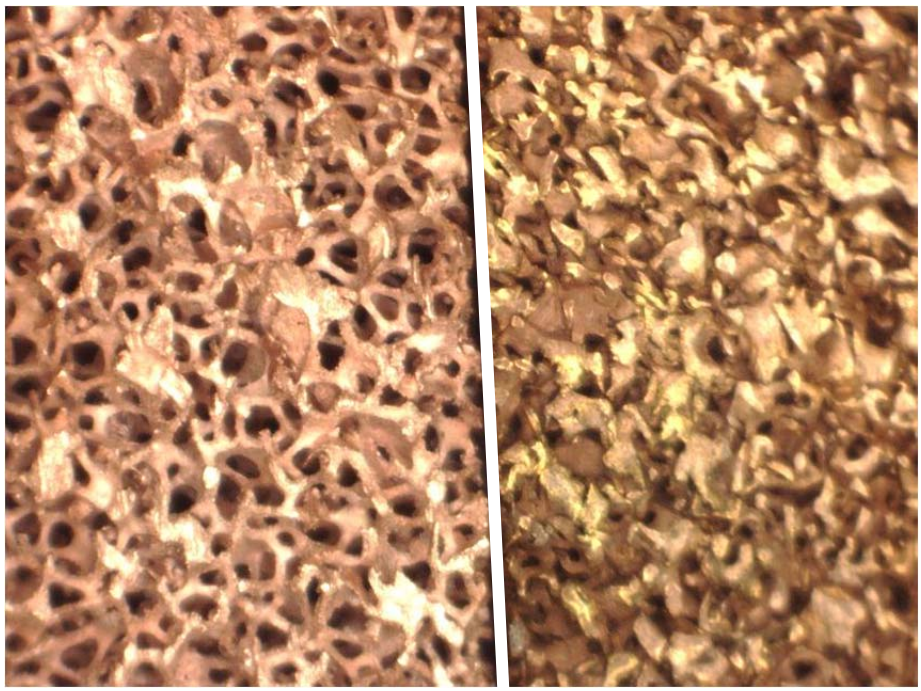

Figure 84: Virgin foam (left), 4x Crush V2.0 after brazing (right)

Microscopic analysis was performed to better comprehend the brazing issues. Inspection showed the silver alloy was first (preferentially) wicked into the foam micropores; insufficient alloy quantity thus prevented adherence to the HX surface. Figure 84 compares virgin uncrushed foam with 4x Crush V2.0 foam after brazing, the lighter colour of the 4x foam is the silver alloy coating the ligaments.

Examination of No Crush V2.0 revealed the soft solder blocking individual pores. Figure 85 is a close up of a pore 1.41 mm in diameter filled with soft solder, the needle positioned underneath afterwards indicates no bonding between the ligaments and HX surface.

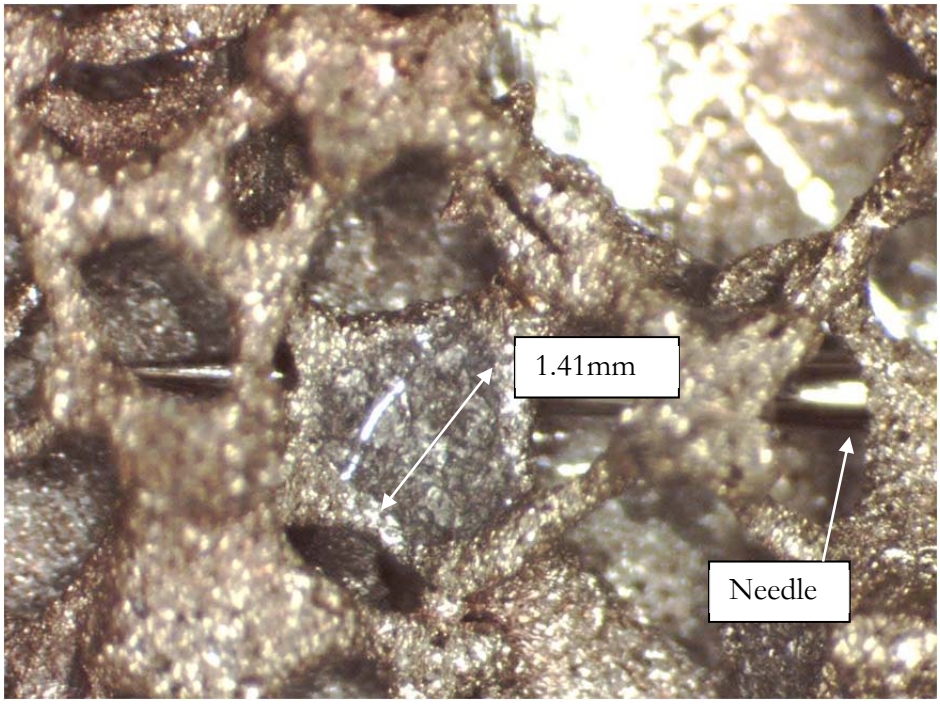

Figure 85: No Crush V2.0 (close up)

A problem area of No Crush V1.0 foam is shown in Figure 86, this 1/2" strip of foam was easily bent upwards to indicate a lack of bonding. The solder can be seen on the ligaments while the HX surface has no silver alloy present.

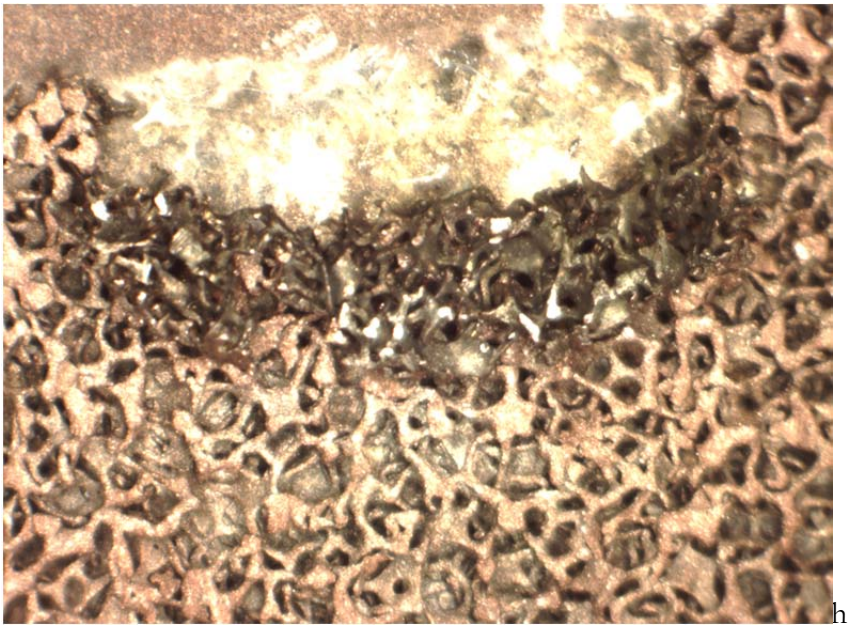
h

Figure 86: No Crush V1.0

A closer review of the virgin foam, Figure 87, showed the casting process leaves behind small pieces of silica and loose copper particles. These are believed to have had an adverse impact on the brazing process.

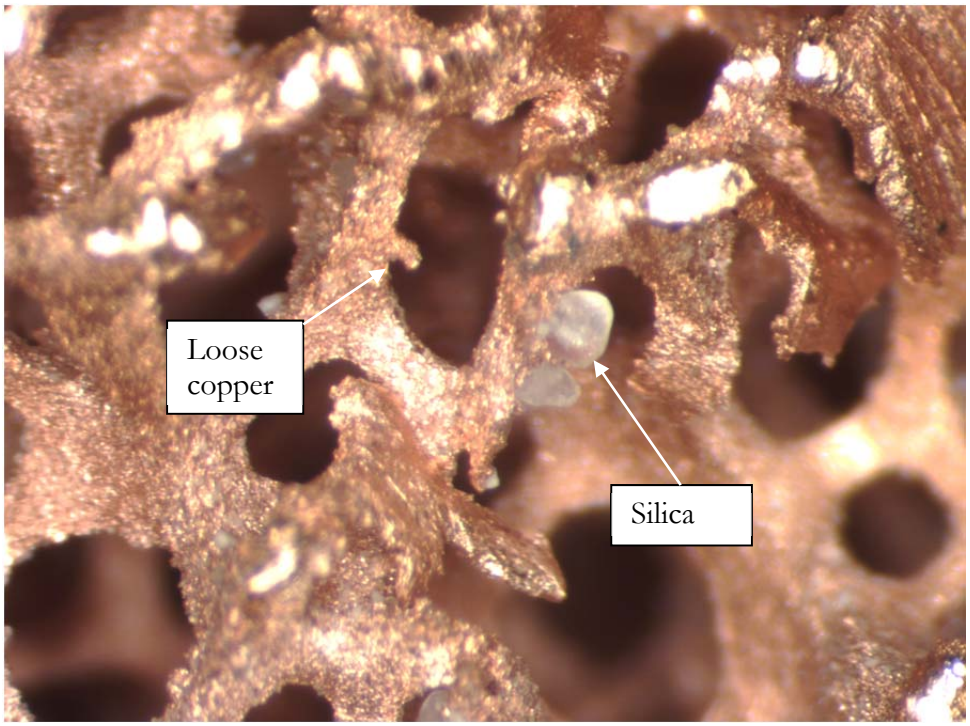

Figure 87: Contaminated Virgin foam

Another cause for poor results stems from how the foam was crushed. To better align the foam ligaments in the direction of heat flow it was decided to crush the foam in two dimensions (length and width). Doing so required assembling multiple pieces of crushed foam, to fill the HX cavity. Figure 81 shows these pieces outside the 4X Crush HX cavity. Brazing paste was applied between foam pieces in an attempt to fuse them, disassembly showed this did not work, likely due to insufficient quantity. The biaxial compression process also tended to increase the density of foam locally at the exterior surface. Joining these surfaces by brazing risks formation of blockages at those interfaces, so it is recommended to utilize one piece of foam fit into the HX cavity.

During biaxial compression the different 4x crush foam pieces expanded laterally, and were thus re-crushed in the Z-direction. To compensate for manufacturing tolerances, small shims were placed where necessary and silver alloy was applied to both sides of these prior to brazing. Figure 88 shows such a copper shim upon disassembly with only a small area of bonding, despite covering the entire face with brazing alloy paste. This suggests an insufficient amount of silver based alloy was used for the respective surface areas.

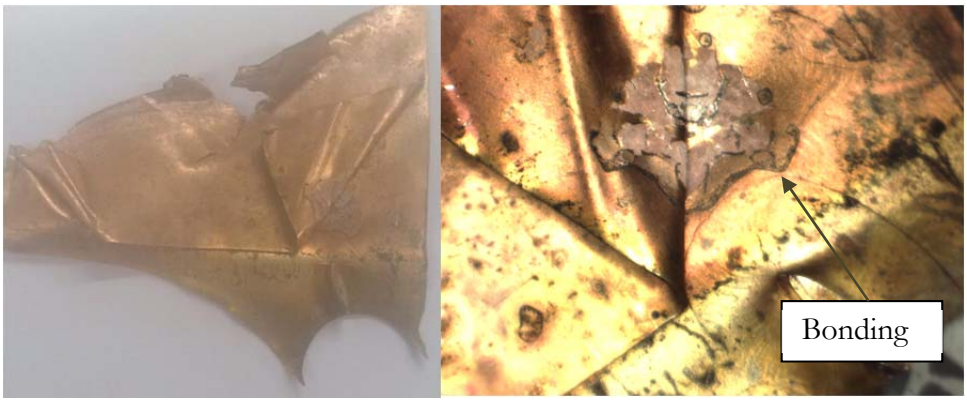

Figure 88: 4x Crush V2.0 Copper shims (left), Close up (right)

The foam samples were weighed to understand the variance in density that could be expected from the manufacturer. A sample size of 14 was taken for the 2.0" x 2.0" x 0.375" foam. The average density was found to be 12.2%, and standard deviation (σ) was 0.82% which corresponds to a ±6.7% difference in density at the ±1σ limits. The maximum percent difference was found to be 24% between the 14 samples examined. This variation is rather concerning as it impacts the consequent thermal performance and flow losses.

4.3. SUMMARY

The first set of tests outline the performance of the HX in conjunction with the TE module identified in Chapter 3 to provide the heat load. This was done to better understand the performance relationship between the TE module and the HX as an assembly. From the onset of testing it became apparent the HX's were not meeting expectations. Initially repeatability was an issue with the test method and set-up, and this warranted the redesign of the test bench. At this time the HX design was optimized to be scalable, closer to a production intent design, and exhibit better performance in terms of pumping losses. While gathering data using the redesigned bench, the brazing and compression methods used during manufacturing were shown to have had negative impacts on the HX performance. When results differed from expectations, a second test set-up was built without the TE module, inspired by research work completed by Boomsma et al. [**50**]. The results from both tests aligned and confirmed that the No Crush V1.0 foam was still the best HX design tested thus far, but later analysis indicated that much more work was needed to perfect the brazing process. Microscopic inspection indicated the metal foam ligaments wicked the silver alloy preferentially. In other cases

pores were blocked with soft solder, a lack of bonding between the foam and HX walls persisted, and contamination from the casting process coupled with insufficient amounts of silver alloy were hindering the bonding. To rectify these issues significantly more silver alloy should be used, but the correct fluidity is necessary to prevent blockages of the pores. The foam should also be free of contaminants, crushed in the correct manner and have minimal density variation.

While the somewhat arbitrary goal of h_{system} = 30,000 W/m^{2}K, determined by full TE system modeling was not met, the best HX developed was able to significantly outperform standard HX's on the market. Figure 89 overlays the results from the present thesis work along with those from Boomsma et al. [**50**], and the highest performance HX design available from Mikros Manufacturing [**57**] using chemically milled microchannels. The figure plots the thermal resistance of the No Crush V1.0 HX for pumping power input, and puts on par with the best. Through testing a system heat transfer coefficient (including contact resistance) was measured at 13,212 W/m^{2}K with 2 LPM flow at only 2.3 kPa ΔP. This is substantially better than a similar channelled plate HX where h ~ 4000 W/m^{2}K [**58**]. Based on system performance, the $h_{contact}$ values measured, in conjunction with a properly brazed crushed (densified) foam, the goal of a system h = 30,000 W/m^{2}K seems plausible for an allowable pressure increment of 10X.

It must be clearly emphasized that many researchers and vendors appear to claim far higher performance values. However on closer inspection it is revealed that one or a combination of the following factors skews results:

- Omission of contact resistance effects altogether
- Extreme pumping power (flow and pressure) are employed

- Values are quoted using heat pipe spreaders or enlarged surface areas
- Micro-fabrication technology is used which makes the design cost prohibitive
- Large temperature differences that involve phase changes of the working fluid.

In the present context, the aim of the work was to achieve the utmost heat transfer at ΔT's of only a few degrees across hard thermal interfaces in order to capitalize on the relatively attractive COP's of thermoelectric devices operating across ΔT's of approximately 20 °C, or less. Indications are that the goals set out are well within reach given refinement of the manufacturing processes employed.

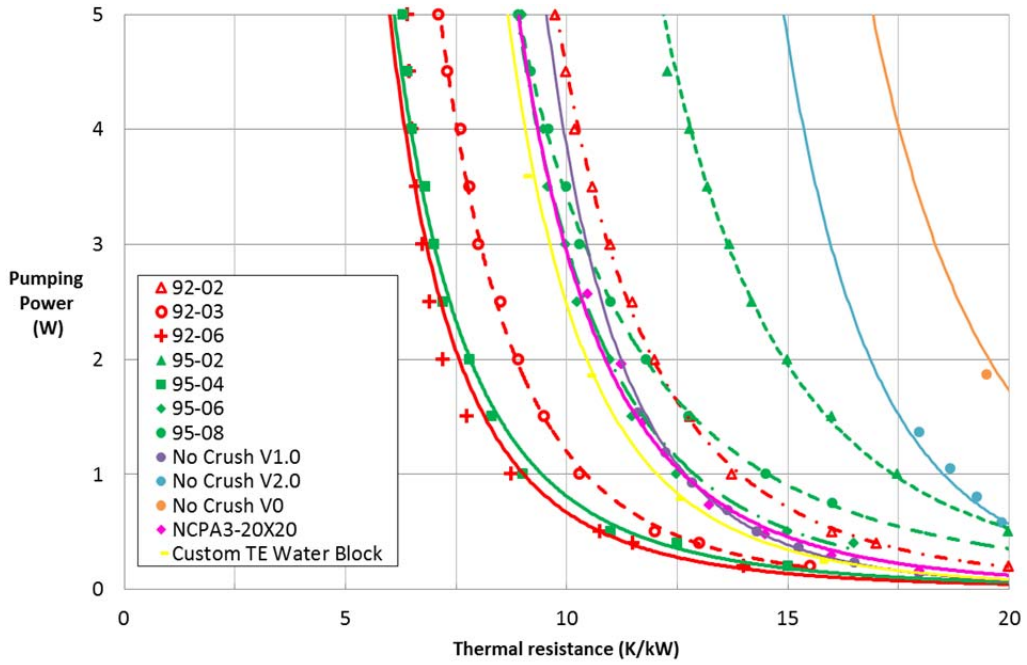

Figure 89: Thermal resistance vs. Pumping power

CHAPTER 5 – CONCLUSIONS AND RECOMMENDATIONS FOR FUTURE RESEARCH

5.1. OVERALL SUMMARY

This thesis reviews both TE and RMF technologies and their potential use together in the development of a high efficiency heat pump system. The background of these technologies was presented showing their presence in the aerospace, military and electronics industries. Use within the automotive industry is minimal but with improvements to efficiency their employ should see growth. With proper design they offer a potential robust, environmentally friendly, reliable alternative to conventional thermal management systems.

Initial testing was performed to benchmark TE modules from five different suppliers. Two tests were performed to compare module performance in a real world environment to the manufacturers' specifications. The Kyrotherm TE module was the only one able to substantiate the claims from its datasheet. The remaining modules lacked between 13 to 31% of the claimed ΔT_{max} value; with the Thermonamic modules failing during each test run. Kyrotherm's product was a clear winner and later used to evaluate the various HX designs developed.

The heat exchanger testing was done in three groupings, the first run analyzed the U and S-path metal foam HX's and base-lined a flat plate configuration. This work brought forth a large amount of experimental error that informed the redesign of the test bench. During this period the HX design was also developed into a more modular configuration that could be scaled and be adapted for use within the automotive application envisioned. Testing of the cross flow HX was first performed with the presence of a TE module as an

assembly. The results from this 2nd batch of experiments indicated that the compression of the foam showed little improvement on system performance. To verify these results the TE module was removed and the HX was tested independently in the final set of runs. They also confirmed that compressing the foam did not improve internal HX performance despite having achieved improved surface contact conductance.

In a post-mortem the HX's were dissected and viewed under a stereo-microscope, where it became clear that the brazing had not been successful. The No Crush V1.0 showed moderate bonding of the foam ligaments to HX surface. The remaining HX's showed no clear evidence of bonding, with braze alloy only lightly covering the foams ligaments. Despite the manufacturing difficulties, the performance level attained was commensurate with some of the best performing HX units known.

5.2. CONCLUSION

Thermoelectric devices continue to show promise as a heat pump technology gaining wider spread use in industry. The Kyrotherm module was able to maintain the specifications outlined on its' datasheet, and indications are that such units are quite capable of removing ~200 W across 20 °C ΔT at COP's above unity considering the system level. Independently, TE modules show promise for use within a high efficiency heat pump systems destined for various purposes for reasons of compactness, bi-directionality, longevity and silent operation.

While the HX design did not meet initial targets, the performance was still impressive despite set-backs due to poor brazing and inconsistences in the foam. The HX assembly was able to achieve a system heat transfer coefficient of 13,212 W/m^2K at 2.0 LPM flow

rate with only 2.3 kPa pressure drop; which is far better than a standard multi-pass flat plate design and ranks favourably against the competitive technology. It was shown that the addition of a RMF improves the thermal performance of the HX but the practical optimal extent is not yet quantified as experimental results were affected by poor brazing and multiple pieces of foam potentially affecting flow. Test bench redesign and complications during manufacturing prevented the full heat pump system from being tested. Prior calculations showed the HX assembly needed to be in the range of 20,000-30,000 W/m^2K for 20-30 kPa pressure drop @ 2 LPM in order to offer a competitive system COP and be commercially viable. Continued development focusing on brazing and correct size and type of metal foam insert is still believed to hold the possibility of meeting such a target with relative ease.

5.3. RECOMMENDATIONS FOR FUTURE RESEARCH

There are two fundamental areas that need to be examined to determine the overall viability of RMF's as a high efficiency HX. In this work the brazing proved to be a challenge and is the key reason the crushed foam didn't meet theoretical expectations. The relationship between the brazing parameters and HX performance utilizing a variety of brazing pastes and preparation / processing methods need to be further evaluated. In conjunction, a single piece of foam is desired over multiple crushed pieces within the flow cavity. This eliminates any voids, flow bypasses and interface blockages that can degrade performance. Secondly, optimizing the hard contact surface interface by selection of appropriate thermal pastes or employing bonding technique (example low melting solders) is equally crucial to meeting the overall performance objective.

APPENDICES

APPENDIX A: ELECTRICAL SCHEMATICS

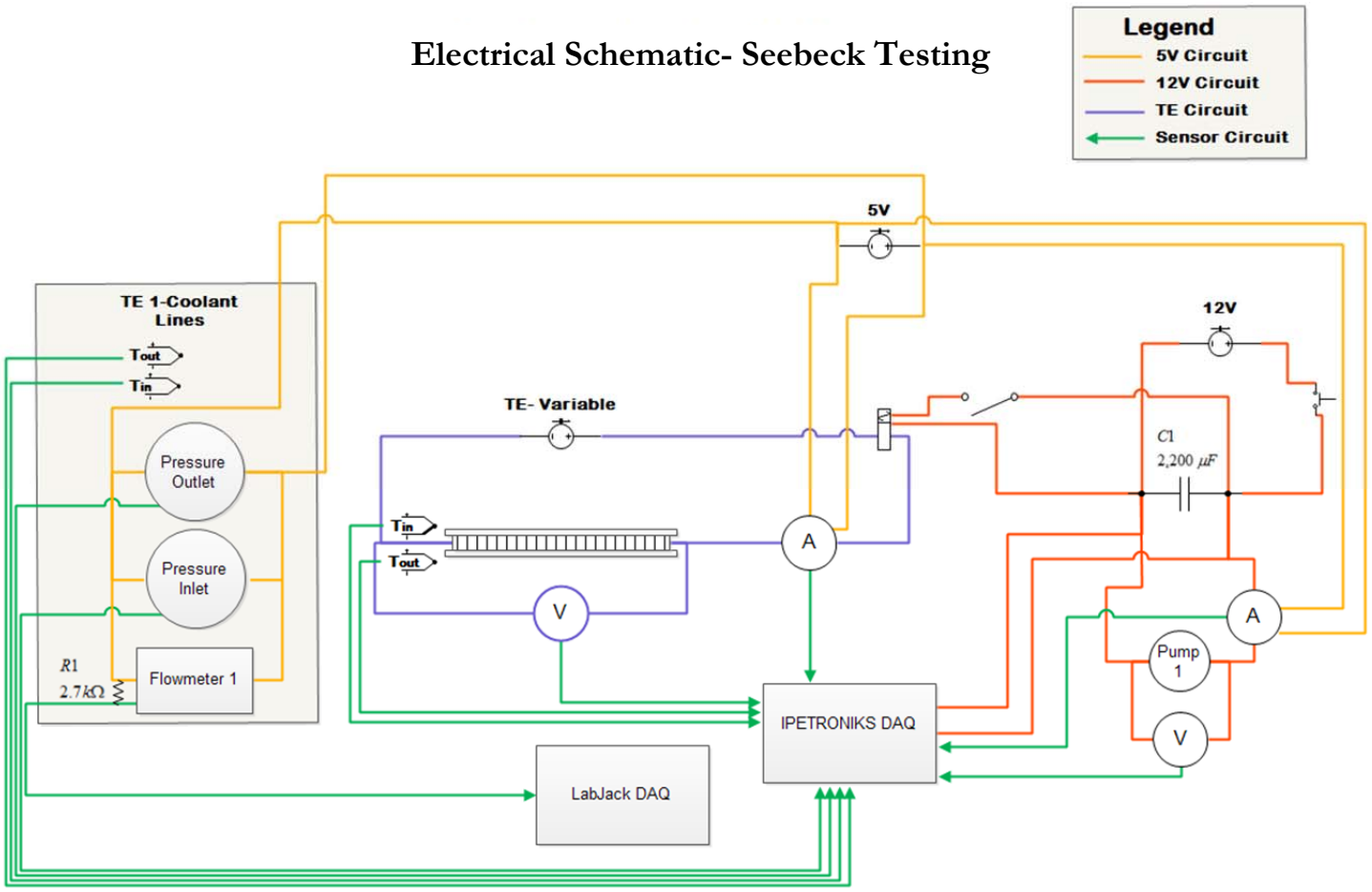

Electrical Schematic- TE Heater Test

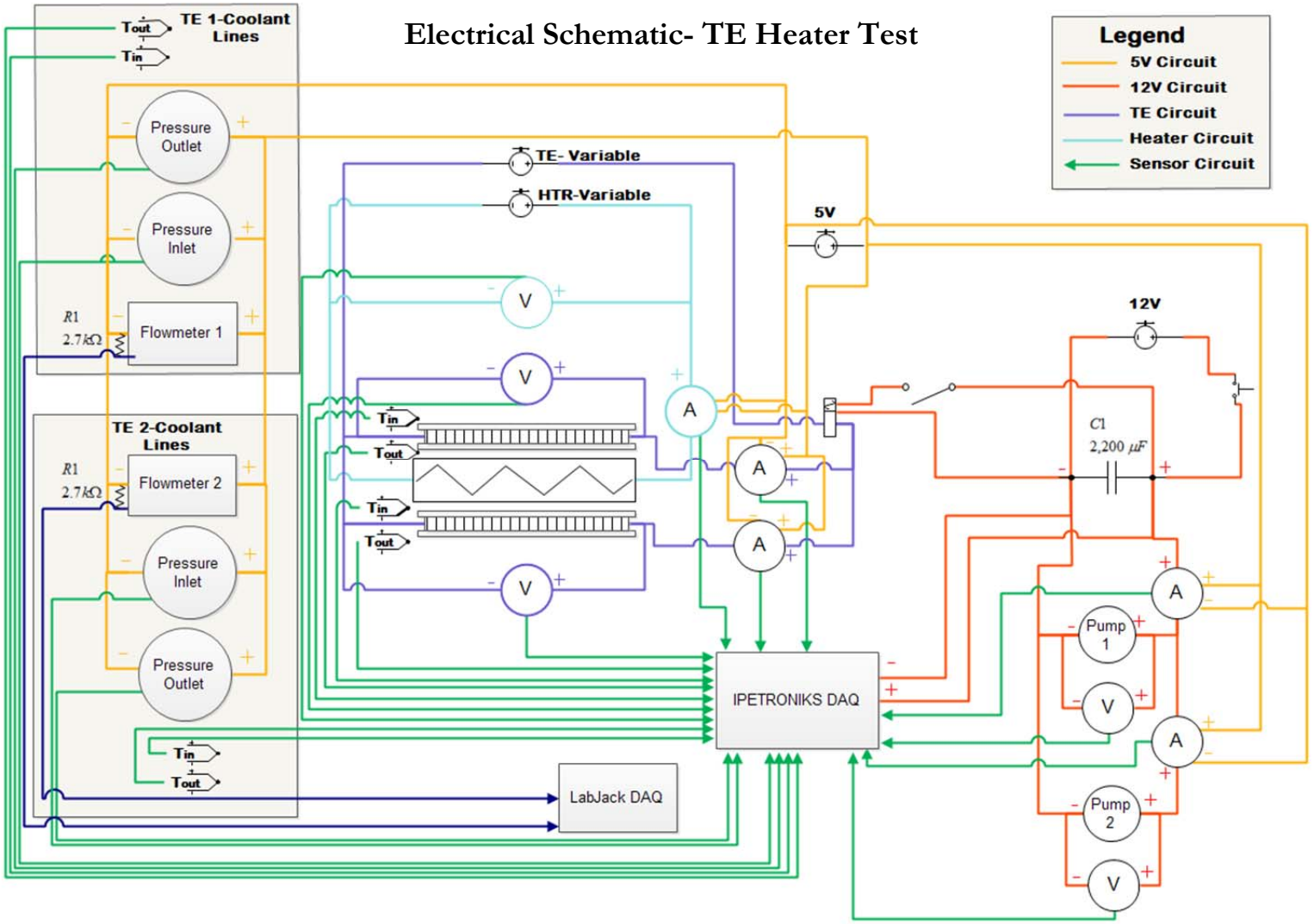

Electrical Schematic- HX Test 1

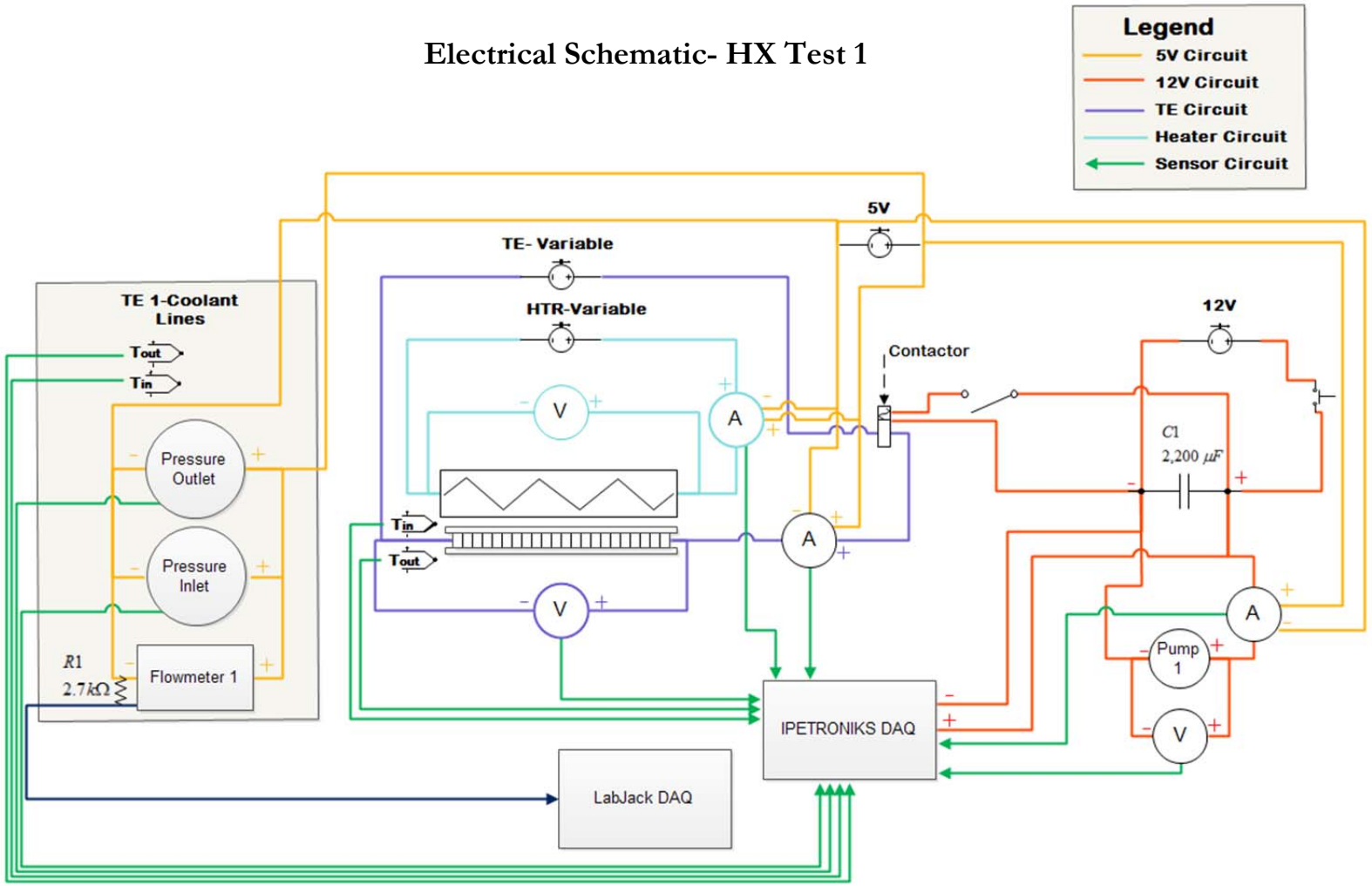

Electrical Schematic- HX Test 2

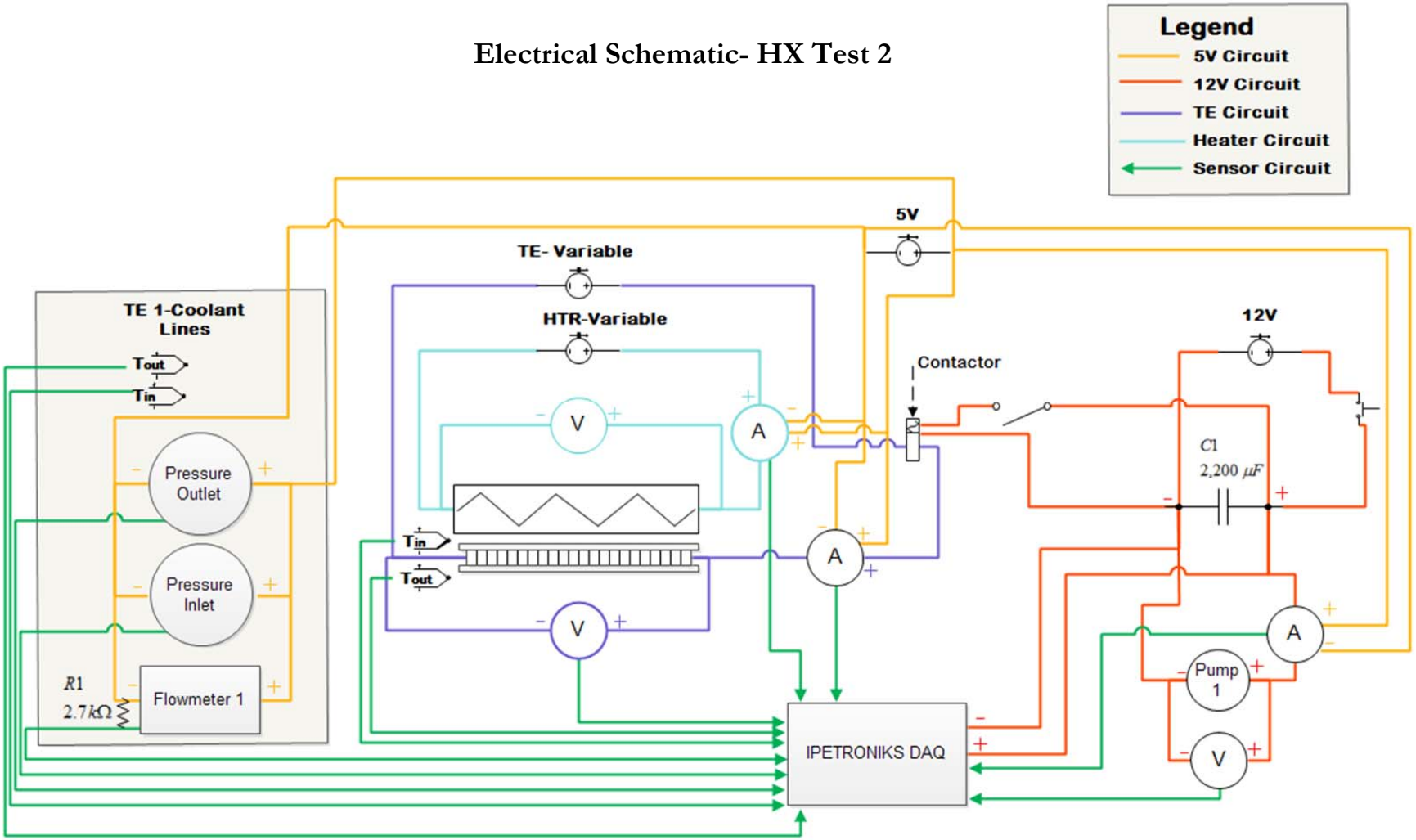

APPENDIX B: SEEBECK TESTING DATA

TE Tech

Iteration	Hot TE Face	Cold TE Face	Temp difference	Applied Voltage	Amperage	Seebeck Voltage(@2ms)	Seebeck Coefficient	Figure of Merit	Power	Cooling capacity
	T_h [°C]	T_c [°C]	ΔT [°C]	V [V]	I [A]	E [V]	α [V/K]	Z [1/K]	P [W]	Qc [W]
test 1 @50c	49.89	-9.90	59.79	18.50	7.48	2.44	0.041	1.24E-0.3	136.50	0.00
test 2 @50c	48.05	-13.39	61.45	16.00	6.72	2.70	0.044	n/a	113.48	-8.65
test 3 @50c	50.06	-14.44	64.50	14.04	5.80	2.65	0.041	n/a	86.51	-9.33
test 4 @50c	50.32	-13.57	63.89	12.01	4.81	2.53	0.040	n/a	61.09	-10.34
test 5 @50c	50.15	-9.64	59.79	10.04	3.90	2.28	0.038	n/a	40.95	-9.19
test 5 @50c	49.89	-3.70	53.59	8.02	2.98	2.15	0.040	n/a	25.18	-13.66
Test 1 @27C	27.02	-28.84	55.86	16.01	7.18	2.38	0.043	1.37E-0.3	114.94	0.00
Test 2 @27C	27.19	-30.15	57.34	14.04	6.34	2.25	0.039	n/a	90.60	2.70
test 3 @27C	27.11	-31.81	58.92	12.02	5.42	2.30	0.039	n/a	68.33	-0.86
test 4 @27C	27.19	-23.25	50.45	8.00	3.52	1.84	0.037	n/a	29.96	0.12

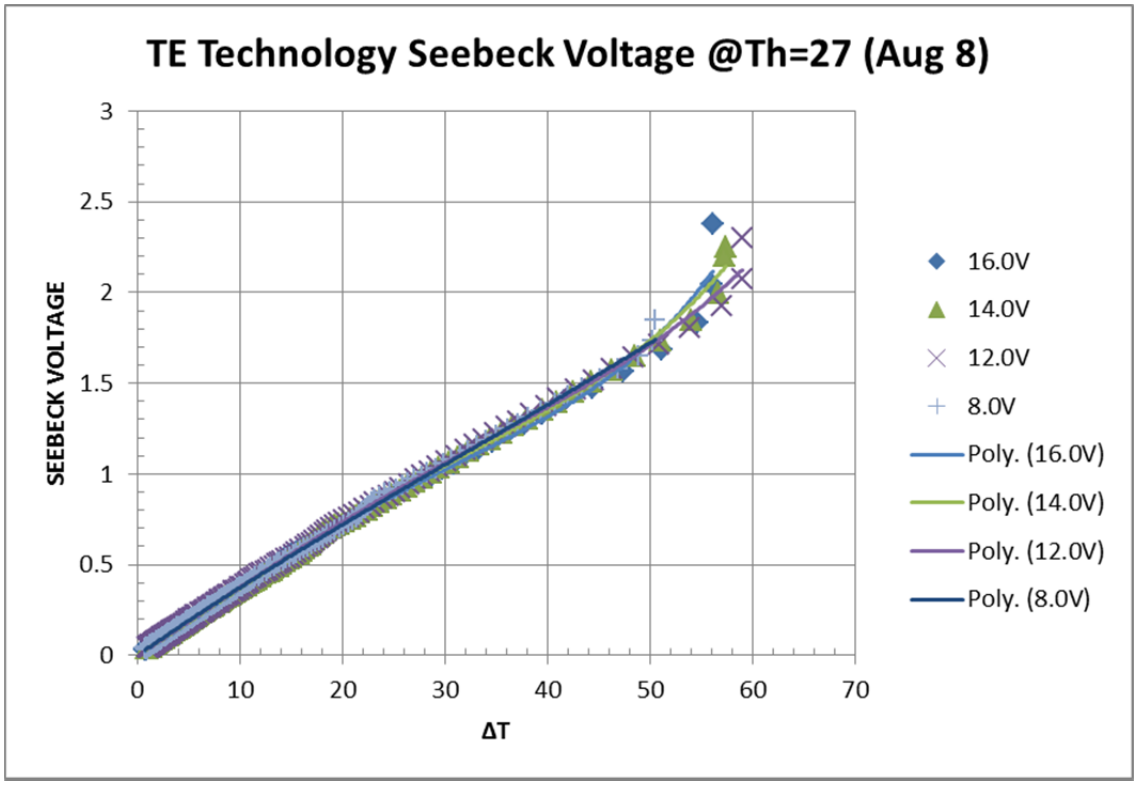
TE Technology Seebeck Voltage @Th=27 (Aug 8)
SEEBECK VOLTAGE
ΔT
0
0.5
1
1.5
2
2.5
3
0
10
20
30
40
50
60
70
16.0V
14.0V
12.0V
8.0V
Poly. (16.0V)
Poly. (14.0V)
Poly. (12.0V)
Poly. (8.0V)

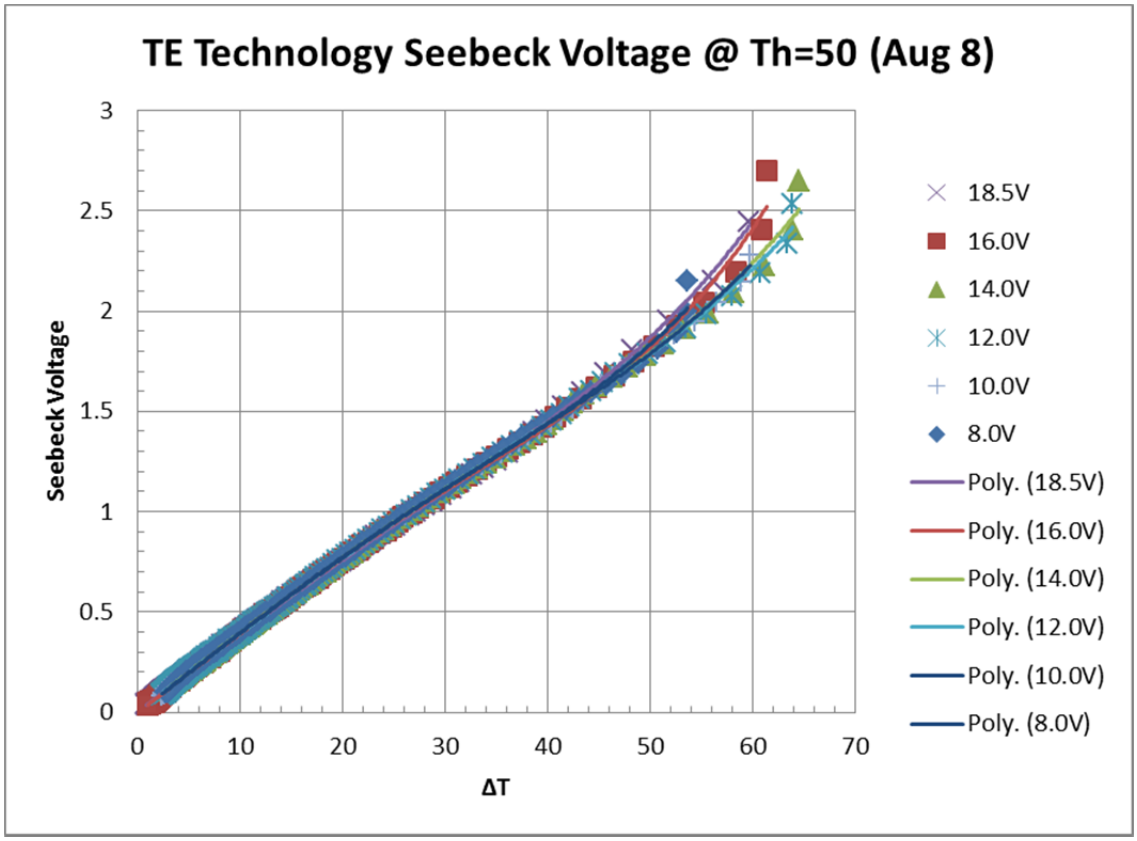
TE Technology Seebeck Voltage @ Th=50 (Aug 8)
Seebeck Voltage
ΔT
0
0.5
1
1.5
2
2.5
3
0
10
20
30
40
50
60
70
18.5V
16.0V
14.0V
12.0V
10.0V
8.0V
Poly. (18.5V)
Poly. (16.0V)
Poly. (14.0V)
Poly. (12.0V)
Poly. (10.0V)
Poly. (8.0V)

Custom TE Module

Iteration	Hot TE Face	Cold TE Face	Temp difference	Applied Voltage	Amperage	Seebeck Voltage(@2ms)	Seebeck Coefficient	Figure of Merit	Power	Cooling capacity
	T_h [°C]	T_c [°C]	ΔT [°C]	V [V]	I [A]	E [V]	α [V/K]	Z [1/K]	P [W]	Qc [W]
test 1 @50c	49.64	-14.93	64.56	32.04	13.49	8.22	0.127	3.10E-03	427.22	0.00
test 2 @50c	49.96	-14.46	64.42	30.00	12.73	8.59	0.133	n/a	390.96	-12.47
test 3 @50c	50.15	-11.75	61.90	25.02	10.59	7.12	0.115	n/a	270.44	25.77
test 4 @50c	49.43	-7.09	56.52	20.01	8.41	6.44	0.114	n/a	177.01	26.86
test 5 @50c	50.23	5.38	44.85	15.01	5.91	4.21	0.094	n/a	85.53	51.28
Test 1 @27C	27.07	-30.60	57.67	32.11	15.25	7.38	0.177	2.58E-03	489.51	0.00
Test 2 @27C	26.79	-31.20	58.00	30.01	14.42	6.01	0.180	n/a	423.90	53.97
test 3 @27C	26.86	-30.61	57.47	25.04	12.22	6.91	0.140	n/a	326.75	10.07
test 4 @27C	27.03	-26.43	53.47	19.99	9.27	4.41	0.144	n/a	180.32	74.25
test 5 @27C	27.18	-19.09	46.28	15.03	6.76	3.82	0.153	n/a	99.96	56.47
test 6 @27C	26.66	-12.90	39.56	12.00	5.37	3.42	0.129	n/a	65.17	43.32

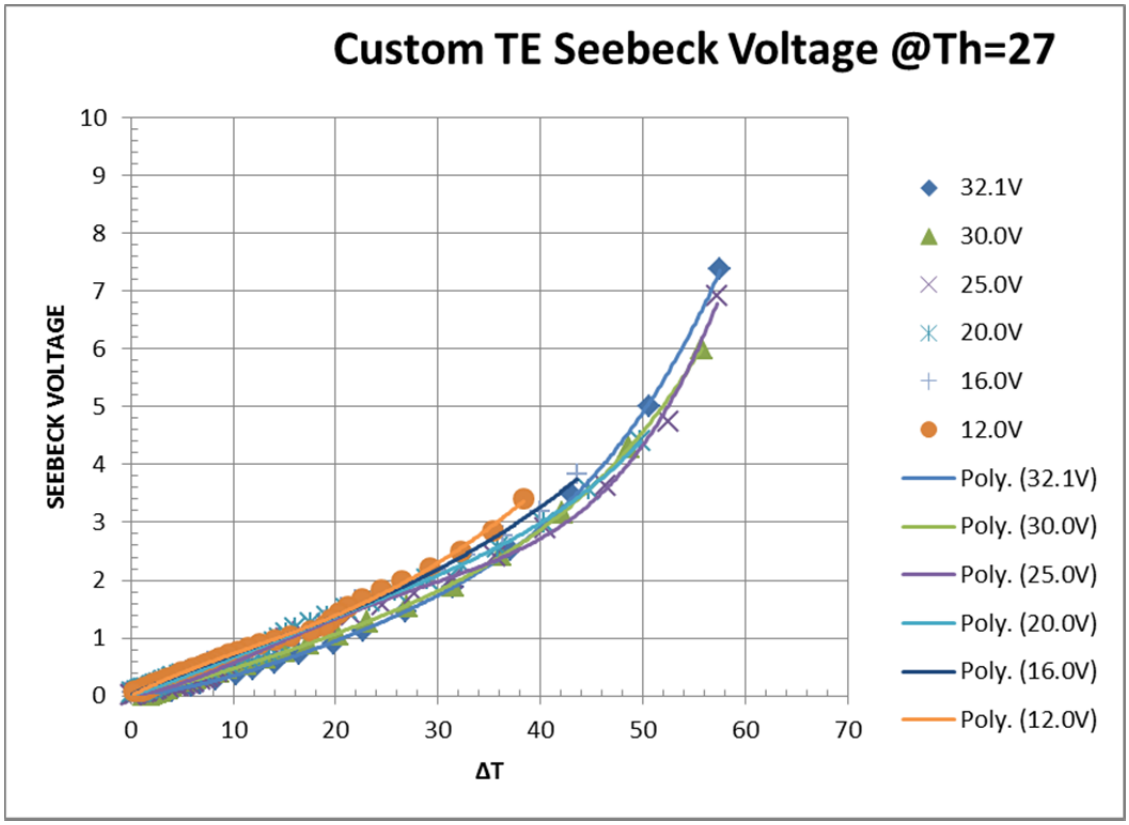
Custom TE Seebeck Voltage @Th=27
SEEBECK VOLTAGE
ΔT
0
1
2
3
4
5
6
7
8
9
10
0
10
20
30
40
50
60
70
32.1V
30.0V
25.0V
20.0V
16.0V
12.0V
Poly. (32.1V)
Poly. (30.0V)
Poly. (25.0V)
Poly. (20.0V)
Poly. (16.0V)
Poly. (12.0V)

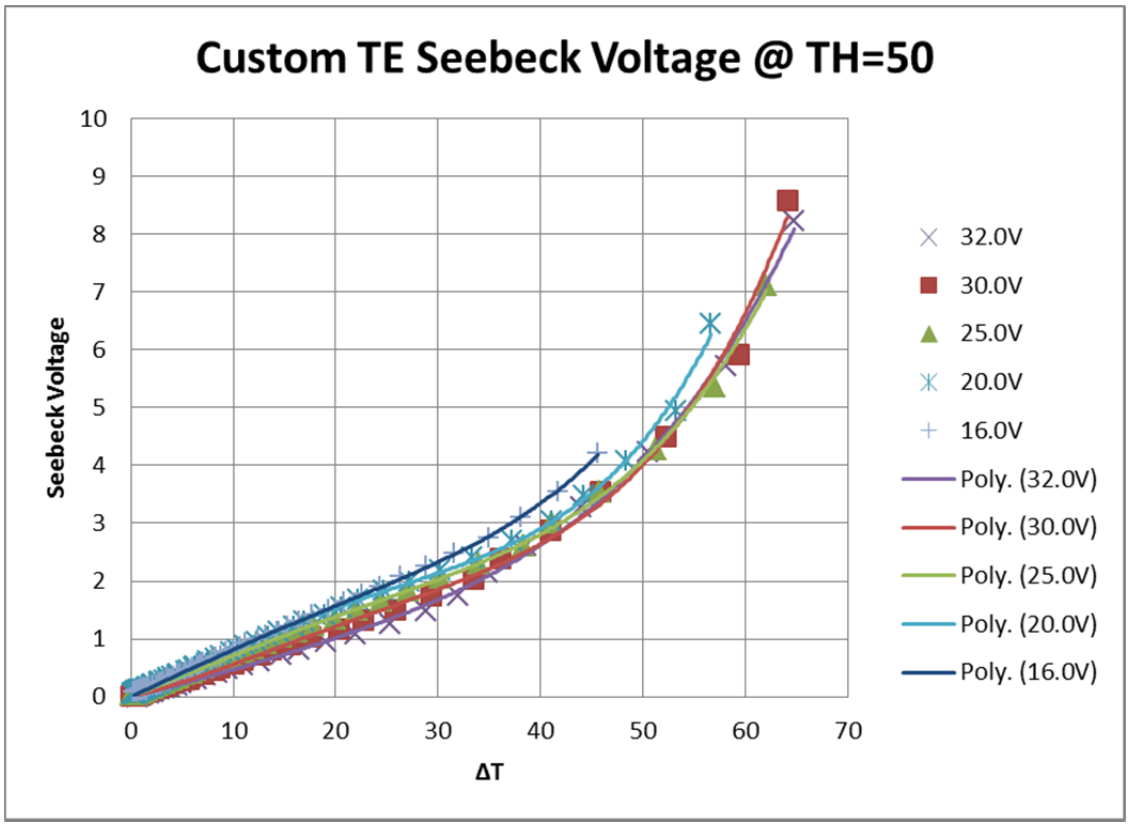
Custom TE Seebeck Voltage @ TH=50
Seebeck Voltage
ΔT
0
1
2
3
4
5
6
7
8
9
10
0
10
20
30
40
50
60
70
32.0V
30.0V
25.0V
20.0V
16.0V
Poly. (32.0V)
Poly. (30.0V)
Poly. (25.0V)
Poly. (20.0V)
Poly. (16.0V)

Crystal

Iteration	Hot TE Face	Cold TE Face	Temp difference	Applied Voltage	Amperage	Seebeck Voltage(@2ms)	Seebeck Coefficient	Figure of Merit	Power	Cooling capacity
	T_h [°C]	T_c [°C]	ΔT [°C]	V [V]	I [A]	E [V]	α [V/K]	Z [1/K]	P [W]	Qc [W]
test 1 @50c	50.41	-0.30	50.71	38.06	12.90	8.52	0.188	2.75E-03	477.94	0.00
test 2 @50c	50.15	-2.74	52.89	35.02	12.21	9.53	0.180	n/a	446.28	-35.48
test 3 @50c	50.06	-4.49	54.55	30.01	10.46	8.88	0.163	n/a	334.83	-18.85
test 4 @50c	49.97	-3.44	53.42	25.00	8.55	6.61	0.124	n/a	218.30	37.14
test 5 @50c	49.97	0.84	49.14	20.01	6.57	6.03	0.123	n/a	134.99	26.07
test 6 @50c	49.97	8.17	41.81	15.01	4.81	4.79	0.115	n/a	74.28	26.41
Test 1 @25C	25.10	-18.63	43.73	36.70	14.20	7.76	0.177	2.49E-03	514.68	0.00
Test 2 @25C	25.01	-20.46	45.47	34.93	13.66	8.20	0.180	n/a	486.80	-18.30
test 3 @25C	25.10	-23.25	48.35	29.97	11.83	6.77	0.140	n/a	361.14	31.96
test 4 @25C	25.10	-23.43	48.53	24.99	9.85	7.01	0.144	n/a	263.72	7.78
test 5 @25C	25.10	-20.72	45.82	20.04	7.64	5.12	0.153	n/a	156.11	7.78

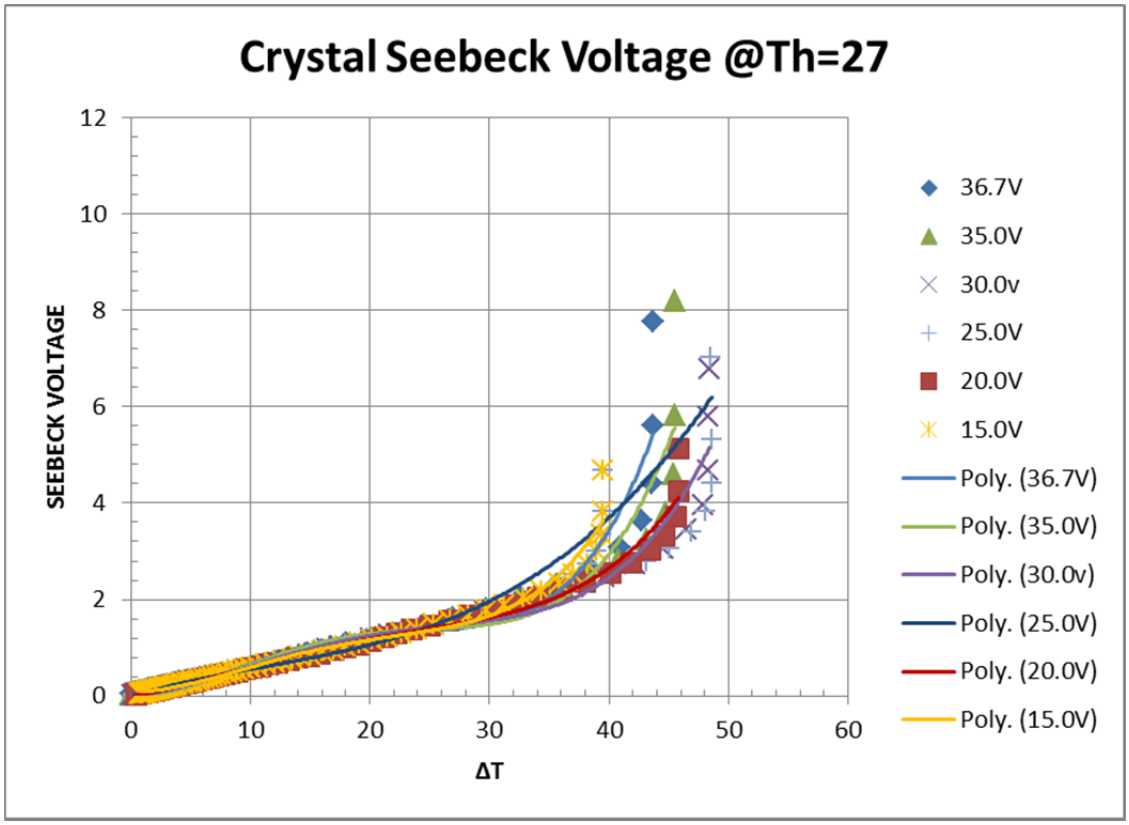
Crystal Seebeck Voltage @Th=27
SEEBECK VOLTAGE
ΔT
0
2
4
6
8
10
12
0
10
20
30
40
50
60
36.7V
35.0V
30.0v
25.0V
20.0V
15.0V
Poly. (36.7V)
Poly. (35.0V)
Poly. (30.0v)
Poly. (25.0V)
Poly. (20.0V)
Poly. (15.0V)

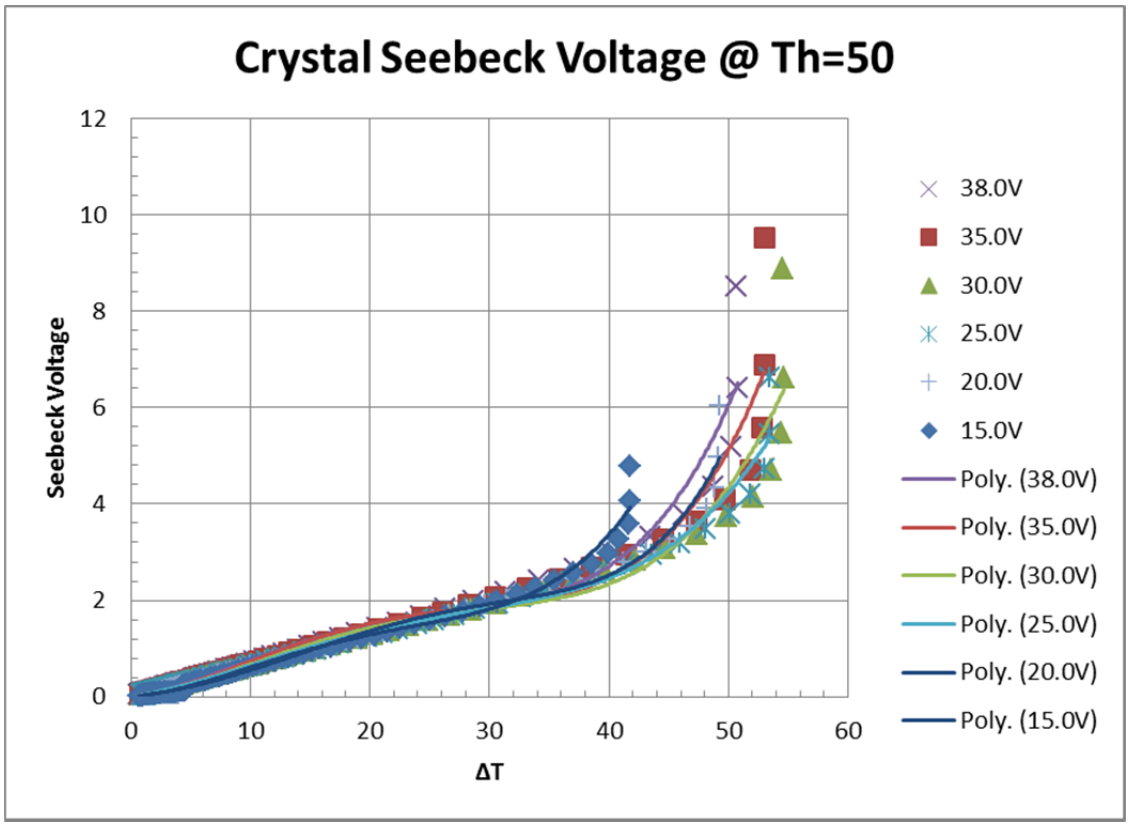
Crystal Seebeck Voltage @ Th=50
Seebeck Voltage
ΔT
0
2
4
6
8
10
12
0
10
20
30
40
50
60
38.0V
35.0V
30.0V
25.0V
20.0V
15.0V
Poly. (38.0V)
Poly. (35.0V)
Poly. (30.0V)
Poly. (25.0V)
Poly. (20.0V)
Poly. (15.0V)

Thermonamic

Iteration	Hot TE Face	Cold TE Face	Temp difference	Applied Voltage	Amperage	Seebeck Voltage(@2ms)	Seebeck Coefficient	Figure of Merit	Power	Cooling capacity
	T_h [°C]	T_c [°C]	ΔT [°C]	V [V]	I [A]	E [V]	α [V/K]	Z [1/K]	P [W]	Qc [W]
test 1 @50c	50.15	3.45	46.70	33.26	20.61	6.43	0.138	2.10E-03	673.20	0.00
test 2 @50c	50.59	0.84	49.75	30.09	18.93	6.37	0.128	n/a	576.81	1.76
test 3 @50c	50.24	-2.31	52.54	25.00	16.10	7.02	0.134	n/a	443.25	-47.80
test 4 @50c	50.06	-1.52	51.58	20.15	13.28	5.36	0.104	n/a	295.80	25.34
test 5 @50c	50.15	2.93	47.22	15.03	10.15	5.24	0.111	n/a	184.42	-7.56
test 5 @50c	49.97	13.05	36.92	10.06	6.34	3.23	0.087	n/a	71.63	25.36
Test 1 @27C	27.28	-16.01	43.29	29.50	20.68	6.09		2.18E-03	610.12	0.00
Test 2 @27C	27.11	-19.50	46.61	25.00	18.16	5.59	0.141	n/a	475.04	25.22
test 3 @27C	26.93	-20.55	47.48	20.00	15.26	5.18	0.120	n/a	342.79	33.59
test 4 @27C	27.02	-17.06	44.08	15.03	11.45	4.15	0.109	n/a	195.94	50.99
test 5 @27C	27.02	-8.42	35.44	10.00	7.33	3.13	0.094	n/a	83.78	38.34

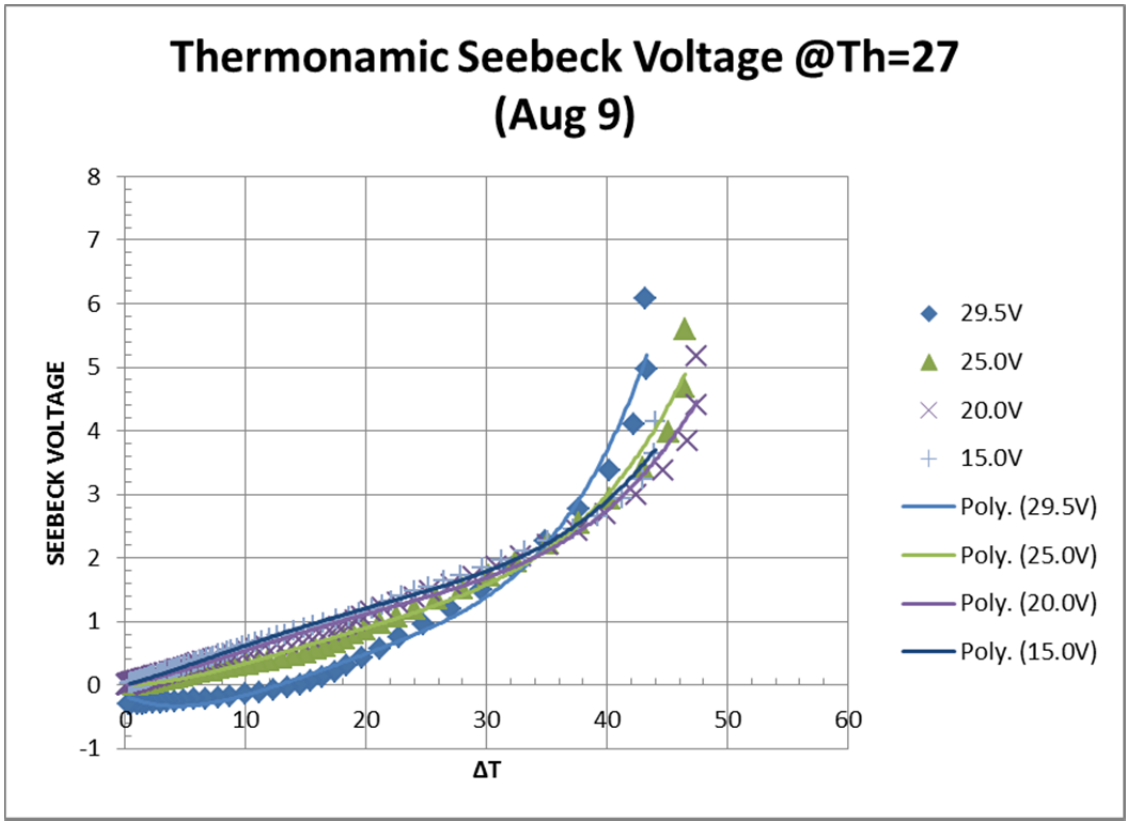
Thermonamic Seebeck Voltage @Th=27
(Aug 9)
SEEBECK VOLTAGE
ΔT
8
7
6
5
4
3
2
1
0
-1
0
10
20
30
40
50
60
29.5V
25.0V
20.0V
15.0V
Poly. (29.5V)
Poly. (25.0V)
Poly. (20.0V)
Poly. (15.0V)

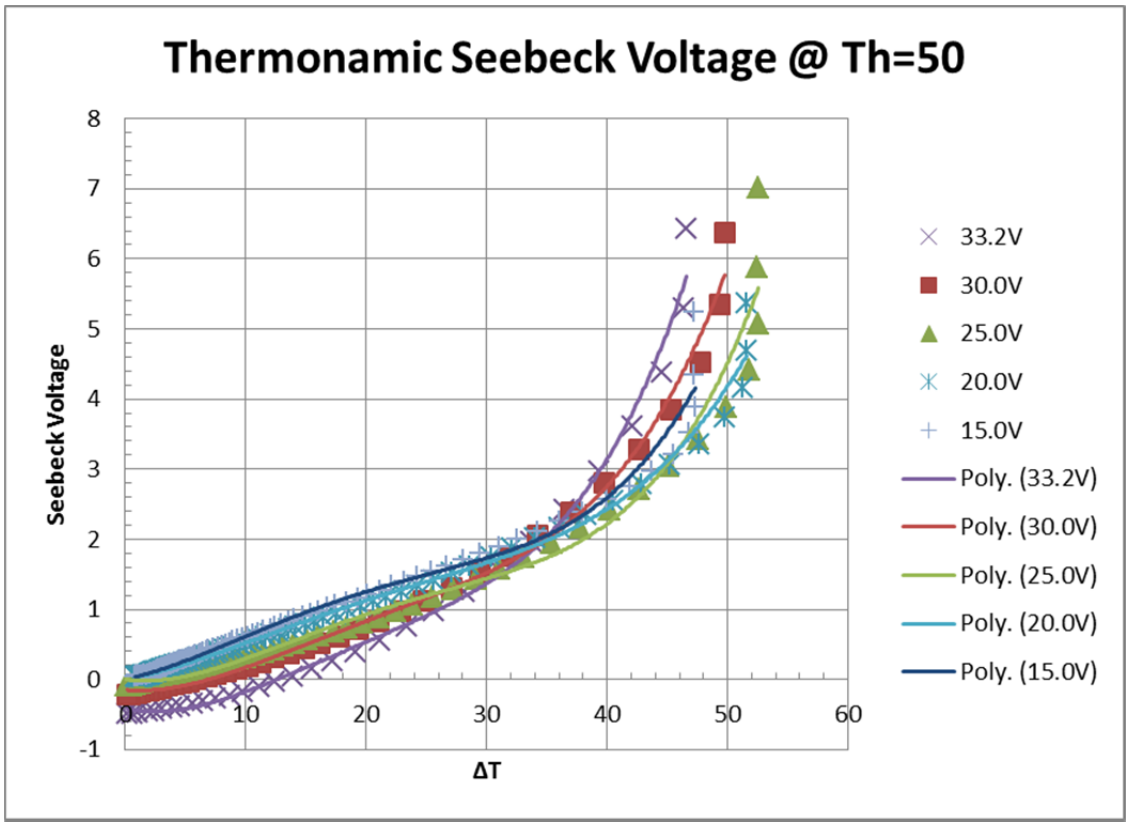
Thermonamic Seebeck Voltage @ Th=50
Seebeck Voltage
ΔT
8
7
6
5
4
3
2
1
0
-1
0
10
20
30
40
50
60
33.2V
30.0V
25.0V
20.0V
15.0V
Poly. (33.2V)
Poly. (30.0V)
Poly. (25.0V)
Poly. (20.0V)
Poly. (15.0V)

Kyrotherm

Iteration	Hot TE Face	Cold TE Face	Temp difference	Applied Voltage	Amperage	Seebeck Voltage(@2ms)	Seebeck Coefficient	Figure of Merit	Power	Cooling capacity
	T_h [°C]	T_c [°C]	ΔT [°C]	V [V]	I [A]	E [V]	α [V/K]	Z [1/K]	P [W]	Qc [W]
test 1 @50c	49.87	-28.69	78.56	26.48	22.47	5.16	0.066	2.52E-03	595.01	0.00
test 2 @50c	50.31	-23.15	73.46	24.24	19.56	6.27	0.085	n/a	457.67	22.43
test 3 @50c	50.28	-20.68	70.95	20.18	15.93	5.80	0.082	n/a	311.41	35.55
test 4 @50c	50.38	-16.05	66.43	18.14	13.89	5.22	0.079	n/a	235.34	57.58
test 5 @50c	50.33	-9.03	59.36	15.07	11.01	4.46	0.075	n/a	150.95	57.23
test 6 @50c	49.80	-0.95	50.75	12.02	8.17	3.81	0.075	n/a	90.05	23.45
Test 1 @27C	27.16	-42.02	69.17	22.60	20.83	5.28	0.076	2.71E-03	469.22	0.00
Test 2 @27C	27.22	-36.36	63.58	20.01	17.88	5.36	0.084	n/a	360.46	-7.46
test 3 @27C	27.00	-33.25	60.25	16.98	14.75	4.21	0.070	n/a	242.29	37.03
test 4 @27C	26.96	-31.41	58.37	15.01	12.72	3.94	0.067	n/a	183.94	35.70
test 5 @27C	27.08	-22.25	49.34	12.04	9.68	4.00	0.081	n/a	116.25	4.44
test 6 @27C	26.85	-16.18	43.03	10.00	7.82	3.36	0.078	n/a	76.82	10.48

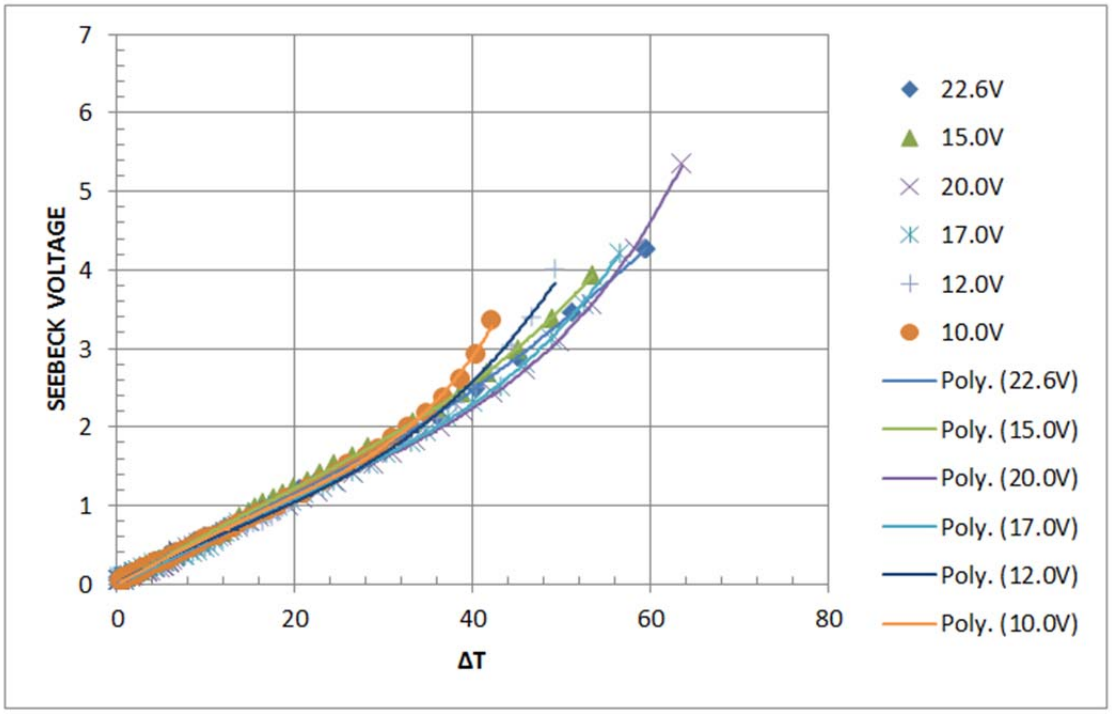
SEEBECK VOLTAGE
ΔT
0
1
2
3
4
5
6
7
0
20
40
60
80
22.6V
15.0V
20.0V
17.0V
12.0V
10.0V
Poly. (22.6V)
Poly. (15.0V)
Poly. (20.0V)
Poly. (17.0V)
Poly. (12.0V)
Poly. (10.0V)

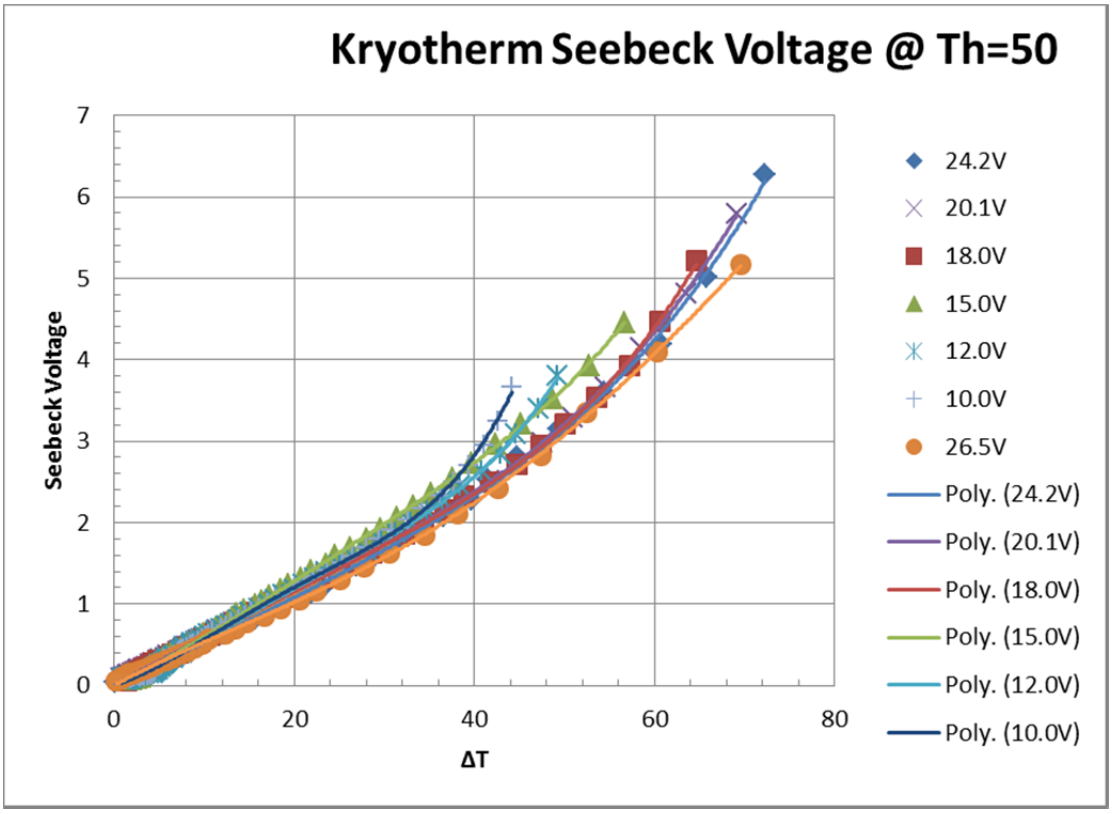
Kryotherm Seebeck Voltage @ Th=50
Seebeck Voltage
ΔT
0
1
2
3
4
5
6
7
0
20
40
60
80
24.2V
20.1V
18.0V
15.0V
12.0V
10.0V
26.5V
Poly. (24.2V)
Poly. (20.1V)
Poly. (18.0V)
Poly. (15.0V)
Poly. (12.0V)
Poly. (10.0V)

APPENDIX C: HEAT EXCHANGER TESTING DATA

Initial Test Bench Results

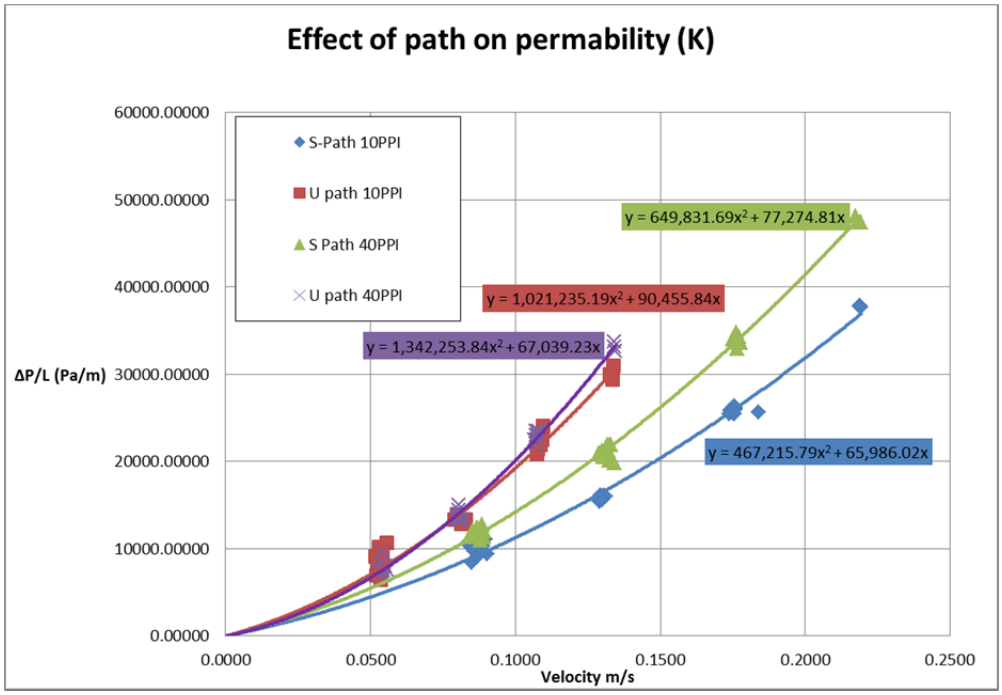

Figure 90: Flow path permeability

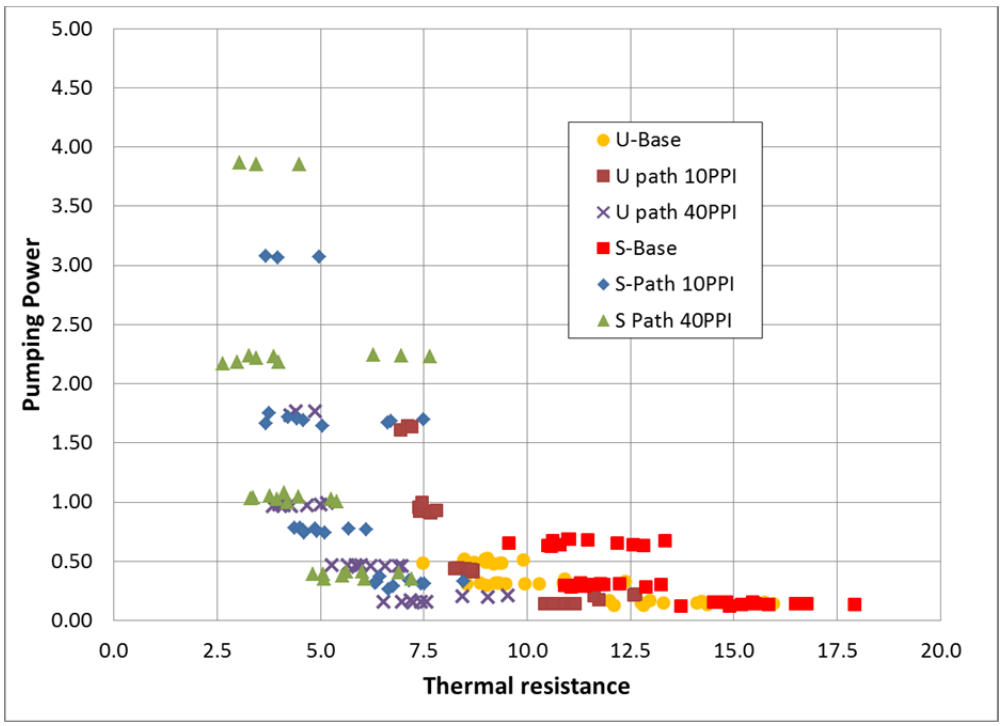

Figure 91: Initial testing - Pumping Power vs. Thermal resistance

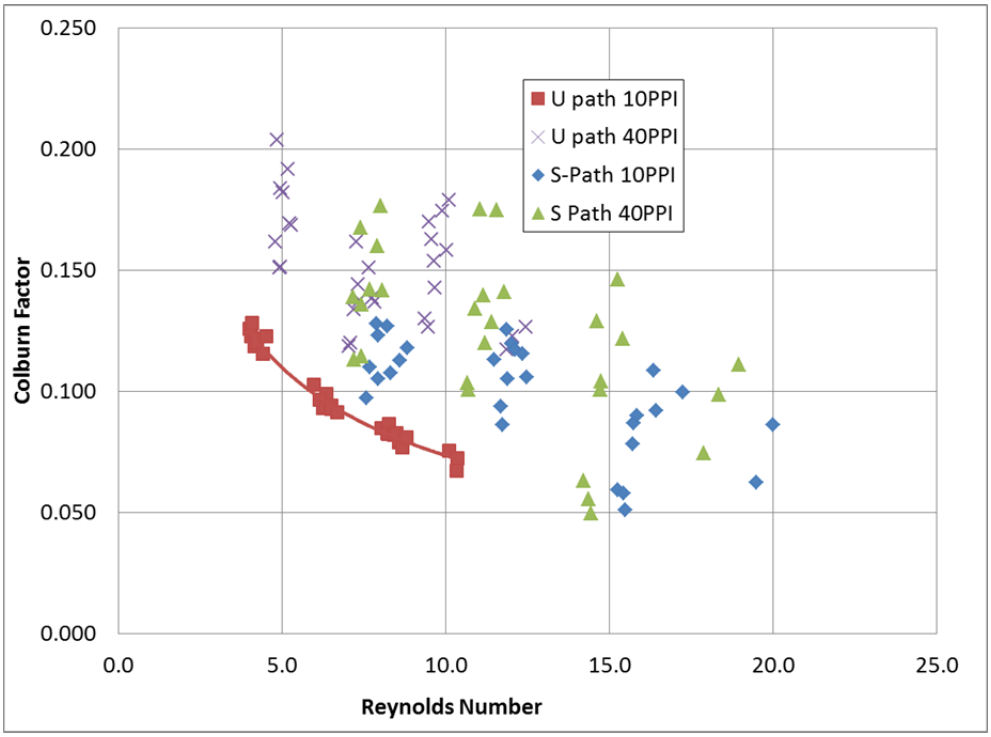

Figure 92: Initial testing - Colburn Factor vs. Reynolds Number

Heat exchanger Test #2 Results

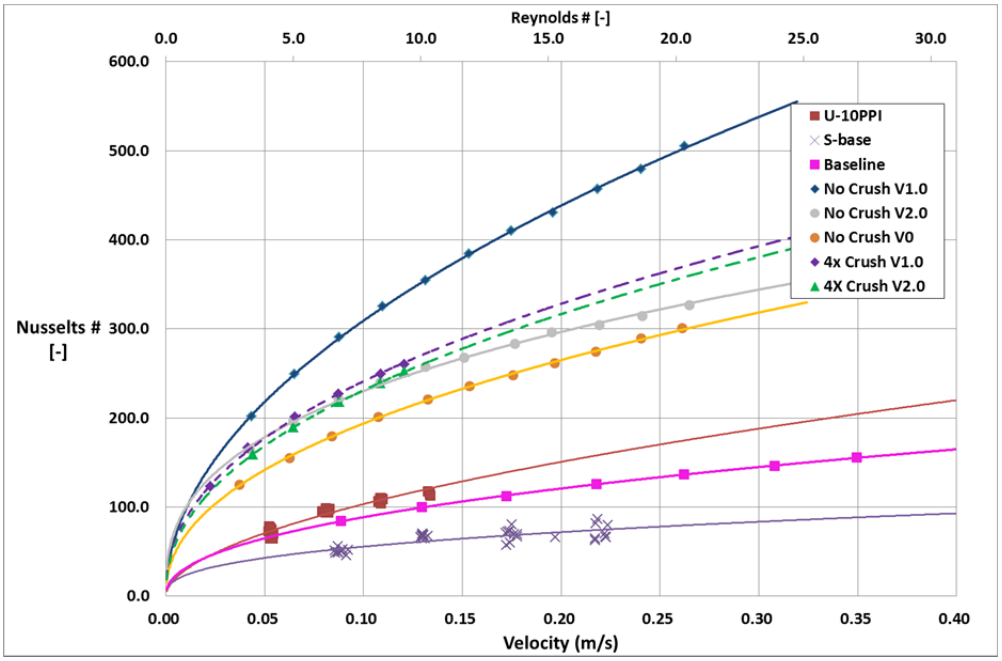

Figure 93: Heat Convection

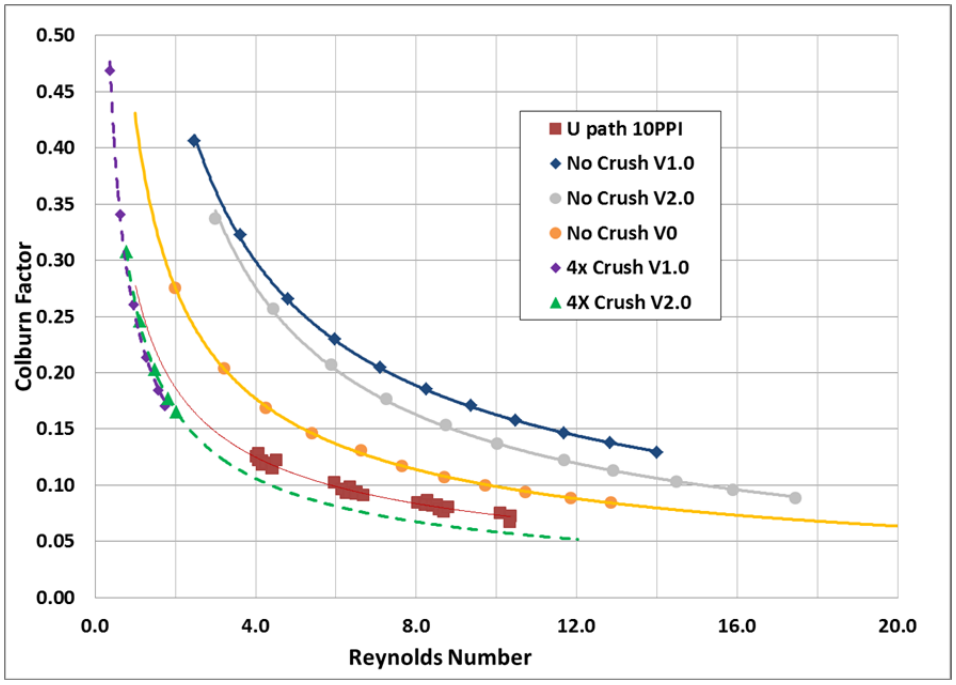

Figure 94: Colburn Factor Vs. Reynolds number

Table 32: Heat exchanger Test #1 Data

Flow rate	% I max	TE Current	HTR_Power	TE 1 Voltage	TE 1_Current	TE 1_Power (raw)	TE Power dissipation estimate with Seebeck	Pump_ Input Power (watts)	Δ Pressure (psi)	Log Mean Temperature of HX Fluid	ΔT- HX Fluid	HTR Temperature Inner (TE Face)	HX Wall Temperature Inner (TE Face)	Flow rate 1 (Main)	Flow Velocity (Main)	Flow rate 2 (Bypass)	Average face temperature on HX side of TE Module (Th)	Average face temperature on HTR side of TE Module (Tc)	ΔT- TE hot side (ceramic) to HX (copper)	ΔT- AVG Fluid temp vs. HX Wall against TE Module	ΔT- TE hot vs. LMTD fluid
LPM	%	A	W	V	A	W	W	W	psi	°C	°C	°C	°C	LPM	(m/s)	LPM	(°C)	°C	°C	°C	°C
Cross Flow Baseline- No Foam																					
Avg 100W	30.0	6.7413	100.83	11.38	9.04	110.06	86.94	12.08	0.01	41.12	2.25	41.65	55.36	1.50	0.0657	5.71	71.02	40.45	15.66	14.24	29.90
Avg 150W	50.0	11.2355	148.31	11.00	9.05	107.53	89.38	11.91	0.01	41.31	2.70	57.99	58.31	1.50	0.0657	5.69	76.41	56.22	18.10	17.00	35.10
Avg 200W	70.0	15.7297	199.41	9.20	8.30	83.37	74.84	11.99	0.01	40.87	2.90	78.47	59.74	1.50	0.0657	5.69	78.97	75.88	19.23	18.87	38.10
Cross Flow- No Crush V1.0																					
Avg 100W	30.0	6.7413	102.33	12.99	11.29	163.25	126.24	11.45	0.23	41.53	2.88	23.08	44.61	1.50	0.0658	5.34	52.44	21.26	7.83	3.08	10.90
Avg 150W	50.0	11.2355	150.44	12.57	11.33	159.73	129.73	11.44	0.23	41.91	3.33	37.03	45.52	1.51	0.0659	5.35	54.48	34.52	8.95	3.61	12.57
Avg 200W	70.0	15.7297	202.40	12.04	11.35	154.86	131.88	11.55	0.23	42.37	3.82	52.75	46.52	1.51	0.0662	5.35	56.74	49.53	10.21	4.15	14.36
Cross Flow- No Crush V2.0																					
Avg 100W	30.0	6.7413	101.16	13.16	11.30	165.91	129.08	12.16	0.18	41.68	2.95	24.73	46.84	1.48	0.0649	5.69	53.01	22.97	6.18	5.16	11.34
Avg 150W	50.0	11.2355	149.13	12.72	11.31	161.67	132.23	12.08	0.18	42.03	3.40	38.96	48.26	1.49	0.0651	5.70	55.08	36.61	6.82	6.23	13.05
Avg 200W	70.0	15.7297	200.22	12.21	11.32	156.87	134.47	12.03	0.18	42.32	3.92	54.70	49.74	1.49	0.0651	5.70	57.25	51.67	7.51	7.42	14.93
Cross Flow- No Crush V0																					
Avg 100W	30.0	6.7413	100.46	13.40	11.27	168.69	127.44	11.80	0.26	41.68	3.00	26.46	48.47	1.49	0.0652	5.62	60.08	25.50	11.61	6.79	18.40
Avg 150W	50.0	11.2355	146.49	12.98	11.28	165.03	131.57	11.70	0.25	42.03	3.51	41.47	50.07	1.50	0.0654	5.61	63.22	40.19	13.15	8.03	21.18
Avg 200W	70.0	15.7297	200.77	12.48	11.29	160.15	134.07	11.86	0.25	42.38	4.03	57.46	51.61	1.50	0.0655	5.63	66.39	55.85	14.78	9.23	24.01
Cross Flow- 4x Crush V1.0																					
Avg 100W	30.0	6.7413	103.80	13.27	11.30	166.90	129.58	15.51	3.02	41.79	2.97	23.96	45.95	1.51	0.0661	5.53	53.49	22.42	7.53	4.16	11.70
Avg 150W	50.0	11.2355	152.18	12.84	11.31	162.97	132.71	15.46	3.02	42.14	3.42	37.75	47.40	1.52	0.0665	5.54	55.52	35.70	8.13	5.25	13.38
Avg 200W	70.0	15.7297	203.91	12.31	11.33	157.73	134.88	15.43	3.00	42.43	3.95	53.44	48.91	1.52	0.0666	5.54	57.68	50.80	8.77	6.48	15.25
Cross Flow- 4x Crush V2.0																					
Avg 100W	30.0	6.7413	101.03	13.09	11.28	164.70	127.40	15.59	2.87	41.60	2.88	24.03	47.60	1.51	0.0660	4.91	53.44	22.60	5.84	6.00	11.84
Avg 150W	50.0	11.2355	149.08	12.61	11.28	160.09	130.27	15.61	2.86	41.97	3.33	38.56	48.99	1.52	0.0663	4.90	55.58	36.63	6.59	7.03	13.62
Avg 200W	70.0	15.7297	200.21	12.09	11.29	154.84	132.17	15.58	2.86	42.22	3.81	53.78	50.28	1.52	0.0666	4.93	57.67	51.34	7.39	8.06	15.45

Columns continued on next page

Flow rate	% I max	TE Current (A)	"h" - TE Module to HX (based on Fluid flow & ΔT)	"h"- HX internal fluid interface	ΔT- TE Cold side (ceramic) to HX (copper)	"h" - HTR to TE Module	Fluid ΔT & flow based Heat Flux (watts)	Reynolds Number	"h" Heat transfer coefficient (TE hot face to fluid)	$\Delta T (T_{pi}-T_{cinlet})$ ** USED FOR HEAT TRANSFER TERMS	Nusselt Number	Colbourn Factor	Thermal Resistance	System Pumping Power, Watts	Q Loss to environment
LPM	%	(A)	(W/m2 K)	(W/m2 K)	°C	(W/m2 K)	W	-	(W/m2 K)	°C	-	-	K/W	W	W
Cross Flow Baseline- No Foam															
Avg 100W	30.0	6.7413	3,856	3,179	1.19	28,002	120.8	29.456	2,021	15.35	73.19	0.060	0.086	0.0021	8.6
Avg 150W	50.0	11.2355	3,977	3,198	1.77	27,980	144.7	29.629	2,054	18.33	73.70	0.061	0.085	0.0016	22.6
Avg 200W	70.0	15.7297	4,100	3,182	2.59	26,300	137.0	29.496	2,081	20.30	73.08	0.062	0.086	0.0017	36.3
Cross Flow- No Crush V1.0															
Avg 100W	30.0	6.7413	9,649	18,814	1.82	18,571	230.6	3.456	6,954	4.50	324.39	0.207	0.020	0.0441	0.0
Avg 150W	50.0	11.2355	9,831	18,616	2.50	19,883	267.7	3.492	7,027	5.25	322.27	0.207	0.020	0.0438	14.5
Avg 200W	70.0	15.7297	10,007	18,695	3.22	20,776	309.5	3.545	7,127	6.03	323.48	0.207	0.020	0.0442	26.8
Cross Flow- No Crush V2.0															
Avg 100W	30.0	6.7413	12,431	11,174	1.76	19,054	233.2	4.224	6,761	6.61	218.31	0.205	0.029	0.0356	-1.0
Avg 150W	50.0	11.2355	13,182	10,693	2.34	21,084	270.2	4.270	6,830	7.90	210.79	0.205	0.030	0.0354	13.1
Avg 200W	70.0	15.7297	13,944	10,387	3.03	21,910	312.2	4.305	6,924	9.35	205.98	0.206	0.030	0.0350	24.5
Cross Flow- No Crush V0															
Avg 100W	30.0	6.7413	6,727	8,661	0.96	34,640	236.8	3.162	4,246	8.27	177.98	0.127	0.035	0.0501	-6.9
Avg 150W	50.0	11.2355	7,012	8,640	1.28	37,904	278.6	3.198	4,354	9.76	177.69	0.129	0.035	0.0491	1.4
Avg 200W	70.0	15.7297	7,175	8,643	1.61	41,988	319.8	3.227	4,418	11.21	177.67	0.130	0.035	0.0495	17.0
Cross Flow- 4x Crush V1.0															
Avg 100W	30.0	6.7413	10,420	14,334	1.55	22,276	239.7	0.933	6,731	5.63	266.16	0.198	0.024	0.5748	-3.8
Avg 150W	50.0	11.2355	11,311	13,047	2.05	24,547	277.4	0.948	6,837	6.93	247.84	0.199	0.025	0.5776	10.0
Avg 200W	70.0	15.7297	12,234	12,260	2.64	25,593	321.4	0.956	6,974	8.42	236.21	0.201	0.027	0.5773	20.0
Cross Flow- 4x Crush V2.0															
Avg 100W	30.0	6.7413	13,205	9,584	1.42	23,529	232.2	1.074	6,485	7.42	193.80	0.191	0.032	0.5465	-0.9
Avg 150W	50.0	11.2355	13,724	9,564	1.93	25,548	271.2	1.090	6,599	8.67	193.65	0.192	0.032	0.5486	10.9
Avg 200W	70.0	15.7297	14,081	9,619	2.45	27,142	311.2	1.100	6,700	9.93	194.78	0.193	0.032	0.5497	24.0

Table 33: Heat exchanger test #2 Data

Flow rate 1 (Main)	HTR Power	Δ Pressure	ΔT- Fluid	HX Fluid LMTD	HTR Wall Temp	HX Wall Temp	Heat into coolant (Qh)	ΔT From Heater to HX	Pumping Power	"$h_{contact}$" HX to Heater interface Input Q	HX, "$h_{convective}$" based on input Q	"h", System, based on input Q	"h", System, based on exit Q
LPM	W	psi	°C	°C	°C	°C	W	°C	W	W/m^2K	W/m^2K	W/m^2K	W/m^2K
Baseline													
8.0	881	0.50	1.7	41.6	74.5	71.4	811	3.1	0.46	58,971	7,338	6,649	6,118
7.0	882	0.38	1.9	41.8	76.5	73.3	808	3.2	0.31	57,301	6,941	6,304	5,780
6.0	881	0.27	2.2	41.9	79.0	75.6	810	3.4	0.19	53,493	6,490	5,894	5,421
5.0	881	0.19	2.7	42.1	82.0	78.4	806	3.6	0.11	50,335	6,010	5,466	5,000
3.9	879	0.11	3.3	42.4	86.3	82.4	798	3.9	0.05	46,646	5,450	4,966	4,507
3.0	880	0.04	4.5	42.9	92.0	87.8	802	4.2	0.01	43,188	4,861	4,444	4,049
2.0	879	0.01	6.6	44.0	101.3	96.8	806	4.6	0.00	39,899	4,134	3,805	3,487
No Crush V0													
6.0	879	2.72	2.3	42.0	60.1	56.9	819	3.2	1.86	55,977	14,693	12,056	11,225
5.5	877	2.35	2.5	42.1	60.7	57.5	818	3.3	1.49	55,230	14,153	11,662	10,878
5.0	879	1.97	2.7	42.2	61.6	58.2	812	3.4	1.12	53,421	13,600	11,220	10,366
4.5	878	1.66	3.0	42.3	62.4	59.0	810	3.4	0.86	52,857	13,040	10,816	9,988
4.0	879	1.37	3.3	42.6	63.5	60.0	807	3.5	0.63	51,995	12,490	10,406	9,551
3.5	871	1.10	3.8	42.9	64.5	61.2	812	3.2	0.44	55,594	11,796	10,023	9,342
3.0	890	0.85	4.4	43.2	65.9	62.6	815	3.3	0.30	56,079	11,355	9,715	8,894
2.5	880	0.58	5.5	43.7	68.2	64.7	817	3.5	0.16	52,247	10,363	8,893	8,260
1.9	870	0.37	7.0	44.4	71.1	67.5	816	3.6	0.08	50,675	9,335	8,092	7,587
1.4	886	0.22	9.4	45.5	75.0	71.6	815	3.4	0.04	53,234	8,406	7,428	6,840
0.9	890	0.07	16.2	48.5	83.5	79.9	846	3.5	0.01	52,267	7,020	6,313	6,004
No Crush V1.0													
6.0	883	2.23	2.3	41.9	53.7	50.3	825	3.4	1.54	53,707	25,844	18,446	17,248
5.5	884	1.88	2.4	41.9	54.1	50.7	814	3.4	1.19	53,854	25,057	18,055	16,618
5.0	881	1.61	2.7	42.0	54.5	51.1	813	3.4	0.93	53,544	23,996	17,470	16,116
4.5	883	1.34	3.0	42.1	55.0	51.7	808	3.4	0.69	53,859	22,937	16,928	15,493
4.0	885	1.09	3.4	42.3	55.6	52.2	815	3.4	0.50	53,818	21,968	16,391	15,080
3.5	885	0.90	3.8	42.7	56.6	53.2	815	3.4	0.36	53,991	20,808	15,749	14,517
3.0	883	0.68	4.5	43.0	57.6	54.3	814	3.4	0.23	53,955	19,465	14,965	13,802
2.5	881	0.49	5.4	43.4	58.8	55.4	818	3.4	0.14	53,871	18,107	14,144	13,129
2.0	881	0.33	6.8	44.1	60.6	57.3	821	3.3	0.08	54,479	16,558	13,212	12,317
1.5	884	0.19	9.1	45.1	63.2	59.9	821	3.2	0.03	56,339	14,816	12,152	11,288
1.0	881	0.08	13.8	47.2	67.9	64.7	836	3.2	0.01	56,816	12,544	10,594	10,051

Rows continued on next page

Flow rate 1 (Main)	HTR Power	Δ Pressure	ΔT- Fluid	HX Fluid LMTD	HTR Wall Temp	HX Wall Temp	Heat into coolant (Qh)	ΔT From Heater to HX	Pumping Power	"$h_{contact}$" HX to Heater interface Input Q	HX, "$h_{convective}$" based on input Q	"h", System, based on input Q	"h", System, based on exit Q
LPM	W	psi	°C	°C	°C	°C	W	°C	W	W/m^{2}K	W/m^{2}K	W/m^{2}K	W/m^{2}K
No Crush V2.0													
6.1	885	1.96	2.2	41.8	59.0	55.6	825	3.4	1.36	53,587	16,008	12,817	11,948
5.5	885	1.65	2.4	41.9	59.4	56.0	817	3.4	1.05	54,091	15,624	12,592	11,627
5.0	885	1.39	2.7	42.0	59.8	56.4	816	3.3	0.80	54,968	15,234	12,375	11,411
4.5	885	1.12	3.0	42.1	60.3	57.0	823	3.3	0.57	55,167	14,806	12,100	11,251
4.0	883	0.94	3.3	42.2	60.7	57.4	810	3.3	0.44	55,038	14,447	11,854	10,874
3.5	881	0.70	3.9	42.4	61.6	58.3	811	3.3	0.28	55,110	13,806	11,421	10,504
3.0	884	0.54	4.5	42.7	62.4	59.1	819	3.2	0.19	56,591	13,343	11,152	10,335
2.5	884	0.40	5.4	43.1	63.6	60.4	815	3.2	0.11	56,631	12,702	10,701	9,863
2.0	883	0.28	6.7	43.6	65.1	61.9	815	3.2	0.06	57,715	11,978	10,212	9,418
1.5	883	0.18	9.2	45.1	68.0	65.1	822	2.9	0.03	62,989	10,987	9,592	8,928
1.0	882	0.09	14.1	47.3	72.7	69.9	834	2.8	0.01	65,132	9,696	8,625	8,157
4x Crush V1.0													
2.8	886	6.46	4.9	43.3	62.4	59.2	815	3.2	2.05	57,841	13,792	11,506	10,587
2.5	891	5.62	5.4	43.6	63.2	60.0	814	3.2	1.61	58,251	13,430	11,266	10,290
2.0	888	4.07	6.7	44.2	65.0	61.8	813	3.2	0.93	58,224	12,474	10,584	9,690
1.5	893	2.67	9.0	45.2	67.7	64.5	817	3.2	0.46	57,893	11,483	9,854	9,016
0.9	869	1.35	14.4	47.6	72.8	69.7	832	3.1	0.15	57,390	9,734	8,528	8,163
0.5	877	0.50	27.2	53.0	84.0	80.8	863	3.2	0.03	57,401	7,838	7,037	6,921
4x Crush V2.0													
2.8	883	6.55	4.8	43.2	62.9	59.6	811	3.3	2.08	55,215	13,317	11,088	10,176
2.5	882	5.63	5.4	43.4	63.8	60.6	811	3.2	1.60	57,211	12,705	10,721	9,854
2.0	882	3.96	6.7	44.0	65.7	62.6	816	3.1	0.91	58,667	11,741	10,063	9,316
1.5	883	2.41	9.2	45.2	69.1	66.1	826	3.0	0.41	60,676	10,492	9,171	8,570
1.0	881	1.30	13.8	47.2	74.2	71.4	844	2.7	0.15	67,025	9,011	8,103	7,765

REFERENCES

[1] Julian Goldsmid, *Introduciton to Thermoelectricity*.: Springer, 2010.

[2] Thermoelectric Engineering. [Online]. http://www.thermoelectrics.caltech.edu/thermoelectrics/history.html

[3] TE Technology. (2010) FAQ & Technical Information.

[4] ERG Aerospace. (2011) [Online]. http://www.ergaerospace.com/Aluminum-properties.htm

[5] E. P. Little, *Cooling of Avionic Equipment by Thermoelectrric Methods*.: Transactions on Aerspace, 1964, vol. 2.

[6] Laird Technologies, "Thermoelectric Modules & Assemblies for Medical Laser Applications," 2011.

[7] Edward Kolesar, "Thermoelectric Cooling: Review and Application," Brooks Air Force Base, Texas, 1981.

[8] M. Davis, R. Weymouth, and P. Clarke, "Thermoelectric CPU Cooling using High Efficieny Liquid Flow Heat Exchanger," Fremantle, West Australia, 2004.

[9] Hong Xie, Andre Ali, and Rakesh Bhatia, "The use of heat pipes in personal computers," pp. 442-448, 1998.

[10] HoSung Lee, *Thermal Design*. Hoboken, New Jersey: John Wiley & Sons, 2010.

[11] J. Toth, R. DeHoff, and K. Grubb, "Heat Pipes: The Silent Way to Manage Desktop Thermal Problems," pp. 449-455, 1998.

[12] M. Ikeda et al., "Thermal performance of thermoelectric cooler (tec) integrated heat sink and optimizing structure for low acoustic noise / power consumption," pp. 144-151, 2006.

[13] M. Davis, B. Manners, and P. Clarke, "Design of a 126 Litre Refrigerator/Freezer Commerical Prototype," Fremantle, West Australia, 2004.

[14] J.G. Vian and D. Astrain, "Development of a heat exchanger for the cold side of a thermoelectric module," no. 28, pp. 1514-1521.

[15] Jihui Yang and Francis R Stabler, "Automotive Applications of Thermoelectric Materials," *Journal of Electronic Materials*, pp. 1245-1251, 2009.

[16] Amerigon. (2012) Climate Control Seat. [Online]. http://amerigon.com/ ccs seating .php

[17] L.E. Bell, "Broader use of Thermoelectric Systems in Vehicles," , Berlin, Germany, October 2008.

[18] Harry Asada and M Menon, "Iterative learning control of shape memor alloy actuators with thermoelectric temperature regulation for a multifunctional car seat," in *American Control Conference*, Minneapolis, Minnesota, 2006, pp. 935-939.

[19] C.S. Junior, N.C. Strupp, N.C. Lemke, and J. Koehler, "Modeling a Thermoelectric HVAC System for Automobiles," vol. 28, no. 7, pp. 1093-1097, 2009.

[20] (2010, October) Transitioning to LOW-GWP alternatives in MVACs. [Online]. http://www.epa.gov/spdpublc/downloads/EPA_HFC_MVAC.pdf

[21] John Lofy and Lon E Bell, "Thermoelectrics for Environmental Contol in Automobiles," in *International Conference on Thermoelectronics*, 2002, pp. 471-476.

[22] Soonseo Park, Jungho Yoo, and Shiho Kim, "A thermoelectric generation waste heat recovery system using engine coolant for light-duty ICE vehicles," in *International Conference on Electrical Machines and Systems*, 2010, pp. 2012 - 2015.

[23] Terry J Hendricks and Jason A Lusbader, "Advanced thermoelectric power system investigations for Light-Duty and heavy duty Applications: Part I," in *International Conference on Thermoelectronics*, 2002, pp. 381-386.

[24] Jihad Haider and Jamil Ghojel, "Waste heat recovery from the echaust of low-power diesel engine using thermoelectric generators," in *International Conference on Thermoelectrics*, 2001, pp. 413-417.

[25] Burhan Ozmat, Bryan Leyda, and Burt Benson, "Thermal Applications of Open Cell Metal Foams," ERG, Material and Aerospace Corporation, Oakland, CA, 2008.

[26] Burhan Ozmat, "Reticulated Metal Foams Build Better Heatsinks," *Power Electronics Technology*, pp. 30-35, November 2007.

[27] John Banhar, "Manufacture, Characterisation and application of cellular metals and metal foams," *Progress in Materials Science*, pp. 559-632, 2001.

[28] ERG Aerospace. (2013, April) The Basics of Duocel Foam. [Online]. http://www.ergaerospace.com/Descriptors.htm

[29] Wikipedia. (2013, March) Reticulated Foam. [Online]. http://en.wikipedia.org/wiki/Reticulated_foam

[30] J.G Fourie and J.P Du Plessis, "Pressure Drop Modeling in Cellular Metallic Foam," *Chemical Engineering Science*, pp. 2781-2789, 2002.

[31] C.Y Zhao, W Lu, and S.A Tassou, "Thermal Analysis on Metal-foam filled heat exchangers. Part II: Tube heat exchangers," *International Journal of Heat and Mass Transfer 49*, pp. 2762-2770, 2006.

[32] Wassim Azzi, "A systematic study on the mechanical and thermal properties of open cell metal foams for aerospace applications," North Carolina State University, Raleigh, Masters Thesis 2004.

[33] Ahmad Pesaran, "Battery Thermal Management in EVs and HEVs: issues and solutions," , Las Vegas, Neveda, 2001.

[34] Ferrotec. Thermoelectric Technical Reference — Reliability of Thermoelectic Coolers. [Online]. http://www.ferrotec.com/technology/thermoelectric/thermalRef10/

[35] R. Ahiska, s. Dislitas, and G. Omer, "A new method and computer-controlled system for measuring the time constant of real thermoelectric modules," no. 53, pp. 314-321, 2012.

[36] Gao Min and D.M. Rowe, "Improved model for calculating the coefficient of performance of a Peltier module," no. 41, pp. 163-171, 2000.

[37] H. Demirel, B. Ciylan, B. Erkal, and S. Yilmaz, "Design of a universal thermoelectric module test system for testing rat brain thermoelectric hypothermia," no. 3, pp. 160-165, 2007.

[38] R. Ahiska and K. Ahiska, "New Method for investigation of parameters of real thermoelectric modules," no. 51, pp. 338-345, 2010.

[39] X.C. Xuan, "Investigation of thermal contact effect on thermoelectric coolers," no. 44, pp. 399-410, 2003.

[40] L.E. Bell, "Paradigm Shift in SOlid-State Cooling, Heating and Temperature Control," , Irving, Texas, October 2002.

[41] Lon. E. Bell, "Cooling, Heating, Generating Power and Recovering Waste Heat with Thermoelectric Systems," vol. 321, pp. 1457-1461, September 2008.

[42] Lon. E. Bell, "Alternate Thermoelectric Thermodynamic Cycles with Improved Power Generation Efficiencies," , Hérault, France, August 2003.

[43] TE Technology. (2012, February) HP-127-1.4-1.5-74. [Online]. http://www.tetech.com/temodules/graphs/HP-127-1.4-1.5-74.pdf

[44] Manickam Srinivasen and Manickam Praslad, "Advanced Thermoelectric Energy Recovery System in Light Duty and Heavy Duty Vehicles: Analysis on Technical and Marketing Challenges," in *International Conference on Power Electronics and Drives Systems*, 2005, pp. 977-982.

[45] T.A. Corser, "Qualification and reliability of thermoelectric coolers for use in laser modules," , Breinigsville, PA, 1991, pp. 150-156.

[46] Paul G. Lau and Michael J. Nagy. (2004, November) Process Cooling. [Online]. http://www.process-cooling.com/Articles/Feature_Article/b9545767cb5b7010VgnVCM100000f932a8c0

[47] A Bhattacharya, V.V Calmidi, and R. L Mahajan, "Thermophysical properties of high porosity metal foams," *International Journal of Heat and Mass Transfer*, vol. 45, pp. 1017-1031, 2002.

[48] K Boomsma and D Poulikakos, "The effects of compression and pore size variations on the liquid flow characteristics of metal foam," *Journal of Fluids Engineering- Transactions of the ASME*, vol. 124, pp. 263-272, 2002.

[49] Yunus Cengel and Robert Turner, *Fundamentals of THERMAL-FLUID SCIENCES*, 2nd, Ed. New York, NY: McGraw Hill, 2005.

[50] K Boomsma, D Poulikakos, and F Zwick, "Metal foams as compact high performance heat exchangers," *Mechanics of Materials*, vol. 35, pp. 1161-1176, 2003.

[51] B E Antohe, J L Lage, D C Price, and R M Weber, "Experimental determination of Permeability and Intertia Coefficients of Mechanically Compressed Aluminum Porous MAtrices," *Transactions of the ASME*, vol. 119, pp. 404-412, June 1997.

[52] C Y Zhao, T Kim, T J Lu, and H P Hodson, "Thermal Transport Phenomena in Porvair Metal Foams and Sintered Beds," Micromechanics Centre & Whittle Lab Department of Engineering University of Cambridge, 2001.

[53] William D. Callister, Jr., *Materials Science and Engineering an Introduction*, 7th ed.: John Wiley & Sons, Inc. , 2007.

[54] ERG Aerospace Corp. (2011) [Online]. http://www.ergaerospace.com/Copper-properties.htm

[55] University of Waterloo. (1997) Fluid Properties Calculator. [Online]. http://www.mhtl.uwaterloo.ca/old/onlinetools/airprop/airprop.html

[56] Robert J. Moffat, "Describing the Uncertainties in Experimental Results," *Experimental Thermal and Fluid Science*, pp. 3-17, 1988.

[57] Mikros Manufacturing. (2012) [Online]. http://www.mikrosmanufacturing.com/

[58] Chemical and Process Engineering Resources. (2012, May) U in Heat Exchangers. [Online]. http://www.cheresources.com/content/articles/heat-transfer/u-in-heat-exchangers

[59] R.L. Webb, M.D. Gilley, and V. Zarnescu, "Advanced Heat Exchange Technology for Thermoelectric Cooling Devices," vol. 120, no. 1, pp. 98-105, 1998.

[60] Donald T Morelli, "Potential Applications of advanced thermoelectrics in the automobile industry," in *15th International Conference on Thermoelectrics*, 1996, pp. 383-386.

[61] Zheng Zhang, Xiaopeng Xie, and Yutao Luo, "Research on the novel High-intensity Thermoelectric Generator and Its Application on HEV," in *International Conference on Thermoelectrics*, 2005, pp. 505-508.

[62] Ahmad Persaran, Andreas Vlahinos, and Thomas Stuart, "Cooling and Preheating of Batteries in Hybrid Electric Vehicles," , 2003.

[63] Rutvik J. Mehta et al., "A new class of doped nanobulk high-figure-of-merit thermoelectrics by scalable bottom-up assembly," vol. 11, pp. 233-240, March 2012.